Conception et réalisation de cristaux photoniques et de réseaux de diffraction pour les cellules photovoltaïques silicium en couches ultra-minces

Xianqin Meng

N° d'ordre 2012-30 Année 2012

Thèse

Conception et réalisation de cristaux photoniques et de réseaux de diffraction pour les cellules photovoltaïques silicium en couches ultra-minces

Présentée devant
L'Ecole Centrale de Lyon (ECL)

Pour obtenir
Le grade de docteur

École doctorale Materiaux de Lyon
Spécialité : Nanophotonique

Par
Xianqin MENG

Soutenue le 15 Octobre 2012 à l'ECL

Jury

Rapporteur	Mr. Ludovic Escoubas	Professeur
Rapporteur	Mr. Yves Jourlin	Maître de Conférences HDR
Examinateur	Mme. Anne Kaminski	Professeur
Examinateur	Mr. Ounsi El Daïf	Chercheur, IMEC
Directeur de thèse	Mr. Christian Seassal	Directeur de recherche CNRS
Co-directeur de thèse	Mr. Alain Fave	Maître de Conférences
Invité	Mr. Emmanuel Drouard	Maître de Conférences

Laboratoire de recherche : Institut des Nanotechnologies de Lyon (INL

N° d'ordre 2012-30 Année 2012

Thèse

Design and fabrication of photonic crystals and diffraction gratings for ultra thin film Si solar cells

Présentée devant
L'Ecole Centrale de Lyon (ECL)

Pour obtenir
Le grade de docteur

École doctorale Materiaux de Lyon
Specialty : Nanophotonic

Par
Xianqin MENG

Soutenue le 15 Octobre 2012 à l'ECL

Jury

Rapporteur	Mr. Ludovic Escoubas	Professeur
Rapporteur	Mr. Yves Jourlin	Maître de Conférences HDR
Examinateur	Mme. Anne Kaminski	Professeur
Examinateur	Mr. Ounsi El Daïf	Chercheur, IMEC
Directeur de thèse	Mr. Christian Seassal	Directeur de recherche CNRS
Co-directeur de thèse	Mr. Alain Fave	Maître de Conférences
Invité	Mr. Emmanuel Drouard	Maître de Conférences

Laboratoire de recherche : Institut des Nanotechnologies de Lyon (INL)

ÉCOLE CENTRALE LYON — Direction de la recherche

Liste des personnes Habilitées à Diriger des Recherches en poste à l'Ecole Centrale de Lyon

Nom Prénom	Corps grade	Laboratoire ou à défaut département ECL	Etablissement
HEROUX Abderrahmane	*professeur*	AMPERE	ECL
SURET François	*professeur*	AMPERE	ECL
JAFFREZIC-RENAULT Nicole	*directeur de recherche*	AMPERE	CNRS/ECL
KHÄHE-NEUHI Leonard	*directeur de recherche*	AMPERE	CNRS/ECL
NICOLAS Alain	*professeur*	AMPERE	ECL
NICOLAS Laurent	*directeur de recherche*	AMPERE	CNRS/ECL
SOURTIER Gérard	*professeur*	AMPERE	ECL
SIMONET Pascal	*directeur de recherche*	AMPERE	CNRS/ECL
VOLLAIRE Christian	*professeur*	AMPERE	ECL
		Nbre Ampère 9	
DE LOURN Yves	*maître de conférences*	DER EEA	ECL
		Nbre DER EEA 1	
GUINAUDEAU Hervé	*professeur Service*	DER STMS	ECL
VINCENT Léo	*professeur*	DER STMS	ECL
		Nbre DER STMS 2	
LOHEAC Jean-Pierre	*maître de conférences*	ICJ	ECL
MAITRE Jean-François	*professeur émérite*	ICJ	ECL
MARION Martine	*professeur*	ICJ	ECL
MIRONESCU Elisabeth	*professeur*	ICJ	ECL
MOUSSAOUI Mohand	*professeur*	ICJ	ECL
MUSY François	*maître de conférences*	ICJ	ECL
ZINE Abdel-Malek	*maître de conférences*	ICJ	ECL
		Nbre ICJ 7	
DAVID Bertrand	*professeur*	ICTT	ECL
		Nbre ICTT 1	
CALLARD Anne Ségolène	*professeur*	INL	ECL
DI DARIO Jean-Pierre	*maître de conférences*	INL	ECL
GAFFIOT Frédéric	*professeur*	INL	ECL
GAGNAIRE Alain	*maître de conférences*	INL	ECL
GARRIGUES Maïté	*directeur de recherche*	INL	CNRS/ECL
GENDRY Michel	*directeur de recherche*	INL	CNRS/ECL
GRENET Geneviève	*directeur de recherche*	INL	CNRS/ECL
HOLLINGER Guy	*directeur de recherche*	INL	CNRS/ECL
KRAWCZYK Stanislas	*directeur de recherche*	INL	CNRS/ECL
LETARTRE Xavier	*chargé de recherche*	INL	CNRS/ECL
O CONNOR Ian	*professeur*	INL	ECL
PHANER-GOUTORBE Magali	*professeur*	INL	ECL

ROBACH Yves	professeur	INL	ECL
SAINT-ONGES Guillaume	chargé de recherche	INL	CNRS/ECL
SEASSAL Christian	directeur de recherche	INL	CNRS/ECL
SOUTEYRAND Claire	directeur de recherche	INL	CNRS/ECL
TARDY Jacques	directeur de recherche	INL	CNRS/ECL
VIKTOROVITCH Pierre	directeur de recherche	INL	CNRS/ECL

Nbre INL 18

CHEN Liming	professeur	LIRIS	ECL

Nbre LIRIS 1

BAILLY Christophe	professeur	LMFA	ECL
BERTOGLIO Jean-Pierre	directeur de recherche	LMFA	CNRS/ECL
BLANC-BENON Philippe	directeur de recherche	LMFA	CNRS/ECL
BOGEY Christophe	chargé de recherche	LMFA	CNRS/ECL
CAMBON Claude	directeur de recherche	LMFA	CNRS/ECL
CARRIERE Philippe	directeur de recherche	LMFA	CNRS/ECL
CHAMPOUSSIN J Claude	professeur émérite	LMFA	ECL
COMTE-BELLOT geneviève	professeur émérite	LMFA	ECL
FERRAND Pascal	directeur de recherche	LMFA	CNRS/ECL
GALLAND Marie Annick	professeur	LMFA	ECL
GODEFERD Fabien	directeur de recherche	LMFA	CNRS/ECL
GOROKHOVSKI Mikhael	professeur	LMFA	ECL
HENRY Daniel	directeur de recherche	LMFA	CNRS/ECL
JEANDEL Denis	professeur	LMFA	ECL
JUVE Daniel	professeur	LMFA	ECL
LE RIBAULT Catherine	chargée de recherche	LMFA	CNRS/ECL
LEBOEUF Francis	professeur	LMFA	ECL
PERKINS Richard	professeur	LMFA	ECL
ROGER Michel	professeur	LMFA	ECL
SCOTT Julian	professeur	LMFA	ECL
SIMO Liang	directeur de recherche	LMFA	CNRS/ECL
SUBRENAT Serge	chargé de recherche	LMFA	CNRS/ECL
TRESMAC Isabelle	maître de conférences	LMFA	ECL

Nbre LMFA 23

BENAYOUN Stéphane	professeur	LTDS	ECL
CAMBON Bernard	professeur	LTDS	ECL
CROUZET Bernard	maître de conférences	LTDS	ECL
DANESCU Alexandre	maître de conférences	LTDS	ECL
FOUVRY Siegfried	chargé de recherche	LTDS	CNRS/ECL
GEORGES Jean-Marie	professeur émérite	LTDS	ECL
GUERRET Chrystelle	chargée de recherche	LTDS	CNRS/ECL
HERTZ Dominique	mcf	LTDS	ECL
ICHCHOU Mohamed	professeur	LTDS	ECL
JEZEQUEL Louis	professeur	LTDS	ECL
JUVE Denyse	ingénieur de recherche	LTDS	ECL
KAPSA Philippe	directeur de recherche	LTDS	CNRS/ECL
LE JOT Alain	directeur de recherche	LTDS	CNRS/ECL
LOUBET Jean-Luc	directeur de recherche	LTDS	CNRS/ECL
MARTIN Jean-Michel	professeur	LTDS	ECL
MATHIA Thomas	directeur de recherche	LTDS	CNRS/ECL
MAZUYER Denis	professeur	LTDS	ECL
PERRET-LIAUDET Joël	maître de conférences	LTDS	ECL
SALVIA Michelle	maître de conférences	LTDS	ECL

SIKOROFF François	professeur	LTDS	ECL
SINOU Jean Jacques	professeur	LTDS	ECL
STREMSDOERFER Guy	professeur	LTDS	ECL
THOUVEREZ Fabrice	professeur	LTDS	ECL
TROMEUX Daniel	professeur	LTDS	ECL
VINCENS Eric	maître de conférences	LTDS	ECL

Acknowledgements

I would like to express my deep and sincere gratitude to my PhD advisor professor Christian Seassal, and co-advisors Emmanuel Drouard and Alain Fave, for supporting me during the past three years. Christian has been supportive and has given me the freedom to pursue various projects without objection. His wide knowledge, logical ways of thinking, understanding, encouraging and personal guidance have provided a good basis for the resent thesis. I hope that I could be as enthusiastic and energetic as Christian in my future research career. I am also very grateful to Emmanuel for his scientific advice and knowledge and many insightful discussions and suggestions. He is my primary resource for getting my science questions and is instrumental in modifying papers and thesis. I also want to thank my co-author and friend Alain for his advices on my studying and modifying my thesis as well as his personal helps on my life in France. I could not have asked for better role models as Christian, Emmanuel and Alain, each inspirational, supportive, and patient. I could not be prouder of my academic roots and hope that I can in turn pass on the research values and the dreams that they have given to me. I also want thank the members of my PhD committee, Professors Ludovic Escoubas, Yves Jourlin, Anne Kaminski and Mr. Ounsi El Daïf for their helpful career advice and suggestions in general.

I will forever be thankful to my former college research advisor: Professor Qingyu Zhang has been helpful in providing advice many times during my graduate school career. He is and remains my role model for a scientist, mentor, and teacher. I still think fondly of my time as an undergraduate student in his lab. Prof. Zhang was the reason why I decided to go to pursue a career in research. His enthusiasm and love for teaching and investigating are contagious.

I also thank my partner Guillaume Gomard for his help on experimental assistance and results discussions during the last three years. He is one of the most brilliant and hard work Ph.D candidates as far as I know. Without his help, I

think I could not finish my Ph.D works so well. I will never forget the investigation suggestions and personal helps from Ounsi EI Daif and Romain Peretti during their postdoctoral research in PV group. In addition, I would like to give my gratitude to Regis Orobtchouk for his training and experience transmission on laser holographic lithography, and Valerie Depauw in IMEC, Belgium for technology and measurement results discussion in the last year of my Ph.D.

I own my most sincere gratitude to all the present members of cleanroom in INL: Mazurczyk Radoslaw (extremely knowledgeable, teaching, helpful, and friendly), Pierre Cremillieu (has been helpful with cleaning and repairing experimental tools and other questions in general), Jean-Louis Leclercq (a nice and humorous person who has been pretty supportive during last three years), Cécile James (a strict and intense expert on SEM who has also helped me many times), and Brice Devif (a nice and friendly engineer who helps us to deposit glass several times). As well as the stuffs and students at Photovoltaic Group and Photonic Group in Ecole Centrale de Lyon and INSA de Lyon, I am grateful for the chance to work and discuss with you time to time. Thanks for your helping and supporting to develop my thesis. I own lots of gratitude to colleges and stuffs in LPICM Paris and IMEC Belgium for sample preparing and characterizations.

My sincere thanks are due to all the secretaries and other stuff: Nicole Durand (has been so helpful and gentle to help me dealing with lots of official papers), Patricia Dufaut (is a beautiful and nice lady to deal with all the conferences documents), Sylvie Goncalves (for her kindly and nicely helps on official papers), Laurent Carrel (for his helps on computation tools).

My warm thanks are due to my colleagues from Office F7220, Clement Sieutat, Koku Kusiaku, Taiping Zhang, Huanhuan Liu, and other past master students, Shengli Zhang, Florian Longnos, Felix Yu and so on. Thanks for you companying in these years. Best wishes for your careers and future. At the same

time, I want to thank all of my friends; you always make me feel that I am not alone in France.

Zhaoxian MENG and Hongxia ZHANG, my dear parents, I don't know how to appreciate is enough to let them know my love and feeling. They invested so much passion and time on me. At every step of my life, they are always with me though they are physically thousands and millions of miles away. It is an honor to be their daughter. Without their encouragement, understanding and taking care during these years, it would impossible for me to insist on and finish my thesis.

Finally, I would like to acknowledge Chinese Scholarship Council (CSC) support my study in France, and also thanks for the region Rhône-Alpes project, the ANR SPARCS project and INL-IMEC collaboration to fund and help my research in INL, France.

CONTENTS

Chapter 1

Introduction

1.1 Situation and development of solar cells

Photovoltaics, the direct conversion of sunlight to electricity using solar cells, is recognised as one of the most promising energy options for a sustainable future. The present photovoltaic market is dominated by silicon, which is the oldest and most widely used semiconductor material. Crystalline silicon (c-Si) represents about 95% of the whole photovoltaic market [1]. The most established technology in photovoltaic industry is based on this material. c-Si solar cells have been commercially available for years and satisfactory performances have been achieved. Thus, conversion efficiencies around 25% in laboratory cells and 23% in commercial module [2] have been reported. However, silicon raw material is becoming more and more expensive and is preventing further cost reduction for such "first generation" solar cells although production is growing rapidly, which leads to a decrease of modules cost. The "second generation" solar cells are produced by using very thin semiconductors layers, therefore using much less active material [3]. Thin film cells use one of three major semiconductor materials: silicon (for example, a-Si) [4-5], cadmium telluride (CdTe) [6], or copper-indium-gallium selenide (CIGS) [7].

Among these different technologies, Silicon-based materials are attractive because of their abundance and non-toxicity. In particular, solar cells using hydrogenated amorphous silicon (a-Si:H) are attractive because this material exhibits a very high absorption coefficient [8]. However, despite of the encouraging results obtained with a-Si:H [4-5], some drawbacks, lower absorption in long wavelength and higher bulk recombination, have led to study of variety of alternatives for silicon thin film photovoltaic applications. In particular, mono crystalline silicon (c-Si) [9], polycrystalline silicon (poly-Si:H) [10-11], microcrystalline silicon (μc-Si:H) [12] or nanocrystalline silicon (nc-Si:H) [13],

have been proposed and have received much attention. Among these different possibilities, the use of c-Si layers enables a strong reduction of the bulk recombination as compared to polycrystalline and amorphous silicon layers. Using this material is thus very promising way to build cost-effective photovoltaic devices. However, the energy conversion efficiency of such second generation solar cells is much lower than for the first generation devices. This is due to a reduced photon path length (or lifetime), which limits the absorption efficiency, and an increased carrier recombination processes. In particular, in the case of ultra-thin film solar cells, the absorption in the red and infrared is not sufficient to maintain good conversion efficiency. It is therefore of prime importance to control light collection and absorption, in particular the long wavelength range [14-15]. This is the goal of light trapping. Such a concept if essential to reach sufficient conversion efficiencies provided the cost of the solar cells is not substantially increased.

Considering the maturity of nanophotonics, various kinds of advanced light trapping techniques may be considered [16-18]. These include photonic crystals, diffraction gratings and anti-reflective coatings, as well as metallic nanostructures.

1.2 Thesis overview

In this thesis, we will investigate the impact of periodic photonic nanostructures like photonic crystals or diffraction gratings on thin film solar cells based on a-Si:H and c-Si. After a brief introduction on the thin film silicon solar cells, and a short review of the recent light trapping strategies, in Chapter 2, we will introduce the methodologies developed to design and fabricate the targeted photonic nanostructures (Chapter 3). In Chapter 4, we will present the integration of an absorbing hydrogenated amorphous silicon (a-Si:H) PCs within a thin film photovoltaic solar cell. Optical simulations performed on a complete solar cell reveal that patterning the a-Si:H active layer as a 2D photonic crystal membrane

enables to increase its integrated absorption from 300 nm to 720 nm, in comparison to a similar but unpatterned stack. In order to fabricate such promising cells, we developed a high throughput process based on laser holographic lithography (LHL) and reactive ion etching (RIE). The influences of the parameters taking part in those processes on the obtained patterns are discussed. Optical measurements performed on the "photonized" solar cell structures are discussed and compared to the simulated absorption spectra. Moreover, the angular dependence effect will be measured. Then, in Chapter 5, we will present the integration of an absorbing photonic crystal within c-Si thin film photovoltaic stacks. Finite difference time domain (FDTD) optical simulations are performed in order to design 1D or 2D PCs to assist crystalline silicon solar cells. Optimal designs result from the scanning of lattice parameters of each possible candidate stacks, and the absorption efficiency is calculated in the whole wavelength range between 300 nm and 1100 nm. We will also present the fabrication of such patterned stacks, by a specific set of processes based on LHL, RIE and inductively coupled plasma (ICP) etching. Optical measurements and simulations will be compared in the whole wavelength range of interest. Moreover, we will show that within this design, the influence of the angle of incidence will be measured and discussed. Lastly, we will present the integration of combined front and back 1D or 2D diffraction gratings with different periods, within thin film photovoltaic solar cells based on crystalline silicon layers. The grating structures have been designed considering both the need for incident light absorption enhancement and the technological feasibility. A complete solar cell with combined front and back 1D or 2D diffraction gratings is then designed. The simulated absorption spectra in the crystalline silicon layer and the short circuit current will be discussed, and a preliminary technological feasibility test will be presented.

References and links

[1] *SunShot Vision Study* – US DOE, February 2012.

[2] M.A. Green,et al,"Crystalline silicon on glass (CSG) thin film solar cell modules," Sol. Energy **77**, 857-863 (2004).

[3] A.G. Aberle, "Thin-film solar cells," Thin Solid Films **517**, 4706–4710 (2009).

[4] K. Yamamoto, A. Nakajima, M. Yoshimi, T. Sawada, S. Fukuda, T. Suezaki, M. Ichikawa, Y. Koi, M. Goto, and T. Meguro, "A high efficiency thin film silicon solar cell and module," Sol. Energy **77**, 939–949 (2004).

[5] J. Yang, A. Banerjee, T. Glatfelter, S. Sugiyama, and S. Guha, "Recent progress in amorphous silicon alloy leading to 13% stable cell efficiency," In Photovoltaic Specialists Conference, 1997, Conference Record of the Twenty-Sixth IEEE, 563–568 (1997).

[6] G. Fulop,M. Doty, P Meyers, J. Betz and CH Liu, "High-efficiency electrodeposited cadmium telluride solar cells", Appl. Phys. Lett. **40**, 327-328(1982).

[7] R. A. Mickelsen and W.S. Chen, "High photocurrent polycrystalline thin film Cd/CuInSe2 solar cell," Appl. Phys. Lett. **36** (1980) 371-373.

[8] R. E. I. Schropp and M. Zeman, *Amorphous and microcrystalline silicon solar cells: modeling, materials, and device technology*, (Kluwer Academic Publishers, Norwell, Mass., 1998).

[9] V. Depauw, Y. Qiu, K. Van Nieuwenhuysen, I. Gordon, and J. Poortmans, "Epitaxy-free monocrystalline silicon thin film: first steps beyond proof-of-concept solar cells," Progress in Photovoltaics: Research and Applications **19**, 844-850 (2010).

[10] R. Iiduka, A.Heya, and H. Matumura, R. Iiduka et al., "Study on CAT CVD poly Si film for solar cell application," Sol. En. Mat. Sol. Cells **48**, 279–285 (1997).

[11] R. E. I. Schropp and M. Zeman, *Amorphous and Microcrystalline Silicon Solar Cells: Modeling, Materials and Device Technology* (Kluwer, Dordecht, 1998).

[12] Shah AV, Meier J, Vallat-Sauvain E, Wyrsch N, Kroll U, Droz C, Graf U, "Material and solar cell research in microcrystalline silicon," Sol. En. Mat. Sol. Cells **78**, 469–491 (2003).

[13] Sukti Hazra and Swati Ray, "Nanocrystalline silicon as intrinsic layer in thin film solar cells," Solid State Communications **109**,125 – 128 (1998).

[14] R. H. Franken, R. L. Stolk, H. Li, C. H. M. van der Werf, J. K. Rath, and R. E. I. Schropp, "Understanding light trapping by light scattering textured back electrodes in thin film n-i-p-type silicon solar cells," J. Appl. Phys. **102**, 014503 (2007).

[15] J. Müller, B. Rech, J. Springer, and M. Vanecek, "TCO and light trapping in silicon thin film solar cells," Sol. Energy **77**, 917-930 (2004).

[16] M.Peters, J. C.Goldschmidt, T. Kirchartz, and B.Bläsi, "The photonic light trap--Improved light trapping in solar cells by angularly selective filters," Sol. En. Mat. Sol. Cells **93**, 1721-1727 (2009).

[17] A. Goetzberger and J.C. Goldschmidt and M. Peters and P. Löper, "Light trapping, a new approach to spectrum splitting," Sol. En. Mat. Sol. Cells **92**, 1570–1578 (2008).

[18] O. E. Daif, E. Drouard, G. Gomard, A. Kaminski, A. Fave, M. Lemiti, S. Ahn, S. Kim, P. Roca i Cabarrocas, H. Jeon. and C. Seassal, "Absorbing one-dimensional planar photonic crystal for amorphous silicon solar cell," Opt. Express **18**, A293-A299 (2010).

Chapter 2

Thin film silicon solar cells: state of the art, basics and materials

2.1 Introduction

At present, most of the Photovoltaics (PV) solar cells market is based on 200 μm thick crystalline silicon wafer [1]. A significant part of the cost of a solar cell is due to the Si material and its processing. Based on this, ultra thin film solar cells (with thicknesses in the range 100 nm to 2 μm) have been increasingly attractive with regards to materials consumption. Increasing their absorption through light trapping techniques is then essential to achieve reasonable conversion efficiency [2-3].

In this chapter we will present solar cell operation and define the main cell parameters. Different possible thin film architectures and materials for absorbing layers, antireflective coating, metallic mirrors, etc, will be introduced. Finally, we will briefly describe concepts and a selected state of the art of light trapping techniques in such cells.

2.2 Solar cell operation

In a photovoltaic device, incident photons are absorbed, generate electron-hole pairs, which are then separated and collected to create an electrical current. The physics in the active photovoltaic region is that of a p-n junction, which forms the fundamental operation principles of a vast array of electronic and optoelectronic devices.

As introduced above, in order to increase the efficiency of a solar cell, one of the most important challenge stands in light trapping, and more generally, optical engineering. It is indeed essential to reduce the reflection at the front surface, to selectively increase the absorption in the active layer, by increasing the optical path length of light in a wide wavelength range.

The intensity of light transmitted into the solar device gets attenuated when it passes through the photovoltaic material. This attenuation (rate of absorption) is proportional to the intensity of the light at a given wavelength. The decay in intensity, of monochromatic light passing through the solar cell, is exponential in nature and can be described by the Beer-Lambert law:

$$I(x) = I'e^{-\alpha x} \tag{2.1}$$

where I is the intensity of transmitted light, x is the depth into the material and α is the absorption coefficient, $I' = I_{inc}\ (1-R)$, in which I_{inc} and R are intensity of incident light and reflectance. This wavelength dependent parameter is the inverse of the absorption depth; it determines how far into a material a light wave can penetrate before being absorbed.

By using this equation, we can calculate the number of electron-hole pairs which are being generated in the active layer of the device. So, the generation rate (G) in a solar cell could be obtained by calculating the change in light intensity:

$$G(x) = \alpha N_0 e^{-\alpha x} \tag{2.2}$$

where N_0 is the photon flux at the absorbed solar cell surface in units of photons/unit-area/sec, and x is the distance into the solar cell.

When a photon with sufficient energy is absorbed, an electron-hole pair is generated. When metal electrodes are connected to the emitter and base regions of the solar cell, the generated carriers flow in the external circuit [4]. The generated current is a minority carrier current which flows opposite to the direction of the diode current and thus creates reverse bias operation. This can be seen by looking at the diode equations for a solar cell under dark and illuminated conditions. The ideal diode equation for a solar cell in the dark is given by,

$$I = I_0[\exp(\frac{eV}{KT}) - 1] \tag{2.3}$$

when the solar cell is illuminated the diode current becomes,

$$I = I_0[\exp(\frac{e\square V}{KT}) - 1] - I_{light} \tag{2.4}$$

where I is the current flowing through the diode, I_o is the dark saturation current, V is the applied voltage across the diode, k is Boltzmann's constant, T is the absolute temperature and I_{Light} is the light generated current.

Under dark condition, solar cell presents the same current–voltage curve (I-V) characteristics as a very large diode. The illumination and consequent generation of I_{Light} has the effect of shifting the I-V curve down into the fourth quadrant and hence, power is generated.

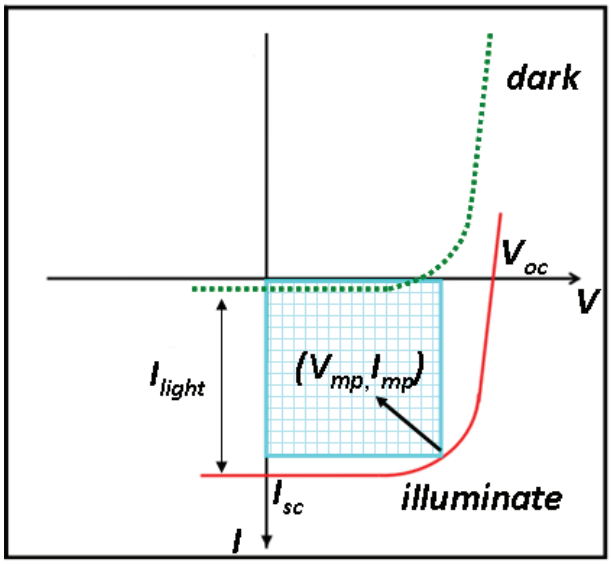

Fig. 2.1. Current and voltage characteristics of a solar cell in the dark and illuminate conditions

The I-V curve can be used to determine a number of important parameters that characterize the performance of a solar cell. The first of these is the short circuit current (I_{sc}), as shown in Fig. 2.1. The short circuit current is the maximum current that can be derived from the solar cell. For ideal solar cells, with no highly resistive losses, the short circuit current is equal to the light generated current ($I_{Light} = I_{sc}$). The short circuit current is dependent on a number of factors which are: the area of the solar cell, the power of the incident light, the spectrum of the

incident light, the absorption characteristics and the collection probability. It is usually expressed as a current density, J_{sc}. The most critical material parameters in comparing the J_{sc} of solar cells of the same material type are the surface recombination velocities and diffusion length. The carrier diffusion length is defined as the distance in the material that a carrier will move from the point at which it is generated to the point at which it recombines. If we assume a perfectly surface passivated solar cell with a uniform generation rate, the J_{sc} can be approximated by,

$$J_{sc} = e*G(L_n + L_p) \tag{2.5}$$

Where G is the generation rate, L_n is the electron diffusion length and L_p is the hole diffusion length.

Another parameter used to characterize solar cell output is the open circuit voltage V_{oc}. The V_{oc} is the maximum voltage that can be obtained from a solar cell, when the current is equal to zero. V_{oc} is determined by the properties of the semiconductor. The equation for V_{oc} is given by,

$$V_{oc} = \frac{KT}{e}\ln[\frac{I_{light}}{I_0} + 1] \tag{2.6}$$

The third parameter used to characterize solar cell performance is called the fill factor (*FF*). The *FF* is defined as the ratio of the maximum power that can be derived from a solar cell to the product of the J_{sc} and V_{oc}. At the points where the J_{sc} and V_{oc} occur, no power is generated because the occurrence of one of these parameters means that the other is zero. The *FF* is therefore the area of the largest rectangle that can fit into the *I-V* curve and is hence, described as a measure of the squareness of the *I-V* characteristics of a solar cell under illumination. It can be calculated using,

$$FF = \frac{J_{mp} \times V_{mp}}{J_{sc} \times V_{sc}} \tag{2.7}$$

The final parameter used in characterizing the performance of a solar cell is the efficiency. The efficiency is defined as the ratio of the electrical output power versus incident optical power. Efficiency can be calculated using,

$$eff = \frac{J_{sc} \times V_{oc} \times FF}{P_{in}} \tag{2.8}$$

The efficiency of a solar cell is affected by intensity and incident light spectrum as well as the temperature of the solar cell. Efficiency measurements are standardized to a temperature of 25 degrees and AM1.5G illumination spectrum. The AM1.5G illumination is the standard irradiance spectrum at the earth's surface; it accounts for losses in solar intensity and power as the light passes through the atmosphere and gets absorbed by air and dust. The *G* in AM1.5G stands for global and it means that the spectrum includes direct and diffuse solar radiation.

2.3 Materials and architectures of thin film solar cells

The typical thin film a-Si:H and c-Si solar cells, which will be at the basis of our investigation, are shown on Fig. 2.2. These structures from the rear to the top are composed of:

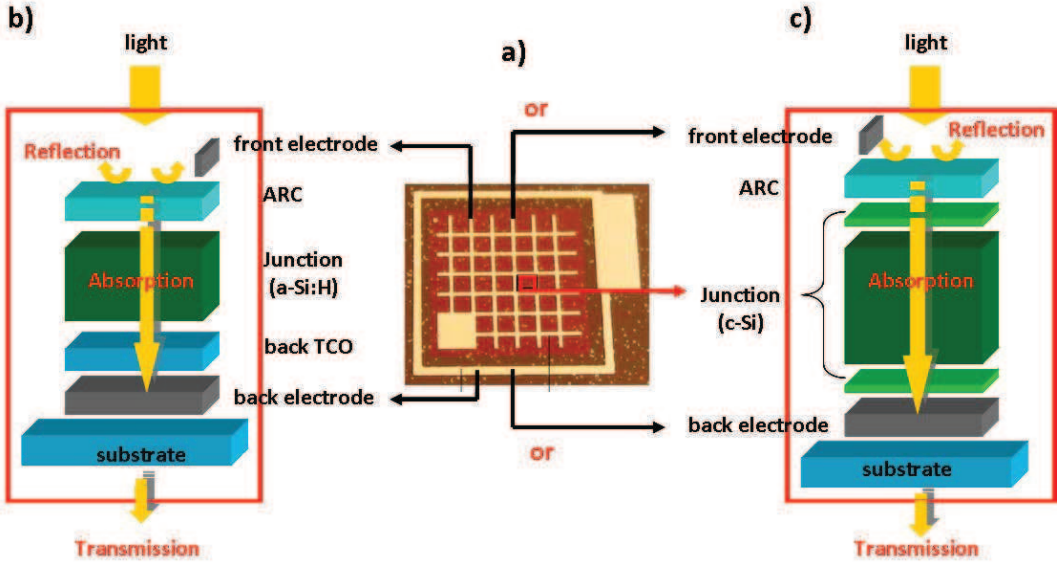

*Fig. 2.2. A typical solar cell device (**a**), a typical a-Si:H thin film solar cell is shown in (**b**) and a classical c-Si solar cell is described in (**c**).*

- A low-cost substrate
- A thin layer of metal contactor, also used on the back side of solar cells to reflect light into device again. This metallic layer should exhibit low sheet resistance and high reflection coefficient.
- The active layer, either hundreds nanometres thick of a-Si:H or few microns of crystalline silicon. An emitter and back surface field will be obtained with n^+ and p^+ highly doped layers.
- An anti-reflection coating (ARC), deposited onto the top surface of solar cells in order to reduce reflection thanks to its low index and controlled thickness. In thin film solar cells, the materials for the ARC could be ultra thin transparent conductive oxide (TCO) layer [5-8].
- Additionally, a back TCO layer is needed in a-Si:H solar cells, as an optical spacer, but also to avoid the diffusion of metallic atoms into Si, shown on Fig. 2.2(**b**).

The optical indices of the materials used in optical optimization are included in the Annex. A. Absorption in all these different layers should be considered, and not only in the silicon absorber.

Materials characteristics, thicknesses, and deposition techniques will be considered and carefully chosen in this thesis. We will also consider real fabrication feasibilities of the devices that will be designed.

In this work we propose to implement solar cells as thin as possible using a-Si or c-Si as absorbing material: reducing the thickness of a-Si down to 100 nm (instead of usually 300-400 nm) and of c-Si down to around 1 μm (instead of 180 μm for wafer based solar cells). When decreasing thickness, absorption can be strongly reduced, especially when considering c-Si. c-Si is strongly absorbing for short wavelength, however, due to its indirect band gap, it is weakly absorbing in the near infrared regime of the solar spectrum. The absorption length (inverse of the absorption coefficient) is 11 μm at 800 nm to over 3 mm at 1100 nm [9]. This effect makes it difficult to achieve high performance thin film devices with thicknesses in the order of a few microns. Therefore, the ideal goal is to get a thinner cell which maintains the effective optical thickness of a thicker cell. Consequently, there is a need for light trapping architectures that increase the optical path length of light within the solar cell and thereby increase the overall cell efficiency.

It is important to note the different behaviour of thin film and wafer based on solar cells. For reduced thicknesses, the surface recombination velocity will become a more important parameter than the diffusion length (for bulk recombination). Actually, by reducing the material volume, it is possible to use a lower quality material. Therefore, light trapping as introduced is extremely essential to confine incident light into such reduced material. However, due to PCs or diffraction grating patterning, there are explosively enhanced dangling bonds. Hence, a large density of defects in patterned materials could generate more recombination centres, which reduces the lifetime of carriers.

2.4 Light trapping for thin film solar cells

When incident light is captured in a solar cell device, a minimized reflectivity is an essential issue to achieve high efficiency solar cells. It is also extremely important that incident light can be efficiently absorbed in the c-Si active layer. In real solar cells, light is partly reflected at the front surface despite of the presence of an ARC (See Fig. 2.2). Still, the main part of the incident light is transmitted into the solar cell device. This transmitted incident light will be partly absorbed by the TCO, silicon and metal layers. A fraction of the solar spectrum, especially in the long wavelength range, will not be absorbed by the layers of the solar cells and will be lost out of the devices.

To increase the efficiency of solar cells, it would be beneficial to retain the light within the absorbing layer for a longer time, because the longer a photon stays, the greater the chances of absorption and creation of an electron hole pair and then increasing the short circuit current characteristics of the solar cell. Light trapping should then afford similar absorption characteristics to thicker cells.

Light trapping is concerned with increasing J_{sc} characteristics of the solar cell device structure. This is achieved through increasing the absorption characteristics which are related to J_{sc}. We will then focus on the improvement of the current versus absorption, defined as [10-11]:

$$J_{sc} = \frac{e}{hc}\int_{\lambda_1}^{\lambda_2} \lambda A(\lambda)\frac{dI}{d\lambda}d\lambda \tag{2.9}$$

in which, c the speed of light in vacuum, λ the wavelength, considering the λ_1- λ_2 range for active silicon, $A(\lambda)$ the absorption in silicon, and I the incident solar radiation spectrum with a units of $W{\cdot}m^{-2}{\cdot}nm^{-1}$. Connecting to Eq (2.8), an increase in J_{sc} directly influences the efficiency of a solar cell device. It is therefore, pertinent to maximize the short circuit current if one wishes to achieve very high

efficiency solar cells. In this respect, either the absorption $A(\lambda)$ or J_{sc} will be considered as the key figure and target when optimizing design parameters of the solar cell architecture.

There has been much work done on light trapping based on principles of geometric optics [12] with the introduction of a maximum absorption increase of $4n(\lambda)^2$, where n is the refractive index of the solar cell material) [13-14] attained by the integration of a Lambertian structure in a thick solar cell, as derived by Yablonovitch and Cody [14]. However, this approach cannot be directly applied to thin layers, where diffraction processes occur. Moreover, the open question is how much more can the absorption efficiency be improved by using wavelength scale structures like photonic crystal or diffraction grating, which could be patterned in thin film solar cells [15-20]. Meanwhile, more conventional texturation techniques have been used for thin film solar cells. Some are based on the control of the surface properties of metallic layer or TCOs like ZnO (by controlling the deposition parameters or by wet etching after the deposition, etc). Others are based on the use of rough glass substrates in combination with conformal deposition. All these methods lead to rough surfaces and interfaces which contribute to light trapping [21-23]. However, there is a very limited possibility to control the surface characteristics, and therefore the optical properties of such devices.

Absorption enhancement by using photonic crystals (PCs) has been proposed as a promising approach for improving the optical performance of solar cells. The objective is to use one, two or three dimensional (1D, 2D or 3D) periodic structures which exhibit a wide variety of light diffraction effects. Indeed, a Photonic Crystal [24-25] is a structure which refractive index is periodically modulated, with a lattice constant on the order of the operation wavelength. If layers of different dielectric constant may be deposited or adhered together to form a band gap in a single direction, it is named 1D PCs. A Bragg grating is an example of this type of PCs. Layers with a planar distribution of the dielectric constant, in one or two dimensions are referred to as 1D or 2D planar PCs. More

complex 3D PC structures have also been investigated theoretically [26-27] and experimentally [28]. It was recently proposed to use PCs as complex back reflectors or efficient anti-reflection coatings [2-3, 29-31], in order to enhance the absorption in an active layer. We also have proposed a concept to produce highly efficient absorbers. It consists in patterning an hydrogenated amorphous silicon (a-Si:H) layer as a planar PC in order to couple incident light into Bloch modes standing over the light line, so as to control the photon lifetimes [32-35,]. Based on this concept, PC-assisted a-Si:H solar cells were designed [36], and preliminary experimental results have been obtained [15, 34].Similar approaches have been studied for organic solar cells, showing also a larger absorption [37-38].

Another attractive light trapping scheme is based on diffraction gratings in thin film solar cells. Diffraction gratings present a great potential as they can be used either as advanced back reflectors to increase both the path length and the spectral density of optical modes at long wavelengths [23,40-41] or as front anti-reflectors to decrease the global reflection and to enhance transmitted grating orders [42-49], or as proposed very recently, as combined back reflector and front anti-reflector in a cell, by patterning different layers [2,3,49]. A diffraction grating [50] is an optical component with a periodic structure, which splits and diffracts light into several beams travelling in different directions. The directions of these beams depend on the period of the grating and the wavelength of the light so that the grating acts as the dispersive element.

When the grating is located on the surface of a thin film, it enables the coupling of the incident light into the quasi-guided mode of the thin film. In that sense, the concept of 1D and 2D diffraction grating in thin films is close to the concept of 1D and 2D PCs.

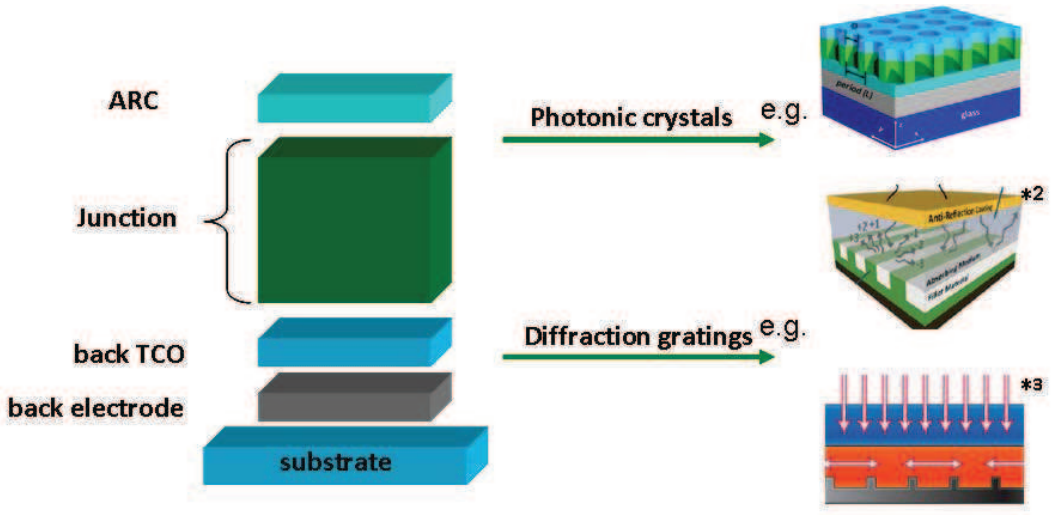

Fig. 2.3. Light trapping schemes, such photonic crystals and diffraction gratings, were considered in thin film silicon solar cells

Based on previous light trapping schemes and typical solar cells schematics, as well as absorption enhancement strategies in a silicon active layer, the ARC, p-n junction, back TCO and electrodes could be patterned or textured as diffraction gratings and photonic crystals [51-55], as displayed on Fig. 2.3. Such light trapping approaches will be developed in this thesis.

References and links

[1] J. Poortmans and V. Arkhipov, *Thin film solar cells: fabrication, characterization and applications*, **8**. John Wiley & Sons Inc, 2006.

[2] J. G. Mutitu, S. Shi, C. Chen, T. Creazzo, A. Barnett, C. Honsberg, and D. W. Prather, "Thin film solar cell design based on photonic crystal and diffractive grating structures," Opt. Express **16**, 15238–15248 (2008).

[3] R. Dewan, M. Marinkovic, R. Noriega, S. Phdadke, A. Salleo, and D. Knipp, "Light trapping in thin-film silicon solar cells with submicron surface texture," Opt. Express **17**, 23058-23065 (2009).

[4] C. Honsberg and S. Bowden, Photovoltaics CDROM.

[5] M. Berginski, J. Hupkes, M. Schulte, G. Schope, H. Stiebig, B. Rech and M. Wuttig, "The effect of front ZnO: Al surface texture and optical transparency on efficient light trapping in silicon thin-film solar cells," J.Appl. Phys. **101**, 074903 (2007).

[6] J. Buencuerpo, L.E. Munioz-Camuniez, M.L. Dotor and P.A. Postigo, "Optical absorption enhancement in a hybrid system photonic crystal–thin substrate for photovoltaic applications," Opt. Express **20**, A452–A464 (2012).

[7] S. S. Lo, C. C. Chen, F. Garwe, and T. Pertch, "Broad-band anti-reflection coupler for a:Si thin-film solar cell," J. Phys. D Appl. Phys. **40**, 754–758 (2007).

[8] O. Isabella, A. Campa, MCR Heijna, WJ Soppe, AJM Van Erven, RH Franken, H. Borg, and M. Zeman, "Light scattering properties of surface-textured substrates for thin-film solar cells," Proceedings of the 23rd EUPVSEC, Session 3AV, **1**, 476–481.

[9] M. A. Green, *Silicon Solar Cells, Advanced Principles and Practice*, University of New South Wales: Center for Photovoltaic Devices and Systems, University of New South Wales, 1995.

[10] J. Müller, B. Rech, J. Springer, and M. Vanecek, "TCO and light trapping in silicon thin film solar cells," Sol. Energy **77**, 917-930 (2004).

[11] A. Marsh and J. Inkson, "Scattering matrix theory of transport in heterostrucutres," Semiconductor Science and Tech. **1**, 285-290 (1986).

[12] R. Brendel and A. Goetzberger, *Thin-film crystalline silicon solar cells: physics and technology*, Weinheim: Wiley-VCH, 2003.

[13] R. Biswas and C. Xu, "Nano-crystalline silicon solar cell architecture with absorption at the classical 4n2 limit," Opt. Express **19**, 664-672 (2011).

[14] E. Yablonovitch and G. D. Cody, "Intensity enhancement in textured optical sheets for solar cells," IEEE Trans. Electron. Dev. **29**, 300–305 (1982)

[15] X. Meng, G. Gomard, O. El Daif, E. Drouard, R. Orobtchouk, A. Kaminski, A. Fave, M. Lemiti, A. Abramov, P. Roca i Cabarrocas, and C. Seassal, "Absorbing photonic crystals for silicon thin-film solar cells: Design, fabrication and experimental investigation," Sol. En. Mat. Sol. Cells **95**, 32–38 (2011).

[16] X. Meng, V. Depauw, G. Gomard, O.EI Daif, C. Trompoukis, E. Drouard, C. Jamois, R. Orobtchouk, A. Fave, F. Dross, I. Gordon, and C. Seassal, "Absorbing photonic crystals for mono-crystalline silicon thin film solar cells," Proceedings of SPIE, **8425**, 84250R (2012).

[17] X. Meng, V. Depauw, G. Gomard, O.EI Daif, C. Trompoukis, E. Drouard, C. Jamois, R. Orobtchouk, A. Fave, F. Dross, I. Gordon, and C. Seassal, Design, "Design, fabrication and optical characterization of photonic crystal assisted thin film monocrystalline-silicon solar cells," Opt. Express **20**, A465-A475 (2012).

[18] X. Meng, E. Drouard, G. Gomard, A. Fave, and C. Seassal, "Combined front and back diffraction gratings for broad band light trapping in thin film solar cell," Opt. Express **20**, A560-571 (2012).

[19] X. Meng, V. Depauw, G. Gomard, O. El Daif, C. Trompoukis, E. Drouard, A. Fave, F. Dross, I. Gordon, and C. Seassal, "Design and fabrication of

photonic crystals in epitaxy-free silicon for ultrathin solar cells," Proc. SPIE, **8312**, 831207 (2011).

[20] Claus Heine and Rudolf H. Morf, "Submicrometer gratings for solar energy applications," Appl. Opt. **34**, 2476–2482 (1995).

[21] M.Berginski, J.Hupkes, et al, "The effect of front ZnO:Al surface texture and optical transparency on efficient light trapping in Silicon thin film solar cells" J. Appl. Phys. **101**, 074903 (2007).

[22] J. Müller, B. Rech, J. Springer and M. Vanecek, "TCO and light trapping in silicon thin film solar cells", Sol. Energy **77**, 917-930 (2004).

[23] J. Chen, Q. K. Wang, and H. H. Li, "Microstructured design of metallic diffraction gratings for light trapping in thin-film silicon solar cells," Opt. Com. **283**, 5236-5244 (2010).

[24] S. John, "Strong localization of photons in certain disordered dielectric superlattices," Phys. R. Lett. **58**, 2486–2489 (1987).

[25] E. Yablonovitch, "Inhibited spontaneous emission in solid-state physics and electronics," Phys. R. Lett. **58**, 2059–2062 (1987).

[26] A. Bielawny, C. Rockstuhl, F. Lederer, and R. B. Wehrspohn, "Intermediate reflectors for enhanced topcell performance in photovoltaicthin-film tandem cells," Opt. Express **17**, 8439–8446 (2009).

[27] A. Chutinan and S. John, "Light trapping and absorption optimization in certain thin-film photonic crystal architectures," Phys. Rev. A **78**, 023825 (2008).

[28] E.R. Dedman, D.N. Sharp, A.J. Turberfield, C.F. Blanford, and R.G. Denning, "Photonic crystals with a chiral basis by holographic lithography," Photonics and Nanostructures - Fundamentals and Applications **3**, 79–83 (2005).

[29] O. El Daif, E. Drouard, G. Gomard, A. Kaminski, A. Fave, M. Lemiti, S. Ahn, S. Kim, P. Roca i Cabarrocas, H. Jeon, and C. Seassal, "Absorbing one-dimensional planar photonic crystal for amorphous silicon solar cell," Opt. Express **18**, A293-A299 (2010).

[30] L.Zeng, P.Bermel, Y.Yi, B.A.Alamariu, K.A.Broderick, J.Liu, C.Hong, X.Duan, J.Joannopoulos, and L.C.Kimerlingv, "Demonstration of enhanced absorption in thin film Si solar cells with textured photonic crystal back reflector," Appl. Phys. Lett. **93**, 221105 (2008).

[31] R. Biswas and C. Xu, "Nano-crystalline silicon solar cell architecture with absorption at the classical 4n2 limit," Opt. Express **19**, 664-672 (2011).

[32] L.Zeng, P.Bermel, Y.Yi, B.A.Alamariu, K.A.Broderick, J.Liu, C.Hong, X.Duan, J.Joannopoulos, and L.C.Kimerlingv, "Demonstration of enhanced absorption in thin film Si solar cells with textured photonic crystal back reflector," Appl. Phys. Lett. **93**, 221105 (2008).

[33] J. Gjessing, E. S. Marstein, and A. S. Sudbø, "2D back-side diffraction grating for improved light trapping in thin silicon solar cells," Opt. Express **18**, 5481-5495 (2010).

[34] G. Gomard, X. Meng, E. Drouard, K. El Hajjam, E. Gerelli, R. Peretti, A. Fave, R. Orobtchouk, M. Lemiti, and C. Seassal, "Light harvesting by planar photonic crystals in solar cells: the case of amorphous silicon," J. Opt. **14**, 024011 (2012).

[35] F. J. Beck, A. Polman, and K. R. Catchpole, "Tunable light trapping for solar cells using localized surface plasmons," J. Appl. Phys. **105**, 114310 (2009).

[36] R. A. Pala, J. White, E. Barnard, J. Liu, and M. L. Brongersma, "Design of plasmonic thin-film solar cells with broadband absorption enhancements," Adv. Mater. **21**, 3504-3509 (2009).

[37] D. Duché, L. Escoubas, J.J. Simon, P. Torchio, W. Vervisch, and F. Flory "Slow Bloch modes for enhancing the absorption of light in thin films for photovoltaic cells," Appl. Phys. Lett. **92**, 193310 (2008).

[38] D. Duché, E. Drouard, JJ Simon, L. Escoubas, P. Torchio,J. Le Rouzo, and S. Vedraine, "Light harvesting in organic solar cells," Sol. En. Mater. Sol. Cells **95**, 18–25 (2011).

[39] A.Bielawny, C.Rockstuhl, F.Lederer, and R. B.Wehrspohn, "Intermediate reflectors for enhanced top cell performance in photovoltaic thin-film tandem cells," Opt. Express **17**, 8439-8446 (2009).

[40] M. Peters, J. C. Goldschmidt, T. Kirchartz, and B. Bläsi, "The photonic light trap--improved light trapping in solar cells by angularly selective filters," Sol. En. Mat. Sol. Cells **93**, 1721-1727 (2009).

[41] J. S Cho, S. Baek, and J. C. Lee, "Surface texturing of sputtered ZnO:Al/Ag back reflectors for flexible silicon thin-film solar cells," Sol. En. Mat. Sol. Cells **95**, 1852–1858 (2011).

[42] H. Sai, H. Fujiwara, and M. Kondo, "Back surface reflectors with periodic textures fabricated by self-ordering process for light trapping in thin-film microcrystalline silicon solar cells," Sol. En. Mat. Sol. Cells **93**, 1087 (2009).

[43] M. Vanecek, O. Babchenko, A. Purkrt, J. Holovsky, N. Neykova, A. Poruba, Z. Remes, J. Meier and U Kroll, "Nanostructured three-dimensional thin film silicon solar cells with very high efficiency potential," Appl. Phys. Lett. **98**, 163503 (2011).

[44] C. G. Granqvist and A. Hultåker, "Transparent and conducting ITO films: new developments and applications," Thin Solid Films **411**, 1 (2002).

[45] J. Y. Chen and K. W. Sun, "Enhancement of the light conversion efficiency of silicon solar cells by using nanoimprint anti-reflection layer," Sol. En. Mat. Sol. Cells **94**, 629–633 (2010).

[46] D. Zhou and R. Biswas, "Photonic crystal enhanced light-trapping in thin film solar cells," J. Appl. Phys. **103**, 093102 (2008).

[47] Y. M. Song, J. S. Yu, and Y. T. Lee, "Antireflective submicrometer gratings on thin-film silicon solar cells for light-absorption enhancement," Opt. Lett. **35**, 276–278 (2010).

[48] S. H. Zaidi, J. M. Gee, and D. S. Ruby, "Diffraction grating structures in solar cells," in Twenty-Eighth IEEE Photovolt. Spec. Conf., 395-398 (2000).

[49] K. X. Wang, Z. Yu, V. Liu, Y. Cui, and S. Fan, "Absorption enhancement in ultrathin crystalline silicon solar cells with antireflection and light-trapping nanocone gratings," Nano Lett. **12**, 1616–1619 (2012).

[50] D.C. O'Shea, *Diffractive optics: design, fabrication, and test*, Society of Photo Optical **62**, (2004).

[51] J. Pla, M. Tamasi, R. Rizzoli, M. Losurdo, E. Centurioni, C. Summonte, and F. Rubinelli, "Optimization of ITO layers for applications in a-Si/c-Si heterojunction solar cells," Thin Solid Films **425**, 185-192 (2003).

[52] G.G. Granqvist, A.Huiltaker, "Transparent and conducting ITO films: new developments and applications," Thin Solid Film **411**, 1-5 (2002).

[53] F. Duerinckx and J. Szlufcik, "Defect passivation of industrial multi-crystalline solar cells based on pecvd silicon nitride," Sol. En. Mat. Sol. Cells **72**, 231-246 (2002).

[54] M. Zeman, R. van Swaaij, JW Metselaar, and REI Schropp, "Optical modeling of a-Si: H solar cells with rough interfaces: Effect of back contact and interface roughness," J. Appl. Phys. **88**, 6436 (2000).

[55] K. Tabuchi, W.W. Wenas, A. Yamada, M. Konagai, and K. Takahashi, "Optimization of ZnO films for amorphous silicon solar cells," Jpn. J. Appl. Phys. **32**, 3764–3769 (1993).

Chapter 3

Simulation, fabrication and characterization methodologies for Photonic crystal and diffraction grating assisted thin film silicon solar cells

3.1 Introduction

In this chapter, we will introduce design methodologies used in this thesis to obtain optimized absorption in solar cells, using diffraction gratings and PCs. Based on designs, the main challenge for us is how to generate these patterns in labs. Therefore, several fabrication technologies and processes, such as deposition technologies, lithographic and etching methods, will be briefly described. After the fabrication of these patterned stacks, the measurement methods are extremely important to characterize their topography, optical properties as well as their electrical properties.

3.2 Design methodologies

In metrology and in optical design systems, rigorous simulations are needed to be guideline for the realization. If the structures include patterns at the scale of the wavelength or smaller, specific methods are required. At the moment, the Rigorous Coupled Wave Analysis (RCWA) [1-2], the Finite Difference Time Domain method (FDTD) [3] and the Finite Element Method (FEM) [4-5] are three main methods to obtain the optical designs for various applications such photovoltaics assisted solar cells. They are rigorous methods used solving the Maxwell equations.

FDTD is a numerical method to solve time-dependant Maxwell's equation using finite-difference approximation of partial derivatives. Since its introduction by Yee cell [1], FDTD evolved into very effective and arguably the most popular numerical technique for electromagnetic problems [3].

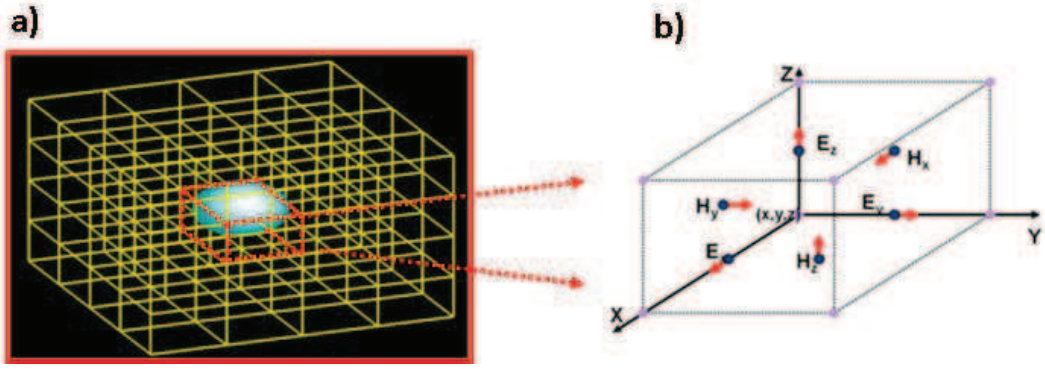

*Fig. 3.1. (**a**) Yee-cell mesh and (**b**) a Yee-cell's algorithm*

RCWA is a semi-analytical method in computational electromagnetics that is most typically applied to solve scattering from periodic dielectric structures.

These two methods have been used in this work. The choice relies mainly on the computation time and memory requirement. Indeed, for a linear medium, Maxwell's equations can be solved either in the time-domain or the frequency domain. The advantage of using methods in the time-domain is that it can explicitly solve time dependant phenomena such as broad band pulse propagation. Single simulation is enough to solve for a broad range of frequencies. This is still true when the material chromatic dispersion has to be taken into account, even if it is more complex and resource consuming: the indices are time dependant, and the response of the structure becomes a convolution On the other hand, it remains straightforward using a frequency domain method, but the computation depends linearly on the spectral resolution. Thus, the structures with c-Si has been computed mainly using FDTD, since this low absorbing material will imply sharp resonances in the spectral response, so needs to be calculated using a large spectral resolution.

In this thesis, we used the FDTD software available in the commercial packages Lumerical [6]. The RCWA is conducted by using CAMFR [1], and more specifically its package GARCLED [2].

The theoretical study in an hydrogenated amorphous silicon (a-Si:H) ultra-thin film solar cells in Chapter.4 has been conducted by using CAMFR / GARCLED. The AM1.5G solar spectral intensity distribution was taken into account over the 300-720 nm spectral range (See Fig. 3.2 green region). These bounds roughly and respectively correspond to the lower limit of the solar spectrum and the a-Si:H gap.

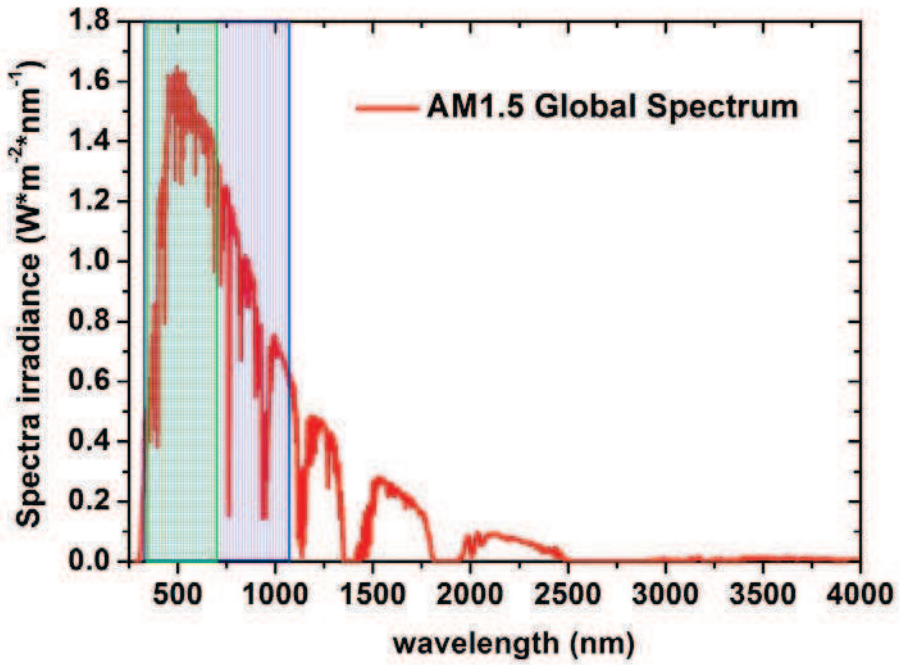

Fig. 3.2. AM1.5G solar spectrum intensity distribution

About the designs in crystalline silicon (c-Si) thin film solar cells for the Chapter.5 and 6, the optical designs are based on the FDTD method. In this work, it has been used to calculate the absorption of complete patterned solar cells, and TCO, metal contactor layers, as well as the specific absorption in the junction layers. The optical performance of the structures will be indicated by their integrated absorption, a percentage defined by the ratio between the absorbed optical power over the incident optical power in the whole of interested spectral range. The AM1.5G solar spectrum intensity distribution was taken into account over the 300-1100 nm spectral range under normal incidence, shown in the blue region of Fig. 3.2. These boundaries roughly and respectively correspond to the

lowest wavelength of the solar spectrum and the c-Si gap. The refractive indexes of the materials, ITO, active layers, are all from ellipsometric measurement.

For a better understanding of the influence of the geometrical parameters of the structures, and thus to enable a rough optimization, Lumercial allows the analysis of the reflected / transmitted light in various order of diffractions, similarly to using RCWA. In this section, we will focus on how to design, create and simulate a complete solar cell step by step by FDTD in Lumerical, and then how to calculate and collect simulated data. We consider a complete solar cell in the example shown in Fig. 3.3.

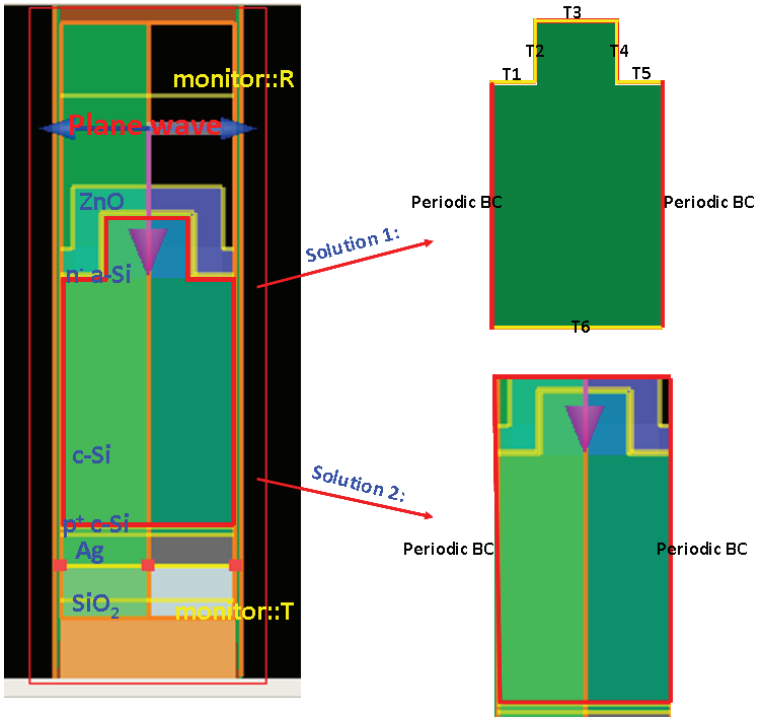

Fig. 3.3. Structure schematic view in FDTD solution with 2 solutions to calculate absorption in c-Si active layer. The solar cell stack is composed of, from back to front, glass substrate, Ag, p^+ c-Si, and active c-Si layer, as well as a n^+ *a-Si:H and ZnO overlaid on the patterned c-Si .*

In order to get the absorption in the whole designed structure, a reflection power monitor (*R*) and a transmission power monitor (*T*) are set far above and below the structure. Therefore, the absorption (Abs) in the whole structure could

be calculated as: *Abs (λ) = 1 – R (λ) – T (λ)*. Meanwhile, we would like to determine the absorption in the ZnO or to calculate the absorption in the active c-Si layer.

In the first solution, as introduced in Fig. 3.1, several power monitors (T1~T6) are set above and below the c-Si layer, to measure the flux of the Poynting vector across each monitor. The absorption in c-Si is [(T1+T2+T3+T4+T5) - T6].

The second solution requires more computational resources and time but appears to be more stable. The absorption Pabs is calculated as: [7]

$$Pabs = 0.5real(i\varpi \vec{E}\square\vec{D}) = -0.5\varpi \mid E \mid^2 imag(\varepsilon) \qquad (1)$$

At a given frequency, the whole absorption in the active layer is thus obtained through the integration of the previous equation. In order to calculate the absorption, we need to know the electric field intensity and the imaginary part of the permittivity, which could be measured in the Lumerical by using a specific script, which is described in Annex.B.

For the diffraction grating analysis in the Lumerical, the grating functions are used to calculate the direction and intensity of light reflected or transmitted through a periodic structure. To simplify, we will consider a 1D grating in this section (Fig. 3.4).

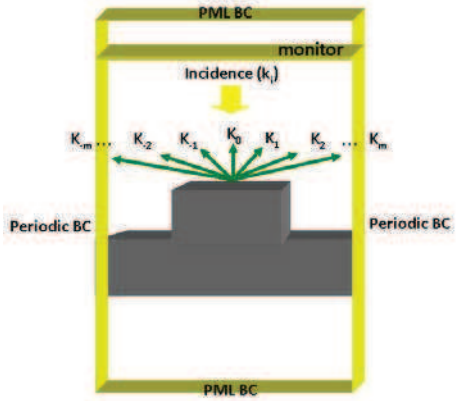

Fig. 3.4. Reflection diffraction grating orders of 1D grating structure

The order directions of a 1D grating can be calculated from the well known grating equation. For our purposes, it is more convenient to re-write this equation in terms of the wave vector *k*:

$$\sin\theta_m + \sin\theta_i = +m\lambda / \Lambda n \quad \rightarrow \vec{k}_m = \vec{k}_i + m\frac{2\pi}{\Lambda} \tag{2}$$

where n is the refractive index, λ is the wavelength in vacuum, Λ is the grating period, m is the diffraction order (0, ±1, ±2…), θ_i is the incident angle, θ_m is the diffraction angle for the m^{th} order.

The grating order direction is defined entirely by the device period, the source wavelength and angle of incidence, and the background refractive index. The grating order direction can be calculated without running a simulation; however the simulation must first be performed in order to obtain necessary information such as the dimensions and period of the structure. After running a FDTD simulation, the grating commands available in Lumerical can be used to calculate the fraction of power that is scattered in each direction. They rely on a technique similar to a far field projection to calculate what fraction of near field power propagates in each grating order direction. The fraction of power transmitted to each grating order can be calculated at all frequency points recorded by the monitor. Meanwhile, the number and angle and the intensity of propagating grating orders are calculated by scripts, which are written in Annex.C.

3.3 Fabrication techniques

3.3.1 Preparation of absorbing silicon layers

a. PECVD

The plasma enhanced chemical vapor deposition (PECVD) at 200 °C will be used for the fabrication of nanostructured a-Si:H cells [9]. This involves the dissociation of silane and hydrogen gas mixtures for the obtaining of intrinsic films, while p-type and n-type doping can be

achieved by adding diborane or phosphine. These fabricated a-Si:H solar cell stacks were fabricated at Laboratoire de Physique des Interfaces et Couches Minces (LPICM) and will be used in Chapter. 4.

b. Epifree c-Si thin film

In order to obtain thin film crystalline silicon cells, various kinds of layers, e.g. mono-, poly-, or micro-crystalline silicon, could be generated by changing deposition conditions (substrate, temperature, pressure). However, simple and low-cost conditions only lead to a lower-quality material and therefore to lower solar-cell performances. Therefore, novel techniques were introduced to generate mono-crystalline silicon layers. In particular, the photovoltaic group in IMEC (Belgium) developed the so-called Epifree process [8]. This novel technique will be used to obtain mono c-Si thin film solar cell in this thesis.

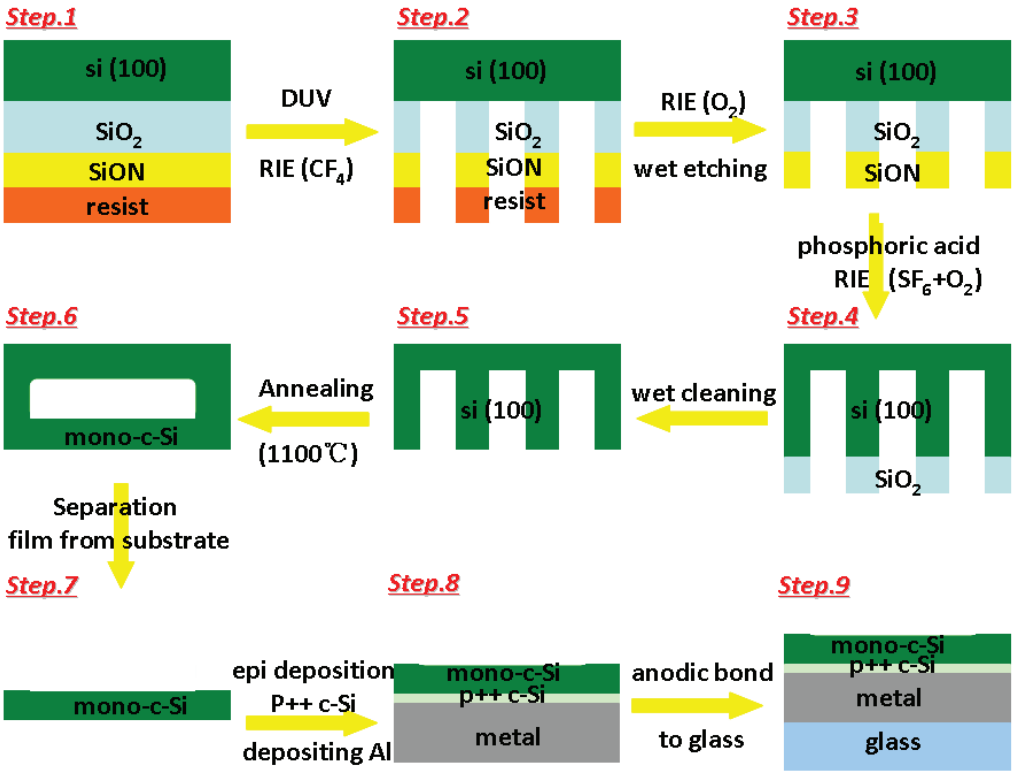

Fig. 3.5. The synthetic process to generate mono crystalline silicon

In this process (Shown on Fig. 3.5), the original substrate is p-type Si (100). After cleaning the substrate, a 500 nm thick SiO_2 is deposited as a mask layer, and then a 50 nm thick SiON is overlaid to generate an ARC. This improves the process resolution by avoiding parasitic light reflections. Then a particular UV sensitive photoresist is spun on the wafer (Step.1). After patterning resist by deep UV light, the SiON and SiO_2 are etched by CF_4 plasma (Step.2). The resist is then stripped by O_2 plasma (Step.3). After that, SiON is cleaned by dipping into phosphoric acid and the 3 μm Si is etched by mixed gases (SF_6 and O_2) plasma through the patterned SiO_2 mask (Step.4), which is then stripped by wet cleaning (Step.5). Then the patterned Si is annealed above 1100 ℃ to generate mo crystalline silicon (Step.6). Then mono c-Si film is separated from the Si substrate (Step.7). Additionally, on this mono c-Si, a thin layer of p^{++} c-Si is deposited by homo-epitaxy, which leads to a good rear surface passivation. Finally, a metal contactor (Al or Ag) layer is deposited (Step.8) and anodic bonding to glass substrate is performed at high voltage (Step.9). Such kind of samples, prepared at IMEC, will be used in Chapter.5.

3.3.2 Laser holographic lithography

Obtaining well defined and uniform nano-scale designed structures over wide areas is very challenging. Recent methods such as electron beam lithography (EBL) [10-12], nano-imprint lithography (NIL) [13-15] and laser holography lithography (LHL) [16-17] or colloidal lithography [18] have been extensively developed and widely used for patterning. The EBL is capable of producing arbitrarily shaped particles with good feature and various sizes which are ideal for prototyping and lithography reticule generation. However, the cost of the instrument and the low throughput rate of EBL make this technique inappropriate for PV applications. NIL method can be used to fabricate large areas, relatively simple way, with low cost, and excellent scalability. Nevertheless, due to the cost of NIL molds, this method is not appropriate for extensive research and

prototyping where a wide range of photonic structure parameters need to be tested. LHL combines its moderate cost with a high resolution, high throughput and design flexibility. Its main limitation is that it is only suited to periodic patterns generation, and that photoresist should be used. We selected this method to generate the PCs and diffraction grating structures presented in this thesis [14, 16-17].

LHL was first proposed and implemented to fabricate one- or two-dimensional (2D) hexagonal patterns in a photosensitive polymer [19], which subsequently served as an etching mask for transfer to a high-index substrate. This technique was extended by Campbell et al. [17] and Shoji et al. [20], by introducing up to two additional laser beams to create 3D structures.

The general sequence of steps for a typical LHL process is as follows: substrate preparation, photoresist spin coating, post-apply-bake, exposure, post-exposure bake, development, and hard bake. A resist strip is the final operation in the final operation in the lithographic process, after the resist pattern has been transferred into the underlying layer via etching or ion implantation. For each layer of stack and pattern geometrical parameter, specific parameters should be adjusted. This will be more extensively discussed in Chapters.4.

It can be noticed that holographic lithography can be improved thanks to the use of phase masks, allowing the fabrication of more complex patterns. It can even be used for a continuous writing, and thus becomes a promising technique to write very large area gratings [21]

3.3.3 Reactive ion etching and Inductivity coupled plasma etching

Reactive ion etching (RIE) [22-23] and Inductivity coupled plasma (ICP)-RIE are widely used technologies for micro- and nanostructuring. They use chemically reactive plasmas to etch materials. As shown in Fig. 3.6, a gas or a gas mixture flows into the reactor where a RF voltage is applied between two electrodes. The voltage causes free electrons to oscillate and the induced dissociation of gas

molecules generates the plasma. After the plasma is created, a self-bias builds up between the plasma center and the electrodes, which accelerates ions towards the sample surface where they activate chemical etching by energy transfer to neutral particles.

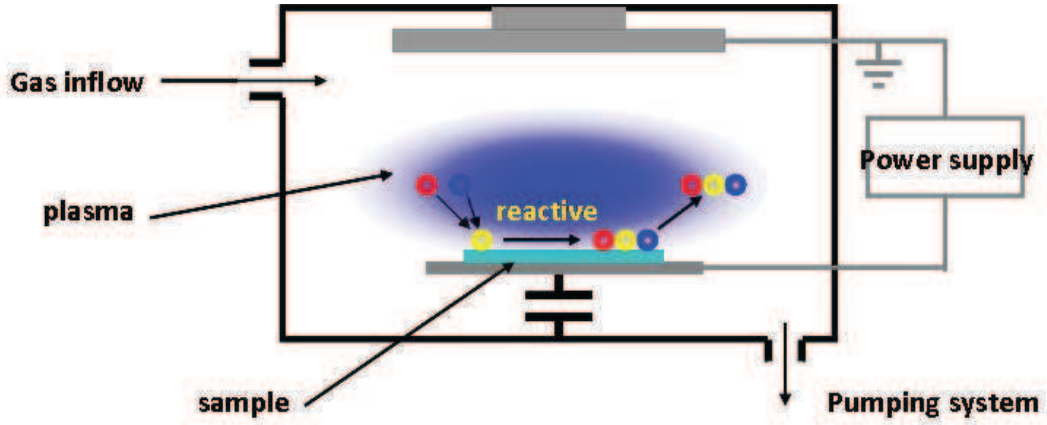

Fig. 3.6. Schematic of RIE and ICP etching system

Indeed, after patterning 1D or 2D on resist, it should be transferred into the unpatterned stack. A deposited layer could also be used as hard mask during the RIE, if it provides a high-enough selectivity. Among the wide choice of possible materials for this purpose, we have chosen a silica mask as the deposited layer. This kind of hard mask for sub-micron patterning by RIE has been developed in our laboratory. The hard mask (generally SiO_2) does not only play a role of protection layer against the resist penetration into the pores, but also provides the homogenous surface necessary to obtain a high quality resist mask by spin-coating. Finally, RIE and Inductivity Coupled Plasma etching (ICP) processes can be used to transfer into the active layer (a-Si:H or c-Si). Moreover, if necessary, the remaining silica mask can be easily removed RIE or wet etching. The details of each technological step of the patterning processes will be described in the Chapter.4 in details.

3.4 Characterization methodologies

3.4.1. Topography methods

The topography and profile of the patterned structures is normally observed by scanning electron microscopy (SEM) [24], Atomic Force Microscope (AFM) [25] and Transmission electron microscopy (TEM) [26-27]. The homogeneity and the lattice parameters, such as period, width of 1D lines or diameter of 2D square holes and the etching depth could be measured by SEM directly and by a profile observation through an angle tilted SEM observation. Combined with the SEM, AFM could also be used to get the topography and lattice parameters of patterning, as well as the roughness of patterned stacks. In addition, the TEM has been used in specific cases to check carefully cross section profiles.

3.4.2. Optical characterization methodology

In order to determine the optical properties of the patterned stack presented stacks, the absorption measurements were performed using an integrating sphere [28-29]. In these experiments, the sample is illuminated by unpolarized light, so as to perform reflectance (R) and transmittance (T) measurements with a ~ 1 mm² spot size and with an 8° angle of incidence, as imposed by the integrating sphere measurement (Fig. 3.7). The incident angle with 8° is intent on obtaining R and T by integrating sphere. The absorption $A(\lambda) = 1 - R(\lambda) - T(\lambda)$ is then simply derived. The absorption of the whole a-Si:H patterned stack and c-Si patterned stack were measured over 300-720 nm and 300-1100 nm with 10 nm step respectively.

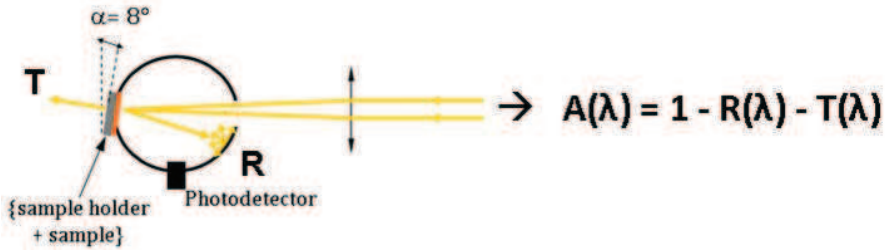

Fig. 3.7. Schematic of integrating sphere

For the solar cells investigation, it is required that the absorption exhibits a moderate dependence on the incident light angle α. Therefore, the relationship between the angle of incidence and the absorption in the patterned stack will be also measured in the integrating sphere through changing α.

References and links

[1] Developped by Ghent University, see http://camfr.sourceforge.net/.

[2] M. G. Moharam and T. K. Gaylord, Rigorous coupled-wave analysis of planar-grating diffraction, J. Opt. Soc. Am. **71**, 811–818 (1981).

[3] A. Taflove, S. C. Hagness, *Computational Electrodynamics: The Finite-Difference Time- Domain Method*, Artech House, Sec. Edition.

[4] O. C. Zienkiewicz, R. L. Taylor et al, *The finite element method for solid and structural mechanics*, 2005.

[5] R L.Taylor, *The finite element method*, University of California, 2005.

[6] http://www.lumerical.com/

[7] http://docs.lumerical.com/en/fdtd/user_guide_absorption_1.html.

[8] V. Depauw, Y. Qiu, K. Van Nieuwenhuysen, I. Gordon, and J. Poortmans, "Epitaxy-free monocrystalline silicon thin film: first steps beyond proof-of-concept solar cells," Progress in Photovoltaics: Research and Applications **19**, 844-850 (2010).

[9] C. Godet and P. Roca i Cabarrocas, "Role of si–h bonding in a-Si: H metastability," J. appl. Phys. **80**, 97–102 (1996).

[10] R. Ruiz, H.M. Kang, F.A. Detcheverry, E. Dobisz, D.S. Kercher, T.R. Albrecht *et al,* "Density multiplication and improved lithography by directed block copolymer assembly," Science **321**, 936-939(2008).

[11] T. H. P. Chang, Proximity effect in electron-beam lithography, J. Vac. Sci. Technol. **12**, 1271 (1975).

[12] W. Chen and H. Ahmed, "Fabrication of 5–7 nm wide etched lines in silicon using 100 keV electron-beam lithography and polymethylmethacrylate resist," Appl. Phys. Lett. **62**, 1499 (1993).

[13] Juha M. Kontio, Janne Simonen, Juha Tommila, and Markus Pessa, "Arrays of metallic nanocones fabricated by uv-nanoimprint

lithography," Microelectronic Engineering, 11th SEMATECH Surface Preparation and Cleaning Conference, **87**, 1711 – 1715 (2010).

[14] Choon-Gi Choi, Chul-Sik Kee, and Helmut Schift, "Fabrication of polymer photonic crystal slabs using nanoimprint lithography," Current Applied Physics **6**, e8 – e11, 2006.

[15] A. Tukiainen, J. Viherial and T. Niemi, T. Rytkonen, J. Kontio, and M. Pessa, "Selective growth experiments on gallium arsenide (100) surfaces patterned using uv-nanoimprint lithography," Microelect. J. **37**, 1477–1480 (2006).

[16] W. Bogaerts, P. Dumon, D. Taillaert, V. Wiaux, S. Beckx, B. Luyssaert, J. Van Campenhout, D. Van Thourhout, and R. Baets, "Soi nanophotonic waveguide structures fabricated with deep uv lithography," Photonics and Nanostructures- Fundamentals and Applications, **2**, 81 – 86 (2004).

[17] M. Campbell, D. N. Sharp, M. T. Harrison, R. G. Denning, and A. J. Turberfield, "Fabrication of photonic crystals for the visible spectrum by holographic lithography," Nature **404**, 53–56 (2000).

[18] S. M. Yang, S. G. Jang, D. G. Choi, S. Kim, and H. K. Yu, "Nanomachining by colloidal lithography," Small **2**, 458–475 (2006).

[19] L. Wu, Y. Zhong, C.T. Chan, K.S. Wong, and G.P. Wang, "Fabrication of large area two-and three-dimensional polymer photonic crystals using single refracting prism holographic lithography," Appl. Phys. Lett. **86**, 241102 (2005).

[20] Satoru Shoji and Satoshi Kawata, "Photofabrication of three-dimensional photonic crystals by multibeam laser interference into a photopolymerizable resin," Appl. Phys. Lett. **76**, 2668–2670 (2000).

[21] V. Gate, Y. Jourlin, M. Langlet, F. Vocanson, O. Parriaux, G. Bernaud, C. Veillas and A. Cazier, "New low-cost high-efficiency solar module: diffracting deflector module," Photonics for solar energy systems IV. Book Series: Proceedings of SPIE, **8438**, 84380W (2012)

[22] Jansen H, Gardeniers H, de Boer M, Elwenspoek M and Fluitman J, "A survey on the reactive ion etching of silicon in microtechnology," J. Micromech. Microeng. **6**, 14-28 (1996).

[23] S. Grigoropoulos, E. Gogolides, A. D. Tserepi, and A. G. Nassiopoulos, "Highly anisotropic silicon reactive ion etching for nanofabrication using mixtures of SF/sub 6//CHF/sub 3/ gases", J. Vac. Sci. Technol. **15**, 640 (1997).

[24] J. Goldstein, *Scanning electron microscopy and X-ray microanalysis*, **1**, Springer Us, 2003.

[25] G. Binnig, C.F. Quate, and C. Gerber, "Atomic force microscope," Phys. Rev. Lett. **56**, 930–933 (1986).

[26] D.B. Williams and C.B. Carter, *Transmission Electron Microscopy, A Textbook for Materials Science*, Plenum, New York, 1996.

[27] John D. Aiken III and Richard G. Finke, "A review of modern transition-metal nanoclusters: their synthesis, characterization, and applications in catalysis," J. Mol. Cat- A- Che. **145**, 1–44 (1999).

[28] N. B. Nelson and B. B Prézelin, "Calibration of an integrating sphere for determining the absorption coefficient of scattering suspensions," Appl. Opt. **32**, 6710-17 (1993)

[29] J. Zhu, Z. Yu, G. F. Burkhard, C.-M. Hsu, S. T.Connor, Y. Xu, Q. Wang, M. McGehee, S. Fan, and Y. Cui, "Optical absorption enhancement in amorphous silicon nanowire and nanocone arrays," Nano Lett. **9**, 279-282 (2008).

Chapter 4

Fabrication of photonic crystal assisted ultra thin film hydrogenated amorphous silicon solar cells

4.1 Introduction

A hydrogenated amorphous silicon (a-Si:H) is an attractive material since it exhibits a very high absorption coefficient with regards to c-Si [1]. However, the active layer thickness should be as much limited as possible in order to reduce fabrication cost and bulk non radiative recombination. With this respect, increasing the absorption of very thin a-Si:H-based solar cell is necessary to achieve a reasonable conversion efficiency. In 2008, INL proposed a light trapping scheme based on photonic crystals (PCs) structures patterned within the active a-Si:H layer. Active layers have thicknesses of around 100 nm, i.e. lower than the diffusion length of the minority carriers (~0.3 μm) [2]. This approach can lead to a substantial increase of the solar light absorption over a wide optical spectral range, thanks to light collection into planar PC Bloch mode resonances standing over the light line [3-6].

In this chapter, we report on patterning the a-Si:H active layer as a square 2D PC membrane using LHL and Reactive Ion Etching (RIE). The global design of our "photonized" solar cell has been optimized optically by simulation, as it will be recalled in the next section. Its optical properties and the parameters of the PCs membrane which maximize the absorption in the active layer were also discussed. This defines the objectives of the subsequent experimental developments. After presenting the general fabrication process of our patterned cells, the influence of the main LHL (and RIE) parameters is studied, with a view to generate the targeted pattern. The optical properties of the fabricated cells are investigated both experimentally and theoretically, and compared to those of an unpatterned cell.

One of the drawbacks of these PC assisted solar cells might be the additional surface recombination on the etched sidewalls. In order to limit their impact, it will be necessary to passavite efficiently these additive surfaces. Additionally, the PC symmetry is expected to pay an important role on this process. Therefore, as a more prospective work, we will consider PC structures which exhibit different

sidewall area to volume ratios. These include triangle, honeycomb and “square honeycomb” structures. The corresponding 2D PC patterned a-Si:H thin film solar cells are designed and the optical properties are analyzed and compared to the classical square 2D PC.

4.2 Optical design and optimization of « photonized » solar cells

The proposed thin-film solar cells are all made with the same stack deposed on a glass substrate. As shown on Fig. 4.1, it consists, from back to front, of a silver (Ag) layer which acts as a reflector and rear contact; a zinc oxide (ZnO) layer playing the role of an optical spacer, a barrier against the diffusion of silver and a transparent and conductive oxide (TCO), an a-Si:H active layer (p-i-n junction) and finally, a front ITO layer which behaves simultaneously as a TCO and an antireflective layer. A metallic grid deposited on the top TCO layer contributes to the collection of the photogenerated carriers.

The absorbing PC membrane structures are patterned within the a-Si:H layers. Here, we will consider a square symmetry 2D PC membrane structure (see Fig. 4.1), as a basis of “photonized” solar cells. Such a 2D pattern structure is expected to exhibit a higher absorption than its unpatterned equivalent, and behaviours independently of the polarization of the incident light [6].

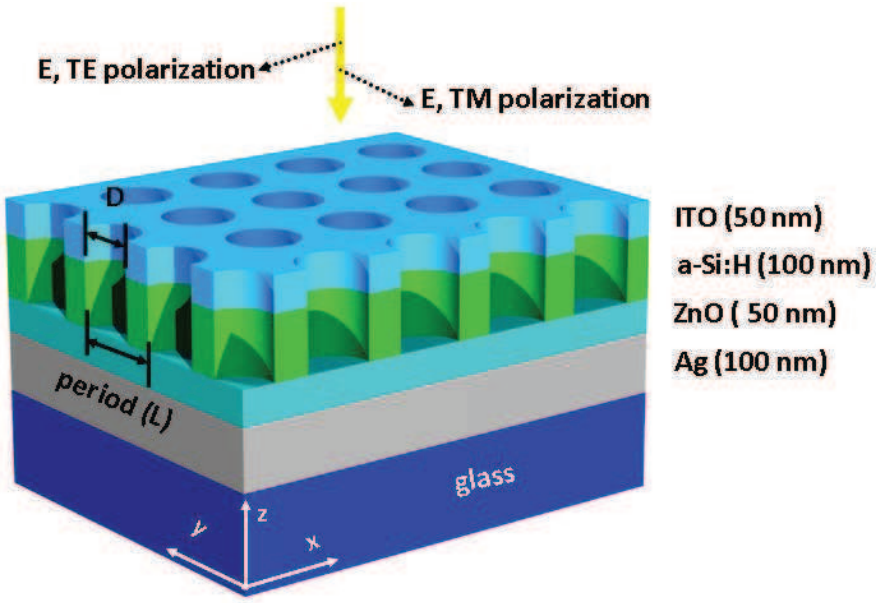

Fig. 4.1. Schematic view of a "photonized" solar cell with a 2D pattern. Photogenerated carriers originating from the a-Si:H active layer are collected through the two surrounding TCO layers, before being transported to the metallic contacts (not shown) disposed on the Ag layer (for the rear contacts) and on the ITO layer, beside the patterned areas (for the top contacts)

It is then possible to adjust the PC membrane parameters, i.e. its period *L* and its *ffair* (= *D/L,* where *D* is the diameter of the holes), in order to maximize the integrated absorption inside the active layer. This theoretical study has been conducted by using CAMFR [7], and more specifically its package GARCLED, based on the Rigorous Coupled Wave Analysis (RCWA) method [8]. The AM1.5G solar spectral intensity distribution was taken into account over the 300-720 nm spectral range, whose bounds roughly and respectively correspond to the lower limit of the solar spectrum and the a-Si:H gap. The thicknesses of the different layers were defined to ensure an efficient collection of the carriers (ITO, a-Si:H and ZnO layers), the long-term stability of the cell (ZnO layer) and a high reflectivity on the back side (Ag layer). Then, we considered values of L and *ffair* achievable using the selected technological processes. More precisely, the configurations of the patterned cell were investigated by scanning simultaneously

L between 0.3 µm and 0.7 µm, and *ffair* between 0.3 and 0.7. The range of the *ffair* ratio has been imposed by the limitations faced when using holographic lithography.

The results of these simulations, displayed on Fig. 4.2, indicate a maximal value for the integrated absorption of about 82 % over the whole patterned cell for *L* = 0.38 µm and *ffair* = 62.5 %.

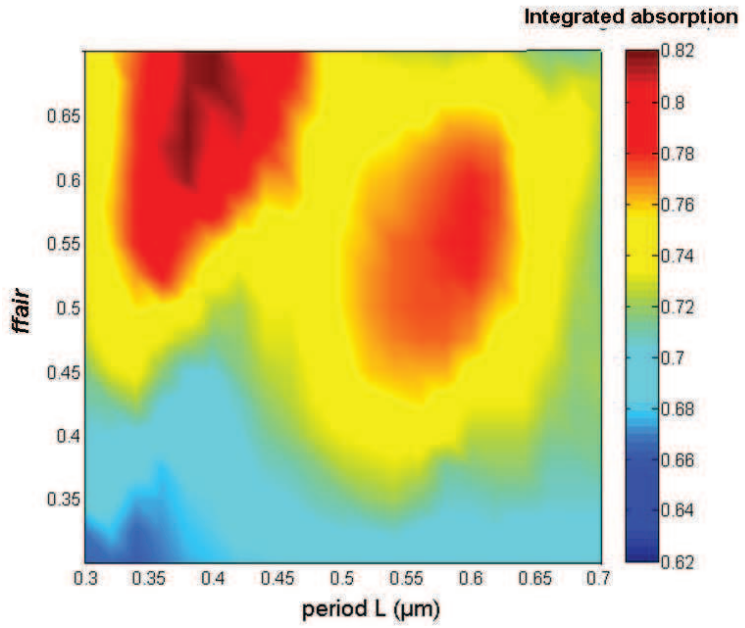

Fig. 4.2. Integrated absorption in the whole patterned cell in function of the period L (x-axis, in µm) and the ffair ratio (y-axis) of the PC membrane

Looking for the integrated absorption in the sole active layer, we found that 65.7 % of the incoming light could be absorbed in the a-Si:H layer for the best configuration obtained. This value represents a 28 % relative increase compared to the case of a similar but unpatterned cell. Provided an efficient passivation of the processed sidewalls of the holes thus created, a subsequent increase of the conversion efficiency is expected for our "photonized" solar cell. It should also be noted that the integrated absorption of the patterned cell is robust with regards to the angle of incidence (α) since at $\alpha = 50$ °,only a 5 % decrease in absolute value is expected compared to its value under normal incidence [9]. Eventually, it can

be appreciated on Fig. 4.2 that highly integrated absorptions can be obtained for a large range of *L* and *ffair* values around the best configuration, which is an important point due to the inherent technological uncertainties. Thus, in practice, and considering the limitations of our LHL setup, periods between 520 nm and 620 nm, and *ffair* ratio between 50 % and 60 % can be targeted for the following.

4.3 Fabrication of PC patterns using laser holographic lithography and reactive ion etching

In this section, we discuss on the steps leading to the patterning of our cells, using LHL and RIE techniques.

The stacks, based on Ag(50nm) /ZnO(100nm) /a-Si:H(130nm) /ITO(60nm) /SiO_2(100nm) layers, which have been processed for this study are based on the design previously presented though actual thicknesses of these layers may be slightly different due to technological uncertainties. The layers were deposited on a glass substrate using the plasma enhanced chemical vapour deposition (PECVD) in a multi-plasma deposition system. Moreover, a 100 nm thick silica layer was added on the top of the stack and acts as a hard mask during the etching of the ITO and a-Si:H layers. Starting from such samples, it is possible to first pattern the hard mask as a 2D PC with a square symmetry via laser holographic lithography, and then to transfer this pattern into the two underlying layers with RIE, as schematized on Fig. 4.3.

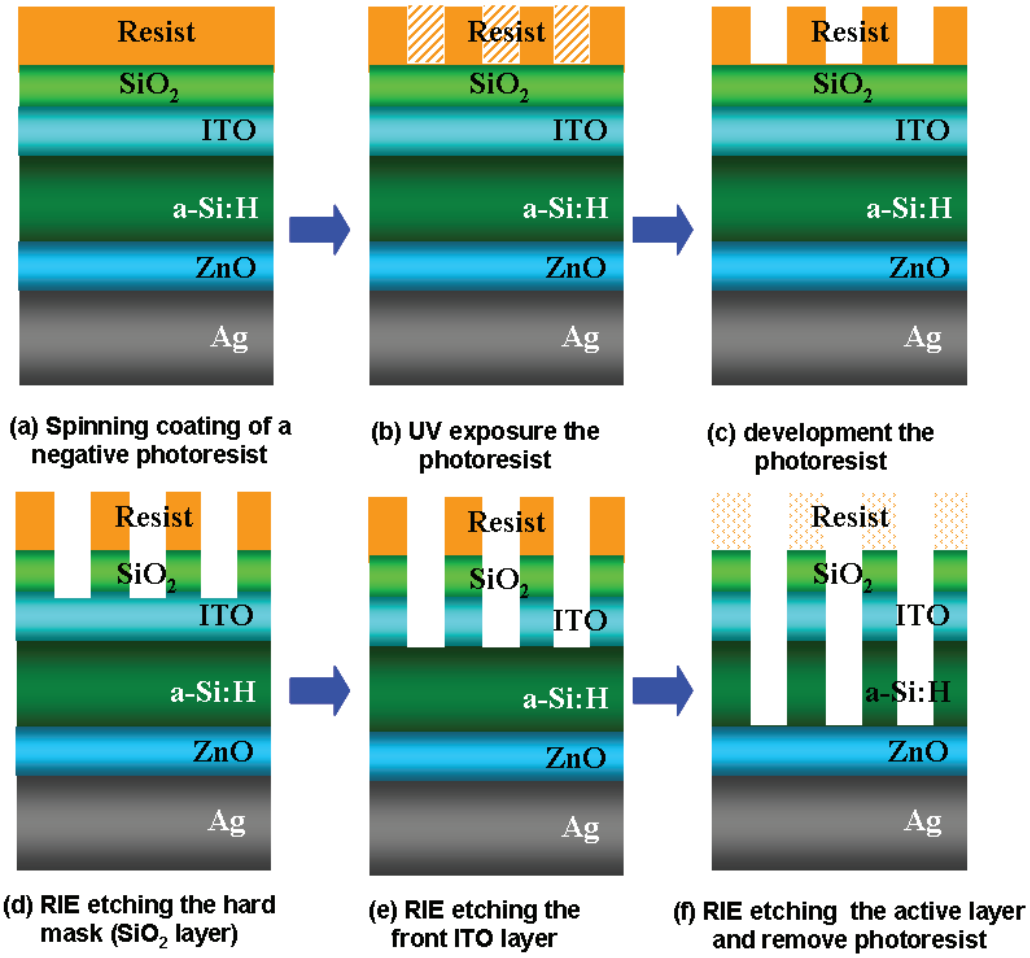

*Fig. 4.3. Main steps of the processes enabling to pattern the active layer as a 2D PC through LHL (**a**), (**b**) and (**c**) and RIE (**d**), (**e**) and (**f**)*

A more detailed description of these techniques will be developed in the following sections. In particular, we will see how the different parameters involved in this process can be tuned in order to reach the targeted parameters of the 2D PC (its period *L* and its *ffair* ratio) and to transfer the obtained pattern in the different layers, while keeping low roughness of the etched sidewalls as low as possible.

4.3.1 Generation of PC patterns by laser holographic lithography

In order to generate such 1D or 2D PCs patterned solar cell stack, the processing sequence associated to LHL includes:

- sample cleaning and preparation
- hexamethyldisilizane (HMDS) adhesion promoter and resist spinning coating
- Post Apply Baking (PAB)
- UV exposure
- Post Exposure Baking (PEB)
- resist development
- descum etch step [10]

Sample cleaning and preparation is intended to improve the adhesion of the photoresist to a substrate. This is accomplished by one or more of following processes: substrate cleaning (using ultrasonic) to remove surface contamination, baking to remove water. Contamination can take the form of particles or a film and can be either organic or inorganic. Particles result in defects in the final resist pattern, whereas film contamination can cause poor adhesion and subsequent loss of linewidth control. One type of contaminant, adsorbed water, is easily removed by a high-temperature process call a dehydration bake, at 110°C, typically for 2 min.

A HMDS promoter is spun in order to obtain good adhesion with resist. A negative UV light sensitive resist is used thanks to its well-suited to the generation of a holes pattern in the resist. In the same time, high sensitivity and resolution may be achieved using such a Chemically Amplified Resist (CAR) resist [11]. Then the photoresist which is NEB-22 in this thesis is spun coating on HMDS.

A PAB process is performed, so as to dry the photoresist and to remove the solvents.

This technique consists in irradiating a photosensitive resist using an interference pattern. A simple way to create such patterns is to use the system

described in Fig. 4.4(**a**). The sample, covered with a UV sensitive resist, is placed on a sample holder, associated to a mirror placed at 90° of the sample. This system is illuminated by a laser beam; this generates fringes which irradiate the resist, with an inter-fringe distance L directly related to the angle θ through the relation $L = \lambda_{laser}/(2sin\theta)$. In order to generate a 2D pattern with a square symmetry at the surface of the sample, the irradiation needs to be repeated after tilting the sample by 90°. The resist is then exposed as schematically shown in Fig. 4.4(**b**). We implemented this generic process using a laser source at 266 nm, with a power around 5.4 mW, and a NEB 22 negative tone CAR. While the selected wavelength enables the patterning of structures with lattice parameters around 500 nm, using negative resist is well-suited to the generation of a holes pattern in the resist, as in the case of our design. In the same time, high sensitivity and resolution may be achieved using such a CAR resist [11].

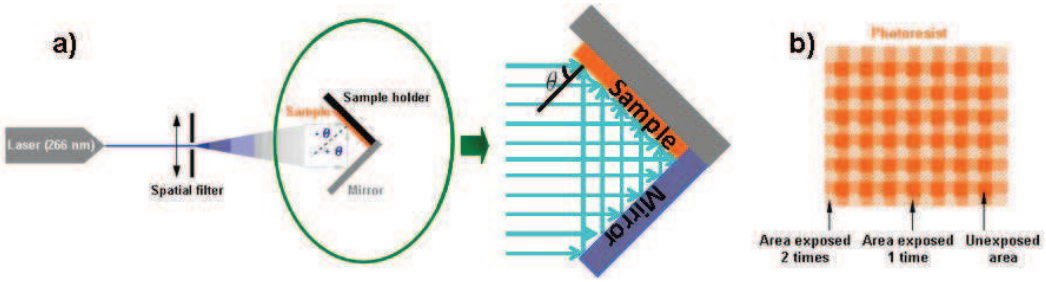

*Fig. 4.4. (**a**) Out of the spatial filter, the beams either impinge directly on the sample's surface or are reflected by the mirror, leading to interference fringes in the photoresist. After a 90 ° tilt of the sample, (**b**) the second exposure enables to create a square array of unexposed areas*

PEB is an essential step in CAR: it is used to catalyse linking reactions, to modify the solubility of the polymer matrix, and to homogenize the photo-acid concentration as generated during the exposure step.

The exposed photoresist is developed in developer solution by a suitable time. The final descum etch step is essential step to remove the remaining resist in patterned region which affects size and shapes of the final generated patterning.

While these steps are well established for standard silicon samples, using UV lithography at 248 nm [12], the process parameters should be adapted to perform LHL over our stacked layers deposited on glass. Indeed, heat transfer and standing wave effects [13] are expected to be different in the case of our structures and using a periodic interference pattern may induce specific constraints. Our methodology therefore consisted in scanning process temperatures and times, starting from parameters suited to classical UV lithography. The NEB resist is spun at 3000 rpm for 30s, followed by a PAB at a temperature of 110°C. Before these steps, it is extremely important that samples are cleaned twice by acetone, alcohol and DI water in ultrasonic batch and dried with N_2. After exposure and PEB (at 92°C), the development is performed in MF702 solution (supplied by Shipley Co), followed by a descum step in oxygen plasma. The following parameters, as PAB, exposure, PEB, development and descum etch times, are then investigated and discussed in the remainder of this section. Such experiments were performed on the stack described in section 4.5.

a. Influence of PAB time

The PAB step is aimed to remove the excess of solvent inside the photoresist. It was adjusted by varying its duration (120s, 150s and 180s), all other parameters being fixed (PAB temperature = 110 °C, Exposure time = 92 ^{2}C, PEB time = 120s, Development time = 1 solvent content is known to affect the PEB and development properties [14], different patterns could be generated by playing on the PAB time. However, as can be checked on Fig. 4.5, it seems this parameter does not have a major influence in our case, since all the patterns present the same PC parameters and comparable shapes of the holes. It means that any of these three PAB times will be suitable for our process.

From Fig. 4.5, we can compare diameters and shapes of resist pillars for 3 different PAB time. As they are almost the same, we can conclude that the time of PAB baking has no obvious influence for fabricating 2D patterns.

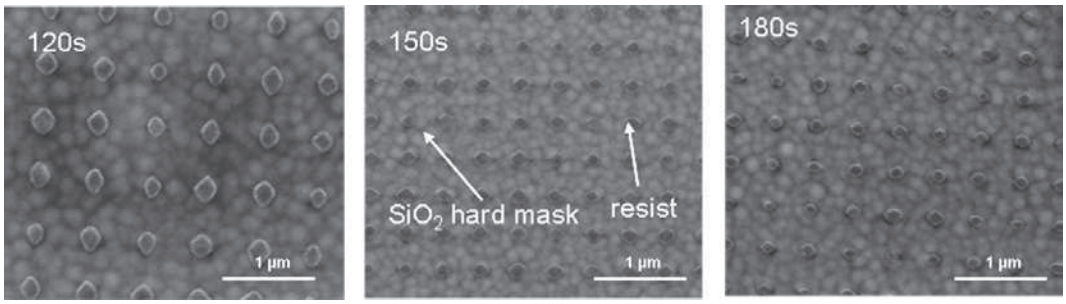

Fig. 4.5. SEM images of the patterned photoresist for different PAB times

b. Influence of exposure time

A first set of experiments was performed with a double UV exposure performed with an exposure time ranging between 50 and 130s. The PAB and PEB parameters were fixed at 110°C for 120s and 92°C for 240s respectively, with 10s development time and 8s O_2 plasma.

As shown in the SEM images from Fig. 4.6, the holes appear circular, with a strong impact of the exposure time on the diameter. As expected in the case of a negative resist, the diameter is decreased while the exposure time is increased. This dependence can be used to control the *ffair* ratio of the patterns, which stands from 0.35 to 0.65 in the whole exposure time range, and for a lattice parameter between 520 and 620 nm. Therefore, the targeted *ffair* ratios (50 % to 60 %), as calculated in section 4.2, stand well within the achievable range. However, parasitic effects such as the presence of an inner resist ring for an exposure time of 90s, or a secondary resist pattern for low exposure times clearly appear. The former may reduce the *ffair* ratio. The latter, which is due to the classical optical standing wave effects [13], does not impact the final shape of the holes. However, it should be eliminated before pattern transfer into the underlying layers since it could change the holes diameter; this is the role of the descum step, which will be discussed at the end of this section.

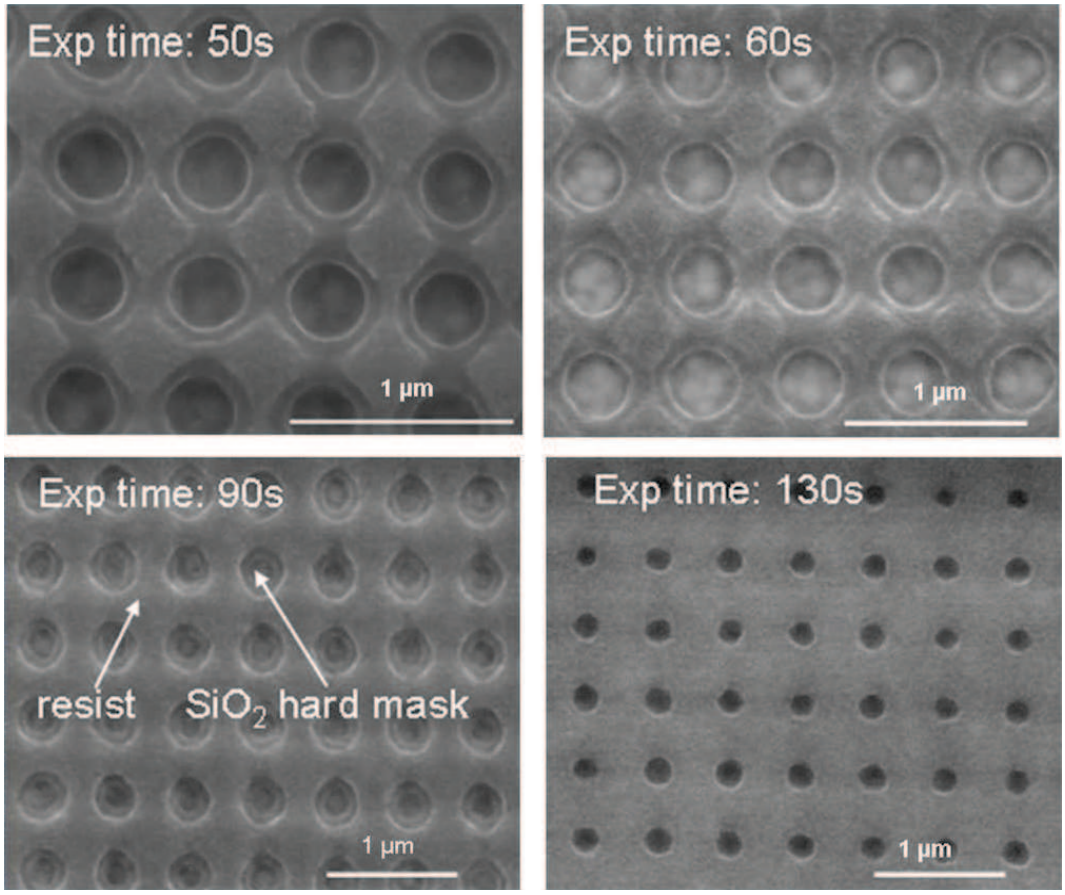

Fig. 4.6. Influence of the exposure time on the diameter of the holes

c. Influence of PEB time

PEB is an essential step in CAR resists. It is used to catalyse linking reactions, to modify the solubility of the polymer matrix, and to homogenize the photo-acid concentration generated during the exposure step. In this sense, it is expected to have a strong impact on the pattern shape and on the reduction of standing wave effects. In a second set of experiments, PEB time was tuned in a 120-240s range, with a 120s PAB, a 50s exposure, a 10s development and a 8s descum. Corresponding SEM images are shown in Fig. 4.7.

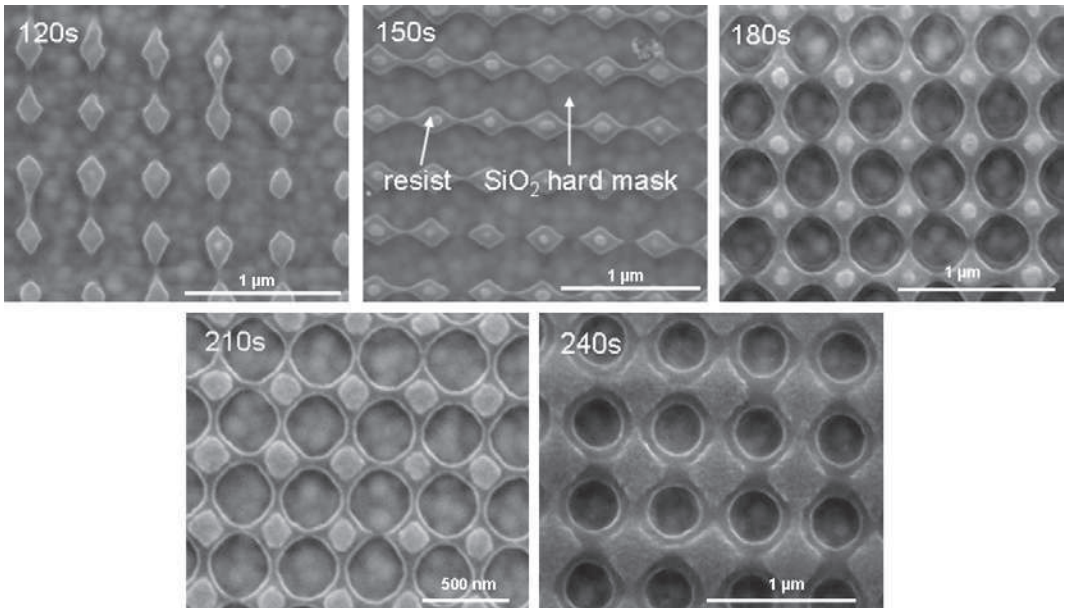

Fig. 4.7. SEM images of patterned photoresist for PEB times from 120s to 240s (with a 30s step) at 92°C

Although a 120s PEB time is generally sufficient in the case of silicon samples, it is necessary to perform a longer baking in the case of our samples. This may be accounted for by the lower thermal conductivity of the glass wafers. PEB time, which should be over 180s, also appears as a second way to control the size of the holes for a given lattice parameter.

d. Influence of development time

After development, non-sensitive areas of NEB-22 layer are dissolved in MF702 developer, potential graphics of patterns are apparent in the photoresist layer, but the development time is a very important parameter for this step, a great deal of research efforts are needed to discover the impact of development time, as usual, we fixed other parameters as PAB is 110 °C for 120s; exposu
PEB is 92 °C for 150s; O_2 plasma 30s; increased to 8s; and changed development time changed from 8s to 10s, as shown on Fig. 4.8.

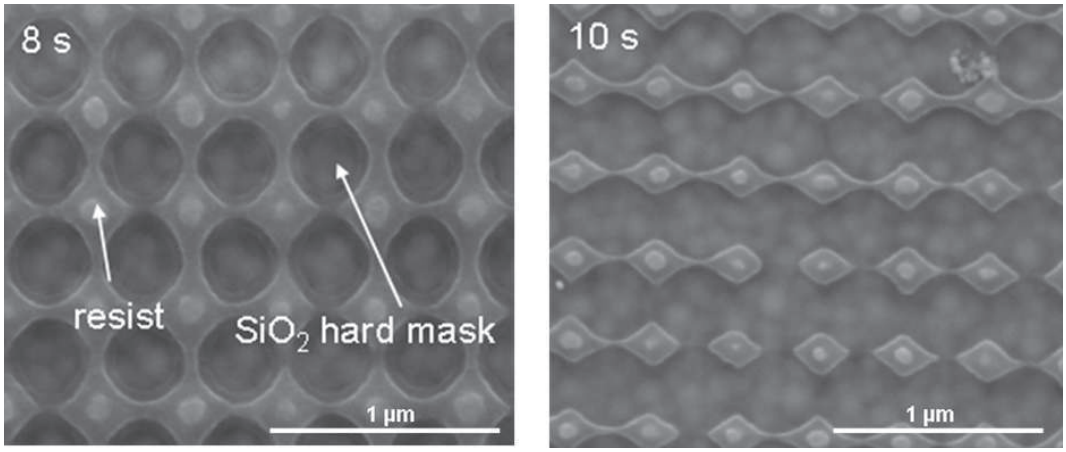

Fig. 4.8. SEM images of patterning photoresist for development time of 8s and 10s

The two studies we have performed have demonstrated the influence of development time. Comparing the shapes of 8s' and 10s' development time, obviously, only the 8s' can generate a 2D patterns when PEB time is 150s, although the remaining photoresist of inner holes can't be removed by developer solution directly.

e. Role of final descum etch

As mentioned above, photoresist may remain within the patterned holes. As it affects size and shape of the final 2D PC structure, after ITO and a-Si:H etching, this resist material should be removed; this is the role of the final descum step. It consists of a reactive ion etching step, with a 20sccm O_2 flow, at 100 W, under a pressure of 100 mTorr. The influence of this 8s descum step is illustrated in Fig. 4.9 in the case of a 120s PAB, a 50s exposure time, a 210s PEB, and a 10s development time. As a result of this final step, the inner resist ring is removed, and the pattern roughness tends to be decreased. Furthermore, the *ffair* ratio is increased from 0.89 to 0.93 after the descum step. This geometrical change should be anticipated when the PEB and exposure time are selected, in order to reach the targeted D and L values.

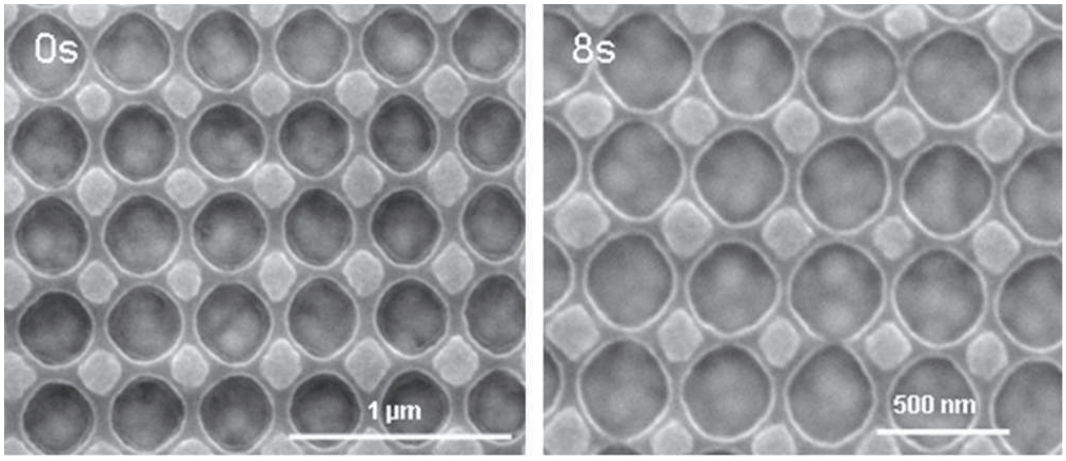

Fig. 4.9. 2D patterning without and with the 8s O_2 plasma

As a conclusion from this investigation, process parameters can be adjusted in order to achieve the targeted 2D pattern. While the PAB time may be fixed at 120s, the exposure and PEB times may be jointly adjusted in order to reach the targeted value of the *ffair* ratio. An appropriate set of parameters consists of a 60s exposure, with a PEB time of 180s. Finally, to take full profit of the LHL patternings, a 8s final descum step should be performed.

4.3.2 Transfer of the patterns by reactive ion etching

The photonic crystal pattern defined by LHL is first transferred into a 100 nm thick SiO_2 hard mask, and then into the underlying ITO and a-Si:H layers, using RIE processes. Transfer into the SiO_2 hard mask is achieved using CHF_3 plasma (with a 16sccm flow, at 15mT, with a power of 100W, for 900s). After resist removal by O_2 plasma, the patterns are transferred to the ITO layer, using a CH_4:H_2 plasma, with flows of respectively 10sccm and 30sccm, at a 200W power, for 130s. This step is performed at low pressure (30mTorr) in order to achieve high sidewall verticality. Finally, the a-Si:H layer was etched with a SF_6:Ar plasma (5sccm for each gas, at 50W during 180s, with reduced pressure of 15mTorr). Fig. 4.10 shows that holes with a reasonable regularity and roughness could be transferred; the achieved period and *ffair* ratio are respectively 585 nm,

in the targeted range, and 47%, just a little bit below the range corresponding to the optimum configuration (50 %-60 %).

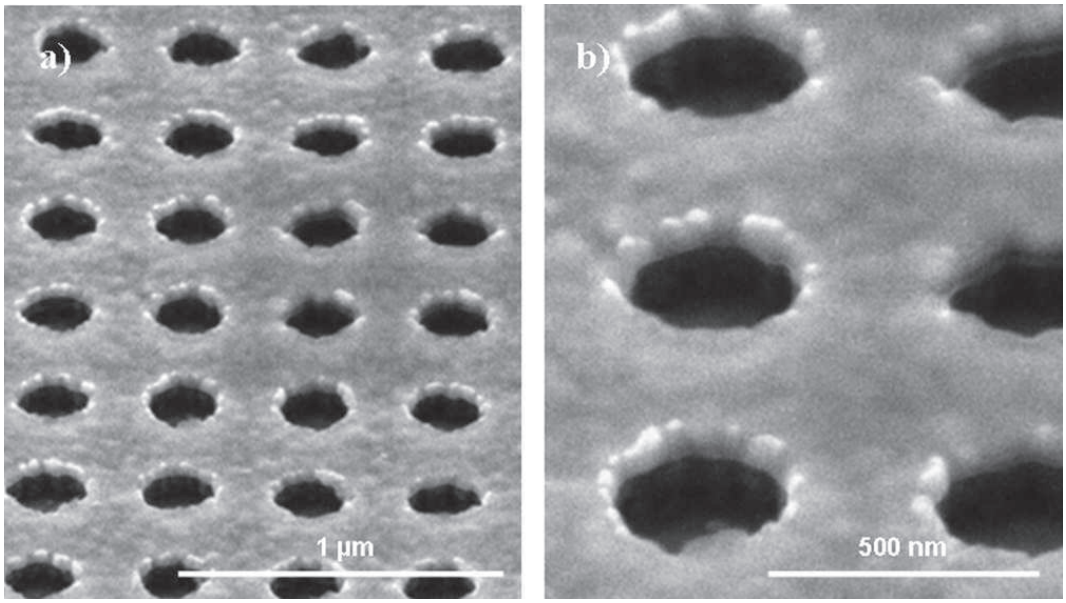

*Fig. 4.10. SEM profile images of the etched SiO_2 hard mask, ITO and a-Si:H layers. (**a**) General view of the surface (**b**) Close-up of the holes*

4.4 Optical characterization of the patterned solar cell stack

In order to determine the optical properties of the patterned solar cell stake presented in the previous section, absorption measurements were performed using an integrated sphere. In these experiments, the sample is illuminated by unpolarized light, so as to perform reflectance (R) and transmittance (T) measurements, with a ~1 mm² spatial resolution and a 8° angle of incidence. The absorption $A(\lambda) = 1- R(\lambda) -T(\lambda)$ is then simply derived. The absorption within the whole patterned stack was measured between 300 nm and 720 nm with a 5 nm step and an experimental uncertainty of about 5 %. The absorption spectrum of the unpatterned stack was also measured as a reference. The corresponding

spectra are reported in Fig. 4.11(**a**). Absorption spectra simulated by RCWA are displayed in Fig. 11(**b**) for comparison. Same stacks as the ones used for the fabrication of the cells have been considered for that purpose, but the top SiO_2 hard mask was not taken into account for the simulations. Due to an uncertain determination of geometrical parameters, in particular the ITO layer thickness, but also the inhomogeneity of the *ffair* ratio, calculated and measured absorption spectra exhibit different features. However, strong similarities are noticeable and the same general trends can be deduced.

All spectra exhibit high absorption for $\lambda < 550$ nm, though slightly more important in the case of the patterned stack. Indeed, the high values of the extinction coefficient of a-Si:H ($k_{a\text{-}Si:H}$) are sufficient to ensure the absorption of the incoming light in one pass within the active layer. Besides, patterning the cell structure decreases the mean refractive index in the front of the cell, leading to an antireflective effect; absorption is then higher in the case of the patterned cell. The situation differs above 550 nm; a sharp decrease of the absorption is observed for the unpatterned cell due to the low values of $k_{a\text{-}Si:H}$ in this spectral range, whereas the 2D PC patterning of the active layer leads to additional absorption peaks, and finally to a higher absorption than in the case of the reference. These absorption peaks are attributed to resonant Bloch modes of the absorbing PC membrane. Thanks to a good "impedance matching" with regards to the incident light, maximising the absorption is possible [3]. Moreover, due to the multimode character of this PC membrane structure and therefore the number of resonances, the absorption integrated in the whole range between 550 and 720 nm is significantly increased in the case of the "photonized" solar cells.

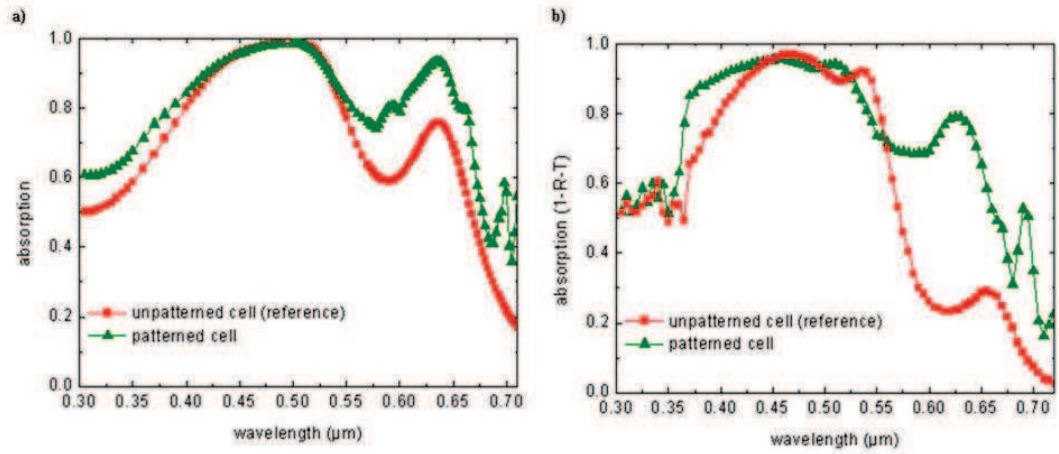

*Fig. 4.11. Comparison between the calculation **(a)** and the measurement **(b)** absorption spectra of the patterned and the unpatterned stacks (angle of incidence fixed at 8°)*

In addition, the polarization independence of the fabricated patterned cell was also investigated by shifting the sample by 90°, while keeping all the other parameters fixed. As can be seen on Fig. 4.10, the spectra corresponding to the two configurations (non shifted or shifted by 90°, with an angle of incidence of 8°) nearly superimpose throughout the considered wavelength range. This indicates that the shape of the PC membrane holes is almost isotropic.

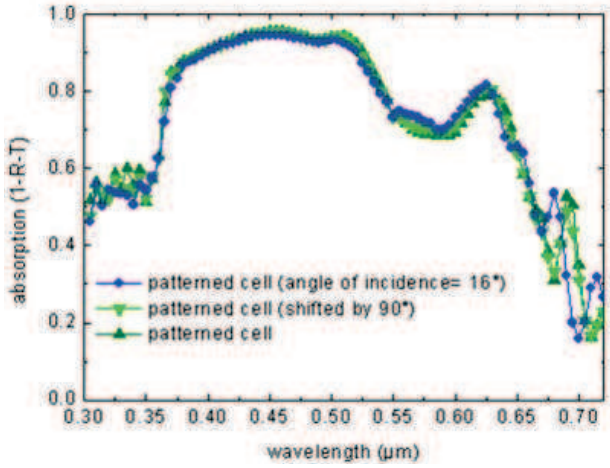

Fig. 4.12. Influence of the polarization and of the angle of incidence on the measured absorption spectrum of the patterned cell

Lastly, the influence of the angle of incidence was tested by doubling its value, from 8° to 16°. If increasing the angle of incidence engenders a blue-shift of certain absorption peaks, for instance around 690 nm on Fig. 4.12, it globally leaves the integrated absorption of the structure unchanged. This can be accounted for by the multimode nature of the PC structure, since a weak modification of the resonant mode properties will not be visible in the wide spectral range we consider [9].

4.5 Outlook

4.5.1 Optical design for 2D PC solar cell stacks on ultra thin film a-Si:H to increase optical harvesting

In PC or diffraction grating patterned stacks, the surface recombination is extremely important to obtain a higher short circuit current density J_{sc}. The ratio Surface/Volume (S/V) between the area occupied by the hole sidewalls and the Silicon volume is an indication of the potential impact of the surface recombination, with regards to bulk recombination. More generally, using different PC symmetries, one could obtain different values of conversion efficiencies for similar integrated absorptions. Therefore, considering the electrical [15] and optical design [9, 16-17] of the ultra thin a-Si:H solar cells, possible alternative symmetries include triangular, honeycomb, or "square honeycomb" structures patterned in a-Si:H thin film solar cells (shown on Fig. 4.13(**a**)-(**d**)).

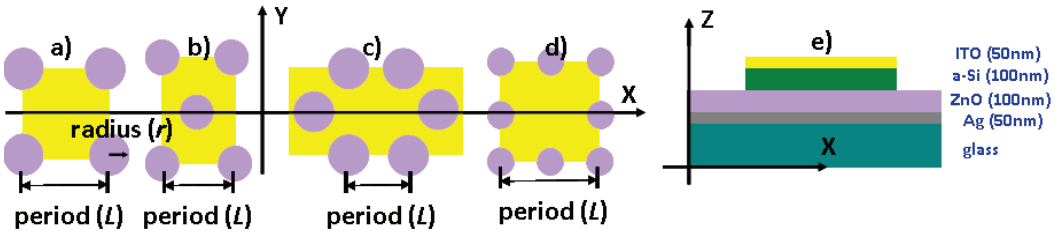

*Fig. 4.13. Topography of the (**a**) square, (**b**) triangular, (**c**) honeycomb and (**d**) square honeycomb "photonized" a-Si:H thin film solar cells, as well as (**e**) a profile view of such device*

The lattice period (L) and radius (r) as defined in Fig. 4.13 are scanned in a large range to optimize the integrated absorption in the a-Si:H layer for each of these structures. The AM1.5G solar irradiance was taken into account over the same 300-720 nm spectral range, as in the case of the square lattice introduced in the beginning of this chapter. This theoretical computation has been conducted by using finite difference time domain (FDTD) [18], and more specifically its package Lumerical [19]. Periodic boundary conditions are considered along the X and Y axis, while Perfect Match Layer (PML) are used in the Z direction. Additionally, the radius range is limited in order to avoid two holes connecting each other, and scanning step is 20 nm. L is scanned from 300 nm to 700 nm per 20 nm step. Moreover, we concentrate on TM polarization (it would be the same as the case in TE in a 2D grating under normal incidence). The optimized lattice parameters, surface/volume (S/V) and integrated absorption as well as the relative absorption in the whole stack and the a-Si:H layer are compared in Table.1. Corresponding spectra are shown in Fig. 4.14.

Table.1 Optimized integrated absorption in the active a-Si:H layer and whole stack of the different patterned stacks, as well as S/V ratio. The reference is a planar unpatterned stack.

Stack (optimized lattice parameters)	S/V	Integrated absorption	
		whole stack	a-Si :H
Structure **a**): square (L = 380 nm , r = 119 nm)	0.0075	0.82	0.66
Structure **b**): triangle (L = 350 nm , r = 100 nm)	0.012	0.73	0.60
Structure **c**). honeycomb (L = 320 nm, r = 120 nm)	0.0086	0.82	0.65
Structure **d**): square honeycomb (L = 540 nm, r = 130 nm)	0.018	0.88	0.64
reference	0	0.64	0.52

Comparing the integrated absorption in the a-Si:H layer, it clearly appears that the PC symmetry has a low impact, except in the case of the triangular structure, which lead to the lowest value. The *S/V* in the square and honeycomb stacks are similar (~ 0.008) but lower than triangle and "square honeycomb" symmetries

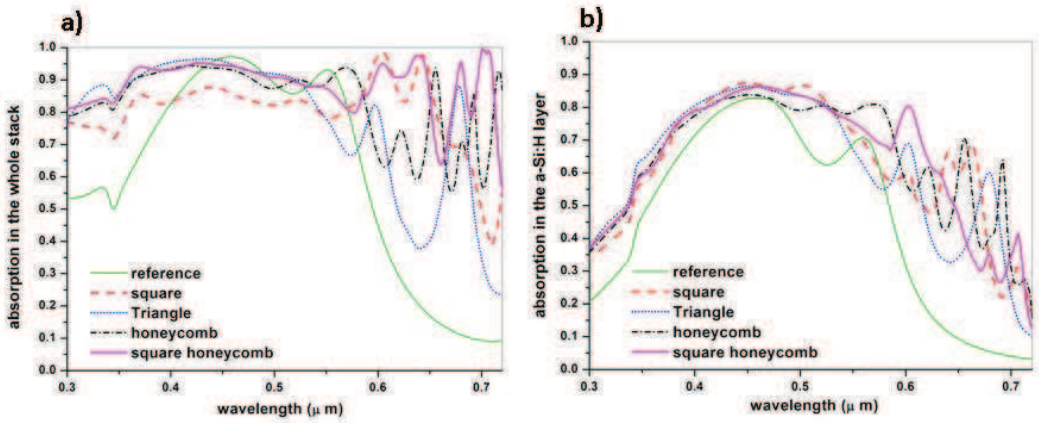

*Fig. 4.14. The absorption spectra in (**a**) the whole stack with different patterning and in (**b**) the a-Si:H active layer on the TM polarization*

From the above computations, we conclude that the different geometric patterning could lead to similar absorption in the a-Si:H layer. By considering integrated absorption in active layer and *S/V* ratio, triangle, honeycomb and

honeycomb structure don't show obvious advantages compared to the square structure. To definitively conclude on the impact of the PC symmetry on the efficiency of the device, additional simulation should be performed including electrical and optical modelling.

4.5.2 Technological route to generate triangular lattice by laser holographic lithography

In addition to the square lattice 2D PC and binary 1D PC, the triangular lattice could be generated with the low cost LHL technique [20]. Theoretically, the sample has to be rotated by 60° after the first exposure, then exposed with similar exposure time and power intensity. After development, the triangular lattice could be observed, as shown on Fig. 4.15.

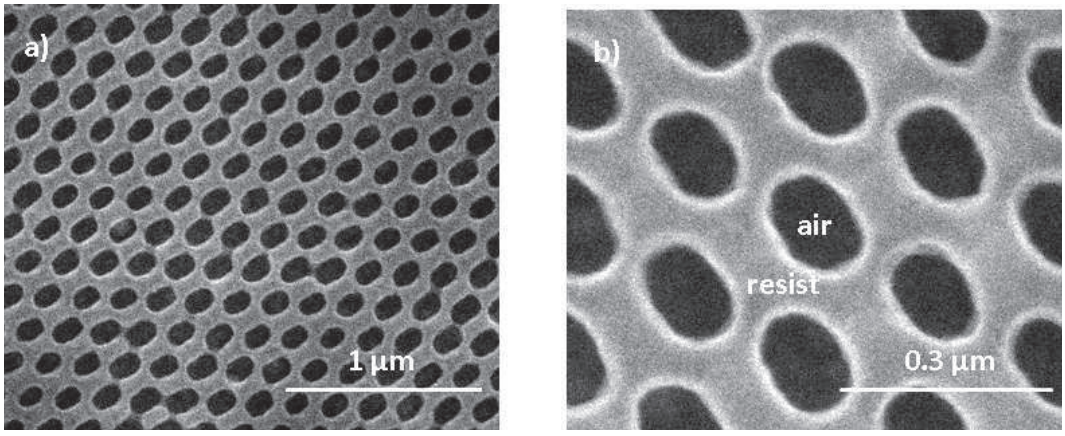

*Fig. 4.15. SEM images of the patterned resist on a cell stack, (**a**) General view of the surface and (**b**) close-up of the holes*

Period and radius could be controlled to reach the theoretically established design by modifying the mirror angle, exposure time and development time as introduced in section 4.3. But 2D holes are not exactly circular. However, when the lattice parameters float in a relative large range, in which optical or electrical properties of structure could be robust, the influence of the shapes will not be so important.

Recently, almost perfectly circular holes could also be generated by LHL by triple exposures. It is fulfilled by rotating the sample to +60° and -60° during the second and the third exposures. Finally, such kind of circular holes in triangular lattices have been generated, as displayed in Fig. 4.16(**a**). But it is crucial to control the rotation angle of sample as exactly as +60° and -60° for the second and the third exposure. If there is a one or two degrees difference, the final patterned shapes could be far away from the design, as shown in Fig. 4.16(**b**), which is schematized in Fig. 4.16(**c**) with different rotation angle for the second and the third exposure (-62°, 0, 60°).

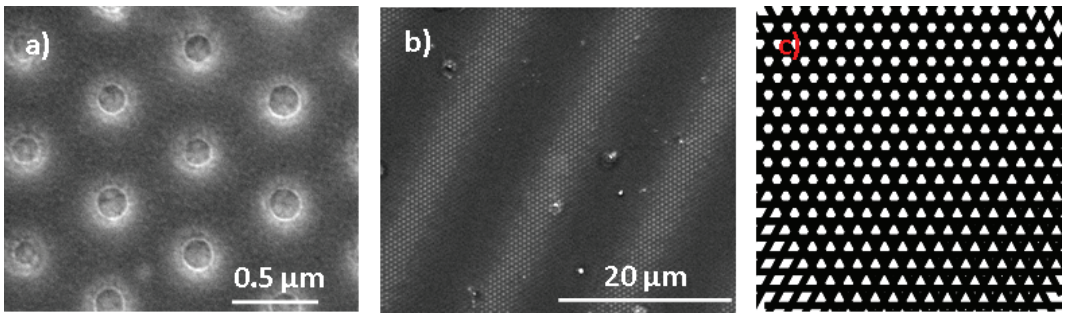

*Fig. 4.16. SEM images of the triple exposure on the resist for triangular lattice with (**a**) correct parameters (**b**) wrong rotating angle (-62°, 0, 60°) , and (**c**) schematic view corresponding to (**b**).*

Conclusion

Thin-film photovoltaic cells structures integrating a 2D PC membrane have been designed and fabricated and optically characterized. We specifically focused on the development of a process based on LHL and RIE, enabling the generation of 2D PC membrane on a 2*2 cm^2 surface, with a high throughput.

- By an appropriate tuning of exposure and PEB times of lithographic process, the desired configurations derived from optical simulations could be fabricated.
- In order to limit roughness of sidewalls and to achieve a better control of the geometrical parameters, an additional descum etch step was necessary and optimized.
- Absorption spectra were determined experimentally by optical measurements using an integrating sphere. Measurements were performed on the patterned and unpatterned reference cell structures, and compared to spectra calculated by the RCWA method. Measured and calculated absorption spectra exhibit a very similar behaviour. The absorption, integrated over the 300-720 nm range, is increased by 28 % in the case of a solar cell stack patterned as a PC membrane. This increase is mainly attributed to the positive role of Bloch mode resonances in the PC membrane above 550 nm.
- These "photonized" cells are independent to the polarization of the light and present a good tolerance towards the angle of incidence.

References and links

[1] R. E. I. Schropp, and M. Zeman, *Amorphous and microcrystalline silicon solar cells: modeling, materials, and device technology*, (Kluwer Academic Publishers, Norwell, Mass (1998).

[2] J. Dresner, D. J. Szostak, and B. Goldstein, "Diffusion length of holes in *a*-Si:H by the surface photovoltage method," Appl. Phys. Lett. **38**, 998 (1981)

[3] Y. Park, E. Drouard, O. El. Daif, X. Letartre, P. Viktorovitch, A. Fave, M. Lemiti, and C. Seassal, "Absorption enhancement using photonic crystals for silicon thin film solar cells," Opt. Express **17**, 14312-14321 (2009).

[4] O. El Daif, E. Drouard, G. Gomard, A. Fave, A. Kaminski, M. Lemiti, Y. Park, X. Letartre, P. Viktorovitch, S. Ahn, H. Jeon, and C. Seassal, "Photonic Crystal Enhanced Absorption of Amorphous Silicon for Solar Cells," Proc.24th European Photovoltaic Solar Energy Conference, 548-552 (2009).

[5] L. Ferrier, O. El. Daif, X. Letartre, P. Rojo Romeo, C. Seassal, R. Mazurczyk, and P. Viktorovitch, "Surfaceemitting microlaser based on 2D photonic crystal rod lattices," Opt. Express **17**, 9780-9788 (2009).

[6] G. Gomard, O. El. Daif, E. Drouard, X. Meng, A. Kaminski, A. Fave, M. Lemiti, E. Garcia-Caurel, P. Roca i Cabarrocas, and C. Seassal, "Design and fabrication of photonic crystal thin film photovoltaic cells," Proc. SPIE **7725**, 77250M (2010).

[7] Developped by Ghent University, see http://camfr.sourceforge.net/.

[8] M. G. Moharam and T. K. Gaylord, Rigorous coupled-wave analysis of planar-grating diffraction, J. Opt. Soc. Am. **71**, 811–818 (1981).

[9] G. Gomard, E. Drouard, X. Letartre, X. Meng, A. Kaminski, A. Fave, M. Lemiti, E. Garcia-Caurel , C. Seassal, "Two-dimensional photonic crystal for absorption enhancement in hydrogenated amorphous silicon thin film solar cells," J. Appl. Phys. **108**, (2010) 123102 (2010).

[10] Chris A. Mack, *Field Guide to Optical Lithography*, SPIE Press Book, 2006.

[11] H. Ito, C.G. Willson, "Chemical amplification in the design of dry developing resist materials," Polym. Eng. Sci. **23**, 1012-1018 (1983).

[12] S. Pauliac, S. Landis, J. Foucher, J. Thiault and O. Faynot, "Hybrid lithography process for nano-scale devices," Microelectronic Engineering **83**, 1761–1766 (2006).

[13] Andreas Grassmann et al., "Contrast Transfer Function Measurements of Deep Ultraviolet Steppers," J. Vac. Sci. Technol. **10**(6), 3008-3011 (1992)

[14] Chris A. Mack, *Field Guide to Optical Lithography*, SPIE Press Book, 2006.

[15] G. Gomard, X. Meng, E. Drouard, K. El Hajjam, E. Gerelli, R. Peretti, A. Fave, R. Orobtchouk, M. Lemiti and C. Seassal, "Light harvesting by planar photonic crystals in solar cells: the case of amorphous silicon," J. Optics. **14**, 024011 (2012).

[16] X. Meng, G. Gomard, O. El Daif, E. Drouard, R. Orobtchouk, A. Kaminski, A. Fave, M. Lemiti, A. Abramov, P. R. i Cabarrocas and C. Seassal, "Absorbing photonic crystals for silicon thin-film solar cells: Design, fabrication and experimental investigation," Sol. En. Mat. Sol. Cells **95**, 32–38 (2011).

[17] X. Meng, V Depauw, G. Gomard, O. El Daif, C. Trompoukis, E. Drouard, A. Fave, F. Dross, I. Gordon, and C. Seassal, "Design and fabrication of photonic crystals in epitaxy-free silicon for ultrathin solar cells," Proceedings of SPIE, **8312**, 831207 (2011)

[18] A. Taflove and S. Hagness, *Computational Electrodynamics: The Finite-Difference Time-Domain Method* (Artech, 2005).

[19] http://www.lumerical.com/

[20] B. J. Thibeault, Y. J. Hung, and S. L. Lee, "Realization of silicon nanopillar arrays with controllable sidewall profiles by holography lithography and a novel single-step deep reactive ion etching bib," In Mater. Res. Soc. Symp. Proc., 2010. Mater. Res. Soc. Symp. Proc., 1402–1415. Mater. Res. Soc. Symp. Proc. (2010).

Chapter 5

Absorbing photonic crystals for crystalline silicon ultra thin-film solar cells: design, fabrication and experimental investigation

5.1 Introduction

In this chapter, we will consider solar cell devices based on very thin mono crystalline silicon (c-Si) layers. With such absorbing layers, bulk recombination of carriers is expected to be strongly decreased with regards to polycrystalline and amorphous silicon layers. Indeed, few technologies are available to obtain thin mono crystalline Si thin film on glass. Direct deposition by CVD leads to polycrystalline Si materials with low grain size and therefore a low efficiency potential. Therefore, several transfer techniques were considered usually based on a porous sacrificial layer [1-2]. Among them, the so called Epifree technology [3], developed by IMEC PV group, is of particular interest: which allows fabricating crystalline-Si layers with a thickness down to 1µm. Such layers are transferred onto glass by anodic bonding on an Al layer, as briefly introduced in Chapter.3.

As in the case of ultra-thin layer a-Si solar cells, PV devices based on a 1µm thick layer need an efficient light trapping structure to reach a high efficiencies. In particular, it should be highlighted that the photonic structure cannot be obtained just by a conformal deposition of the absorbing layer (like in the case of a-Si:H) on a pre-patterned wafer. Indeed, c-Si layer are inherently flat and photonic structures like periodic grating or photonic crystals (PCs) should be directly etched on the c-Si layer [4-5].

In this chapter, we report on the design and the fabrication of Epifree c-Si thin-film solar cell stacks prepared at IMEC on which we integrate 1D and square lattice 2D PC patterns on the front – junction - side. The global design of these cells has been optimized optically by finite difference time domain (FDTD) [6-7] simulations. The optimized devices are designed by scanning the topographical parameters, and calculating the integrated absorption for each case. After presenting the general fabrication process of the patterned cells, we show one of the possible routes to integrate 1D and 2D photonic structures in the active layer, by associating laser holographic lithography (LHL) with reactive ion etching (RIE) and inductively coupled plasma (ICP) etching. The optical properties of the

fabricated devices are then discussed and compared to simulation results. In conclusion, we will briefly mention solar cell results which were obtained recently.

5.2 Absorption enhancement mechanisms in a 1D and 2D PC patterned c-Si layer

Before considering a complete solar cell, we first introduce the effect of a 1D or 2D PC patterning in a 1µm thick c-Si layer. We will consider its lattice parameter, or period (*L*), its surfacic air filling factor (*ffair = (area of air)/(area of material) =d/L* in the case of a 1D PC, as shown on Fig. 5.2(**a**) and the etching depth of Si (*h*). Indeed, whereas in the case of a-Si absorbers, we will consider partially etched c-Si layers. In this section, we will discuss on the impact of these topographical parameters on the absorption efficiency in the c-Si layer.

The absorption spectra are computed by FDTD, and the absorption efficiency is calculated considering an AM1.5G solar spectrum intensity distribution, over the 300-1100nm spectral range, at normal incidence. These boundaries roughly and respectively correspond to the lowest wavelength of the solar spectrum and the c-Si gap. For 1D PCs, we consider the average between a TE and a TM polarized incident beam. The simulation methodology was extensively introduced in section 3.1.

5.2.1 Optimization of the topographical parameters in the case of a 1D PC

We first simulate the absorption efficiency for a wide range of values of *L*, *ffair* and *h*.

Figure 5.1(**a**) displays the integrated absorption, as calculated for a *ffair* arbitrarily fixed at 50%, and for period in the [100, 1000] nm range, and for etching depths in the [0, 500] nm range. Figure 5.1(**b**) is a similar contour plot, calculated for a period set at 500 nm, and for a variable value of *ffair* and *h*, respectively in the [20, 80]% range and in the [0, 500] nm range. These ranges of parameters have been selected because they correspond to technologically feasible structures. Taken out a group of fixed period and *ffair* at 500 nm and 50% respectively, then compared to the integrated absorption on TE and TM polarizations, as shown on Fig. 5.2(**b**)

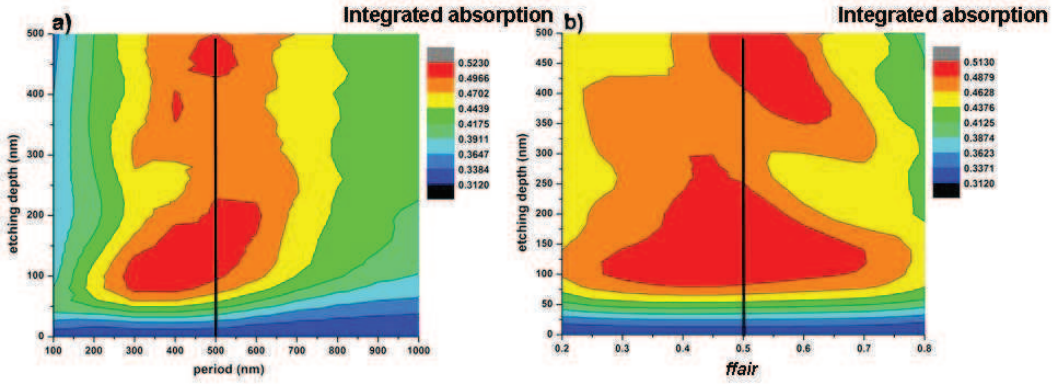

*Fig. 5.1. the integrated absorption comparison (**a**) by scanning the period and etching depth at fixed ffair 50% and (**b**) by scanning the ffair and etching depth at given period 500 nm on the 1D patterned 1 µm thick c-Si layer*

We will consider these two contour plots, together with Fig. 5.2(**b**), which displays the absorption as a function of *h*, for *L* = 500 nm and *ffair* = 50%. We first deduce that the integrated absorption is optimized for an etching depth either around 140nm, or around 460 nm. Considering that it will always be easier to pattern shallower air holes or slits, we will target a value of *h* = 140 nm. Moreover, for a wide range of values of *L* and *ffair*, the absorption in the c-Si layer is improved up to 51%, which corresponds to a 65% relative increase compared to an unpatterned 1µm thick layer of c-Si. A second important conclusion is that this optimized absorption is achieved for a wide range of *L* and *ffair*. Indeed, the integrated absorption is maximized for an etching depth deeper than at least 100 nm, for *ffair* in the 35%-65% range, and for a period in the 300-650 nm range.

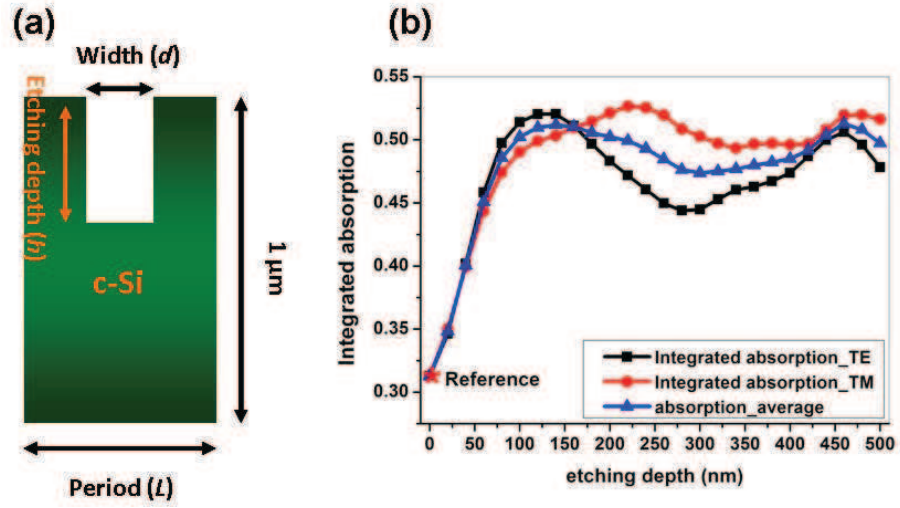

*Fig. 5.2. **(a)** the s*chematic view of the front 1D patterned single c-Si layer, ***(b)*** *the integrated absorptions based on TE and TM polarizations compare to the average integrated absorption. The lattice parameters are (L = 500 nm and ffair = 50%) by scanning h from 0 to 500 nm range on a 1 µm thick c-Si layer*

5.2.2 Absorption mechanisms in a 1D and 2D PC patterned c-Si layer

Figure 5.3 shows the absorption spectra for 1µm thick c-Si layers patterned as 1D or 2D PCs, under illumination at normal incidence. In the case of 1D PC layers, the absorption results from an average of TE and TM polarizations. These spectra were simulated considering L = 0.61 µm, *ffair* = 35% and h = 0.14 µm. These values, which stand within the range indicated in section 5.2.1, will be justified in the next sections. They were chosen considering the necessity to integrate the c-Si layer with the collection electrodes.

For the 1D and 2D PC patterned layers, the integrated absorption between 300 and 1100 nm is respectively 48% and 57%, . These values are much higher than the 31% value obtained for the planar c-Si layer. Moreover, under normal incidence, we observe that the absorption efficiency of a 2D PC layer does not depend on the polarization of the incident light. In the unpatterned c-Si layer, from about 450 nm to 1100 nm, the clearly visible absorption resonances

correspond to Fabry-Perot modes due to the large index contrast between air and the c-Si layer. These resonances can lead to absorption maxima, but the spectral density of modes is limited by the low thickness of the layer, leading to a low integrated absorption over the whole spectral range. Moreover, the large index contrast leading to a high reflection is also responsible for the low absorption (~50%) below 450 nm. On the contrary, the absorption is higher at low wavelength for both 1D and 2D patterned layers. At high wavelength, additional absorption peaks appear, which are attributed to Bloch modes resonances of the PC structures. Thus, the roles of the PC are twofold:

- To reduce reflection for all solar spectra 300 nm -1100 nm range
- To increase the spectral density of resonant modes at large wavelengths, leading to an increased absorption

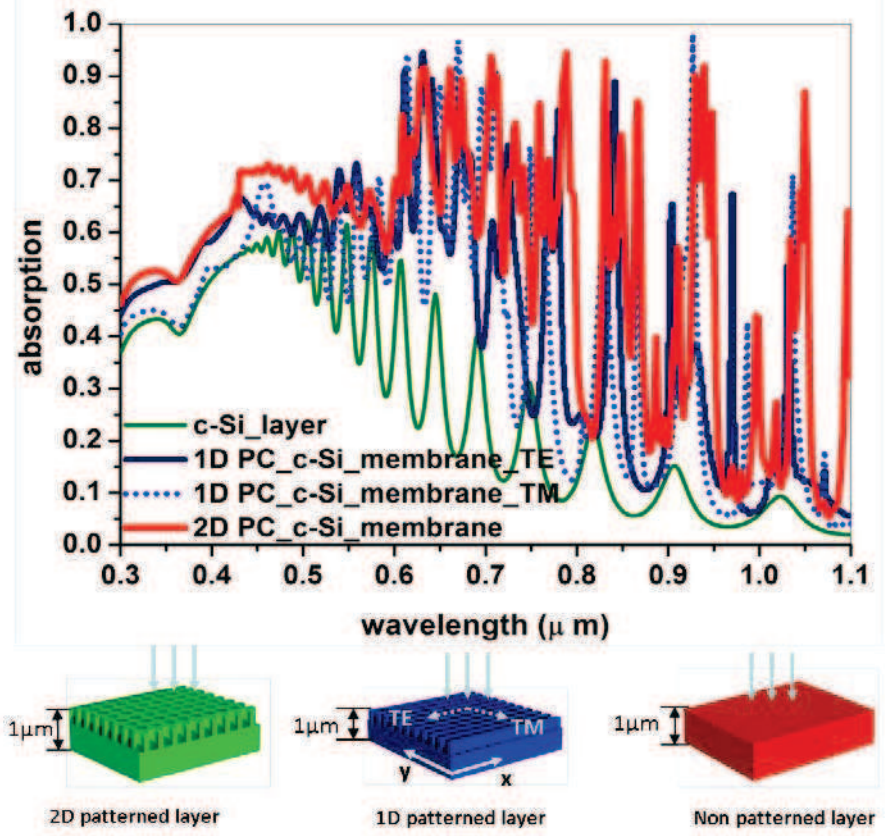

Fig. 5.3. Simulated absorption spectra of the patterned 2D and 1D PC patterned c-Si layer with the same period, ffair and etching depth (L = 0.61 μm, ffair = 35% and h = 0.14 μm) compared to the one of a planar c-Si layer of the same thickness (1 μm).

5.3 Optical design of 1D PC patterned c-Si ultra thin film solar cells

5.3.1 Structure description

The targeted PV solar cell is based on a thin layer stack composed, from the back to the front, of a glass substrate, a 100 nm metallic back-contact and reflector, a 20 nm highly-boron-doped c-Si layer acting as back-surface field, a 1 μm thick epitaxy free c-Si active layer overlaid by a 10 nm i/n^+ doped a-Si:H layer and finally a transparent and conductive oxide (TCO) layer.

The back metallic electrode could be made of aluminium (Al), silver (Ag), gold (Au) and platinum (Pt) layers. Regarding optical and electric properties, Ag is the most appropriate candidate. However, we will also consider Al layers. Indeed, although this material will lead to a higher parasitic absorption, its cost is lower cost, and it is necessary to achieve anodic bonding between Si and glass [3].

The front TCO layer acts as an anti-reflection coating (ARC) [8-9] with adequate thickness so that interference effects decrease reflectivity at the top surface [10-11], in particular in the case of an unpatterned device. It should have a sheet resistance low enough to enable simultaneously low lateral carriers transport losses over hundreds of micrometers to lateral metallic contacts and a low optical absorption. Among the most commonly used TCO materials are an indium tin oxide (ITO), a zinc oxide (ZnO), tin oxide (SnO_2), indium oxide (In_2O_3), or ZnO:Al and so on [12-13]. Considering the previous conditions, ITO or ZnO are the best candidates. Their thickness of the TCO should be adjusted depending of the selected material, and will result from a compromise between low absorption and high conductivity.

On the top of these c-Si solar cell stacks, we integrate a PC structure, e.g. by performing a partial etching of the three layers positioned on the top: c-Si, a-Si:H, and the TCO. The targeted configuration is schematically shown on Fig. 5.4(**a**)-

(**b**) for 1D and 2D periodic structures. In the next section, we investigate the role of each key element of this device.

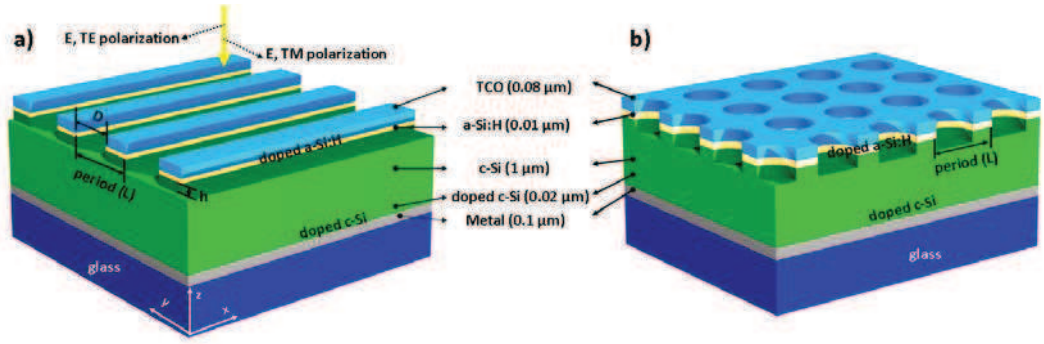

*Fig. 5.4. Schematic view of the investigated (**a**) 1D and (**b**) 2D patterned stack. Photogenerated carriers originating from the c-Si active layer are collected through the TCO and the metal layers.*

5.3.2 Design of the back metallic contact

In this subsection, we investigate the role of the nature of the back metallic contact, which could be constituted of Al, Ag, or by a combination of these two materials.

Indeed, as mentioned above, Al [14] and Ag [15] could be used as back reflector and electrode because of their lower cost, and their well adapted electric and optical properties.

In order to determine the optimum thickness of Ag or Al in the future designs, we first exhibit a simple simulation of the integrated absorption in such a metallic layer as a function of its thickness. Both Al (Fig. 5.5(**a**)) and Ag (Fig. 5.5(**b**)) layers deposited on glass are studied, with thicknesses in the 10-1000nm range.

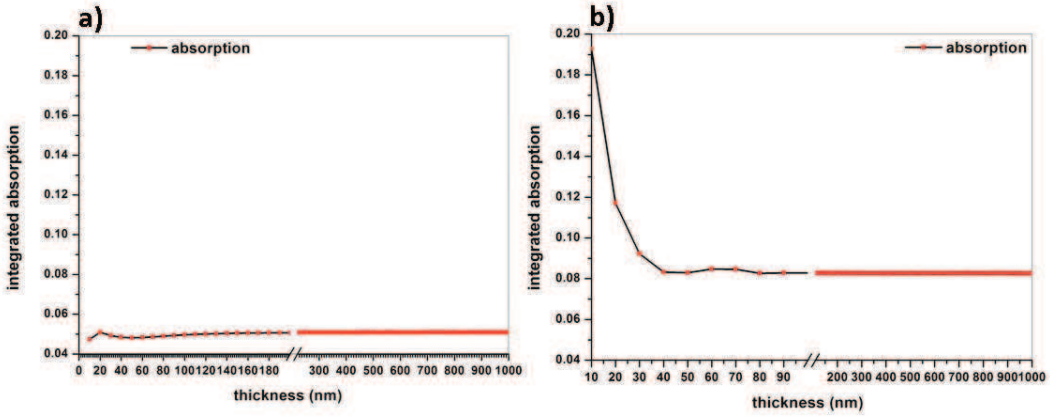

*Fig. 5.5. Integrated absorption comparison versus thickness of (**a**) Ag and (**b**) Al in [10, 1000] nm range with 10 nm step on a metal/glass stack*

Integrated absorption in Ag layer is always lower than in Al, for all the investigated thicknesses. It also clearly appears that in the case of an Ag layer, the thickness has no influence on the integrated absorption. In the case of A1, the integrated absorption is greatly increased for thicknesses lower than 40nm, and remains constant above this limit. Considering the necessity to decrease both the material consumption and the absorption losses in the bottom contact layer, we therefore choose to deposit metallic layers in the 50-100nm range.

We will now consider three possible designs of PC-assisted c-Si solar cells, with three different back contact structures: (1) a 100 nm thick Ag layer, (2) a 100 nm thick Al layer, and (3) a Ag (50 nm)/Al (50 nm) bi-layer. We will consider the specific configuration shown in Fig. 5.6, for the top layer and pattern shape, with a-Si and ZnO layers deposited on top of the patterns. For circumstantial reasons, this stack is slightly different from the general design displayed in the Fig. 5.4; we will come back later on the various possible designs of the top structure, and their respective advantages and drawbacks.

As in the case of the sole c-Si layer, we performed an optimization of the topographical parameters. The exploration of the lattice parameters is performed over the [450 nm, 550 nm] range, with 20 nm step, while *ffair* is scanned between 40 and 60% per step of 5%, and *h* is scanned in the [20 nm, 210 nm] range, per 20 nm step.

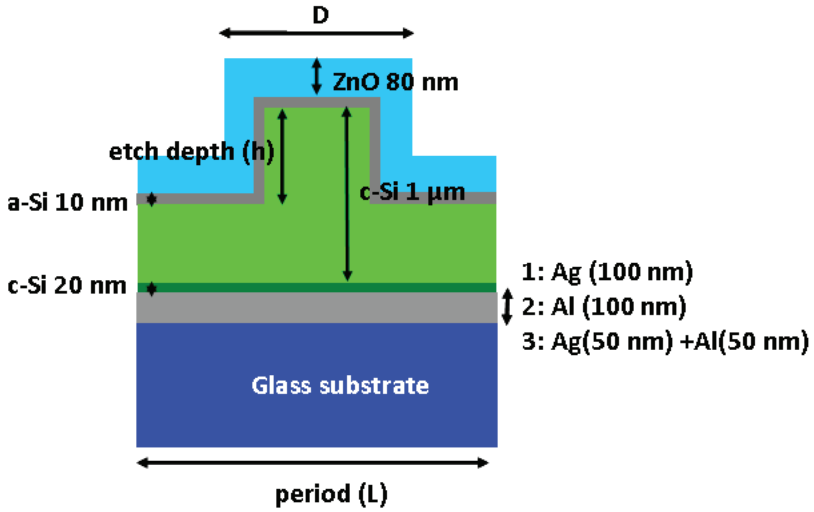

Fig. 5.6. Schematic view of the complete 1D patterned stack with different metal contactor

For the stack with an Ag or Ag/Al back electrode, the optimized topographical parameters are the same: L = 490 nm, *ffair* = 50% and h = 100 nm. However, for the stack with Al layer, the optimized parameters are L = 550 nm, *ffair* = 55% and h = 120 nm, which is different with other two stacks. But there is only 0.3% difference that the integrated absorption from the optimized parameters (L = 550 nm, *ffair* = 55% and h = 120) to the one with (L = 490 nm, *ffair* = 50% and h = 100 nm), which will be considered in the remainder of this section. Therefore, same lattice parameters (L = 490 nm, *ffair* = 50%, h = 100 nm) are used and results is displayed, in order to compare the integrated absorption in these three different stacks in Table.5.1.

Table.5.1 Integrated absorption comparison in each layer of stacks with different metal layer under same lattice parameters (L = 490 nm, ffair = 50%, h = 100 nm), then compared to their reference stacks.

Stack	**Integrated absorption**					
	whole stack	**metal layer**	**P^+ c-Si**	**n^+ a-Si :H**	**c-Si**	**ZnO**
a. Stack (**Ag**)	0.699	0.037	0.010	0.085	**0.477**	0.088
b. Stack (**Al**)	0.757	0.159	0.007	0.083	**0.426**	0.078
c. Stack (**Ag**+**Al**)	0.699	0.038	0.010	0.085	**0.477**	0.084
Reference (**Ag**)	0.493	0.027	0.008	0.054	**0.339**	0.054
Reference (**Al**)	0.564	0.126	0.006	0.053	**0.318**	0.050

Table 5.1 shows that integrated absorption of each layer in the stack with Ag and with Ag/Al are the same. Therefore, we focus mainly on the stack with Al or Ag. With Ag, integrated absorption in the c-Si layer and in the complete stack are up to 48% and 70% respectively, but the part of absorption light is consumed by other layers. Meanwhile, 30% of the incoming light is directly reflected by the front interface of air/ZnO. Although the stack with Al has higher absorption both in patterned stack and reference (Al), absorption in the active c-Si layer (42.6%), is lower than with Ag. After analysis of the absorption losses, it is found that the 100 nm thick Al has absorbed 15.9% of the incoming light compared with only 4% for Ag.

By comparing absorption spectra in the sole active layer of c-Si and in the metal layers (Fig. 5.7(**a)** and (**b)**), we can improve the calculations displayed in Table.5.1. Absorption spectra difference in the active c-Si layer is starts from 500 nm wavelength which is due to higher absorption in Al (See Fig. 5.7(**b**)).

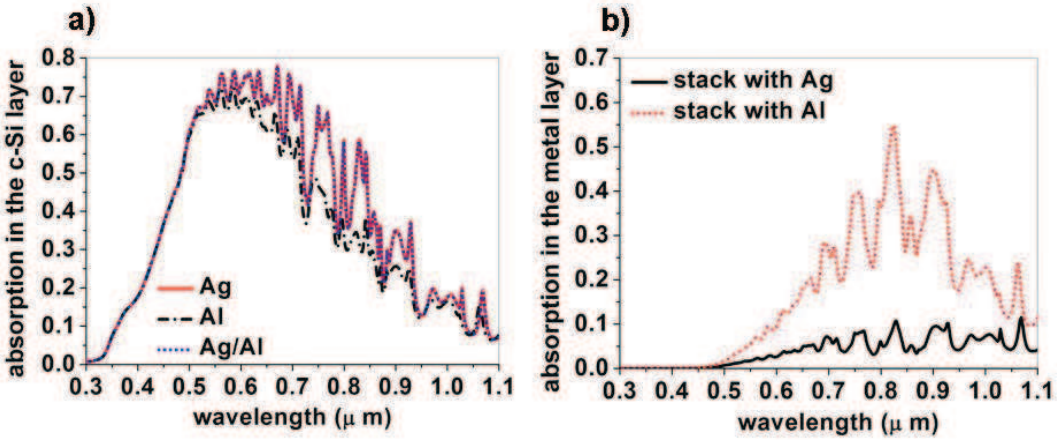

*Fig. 5.7. Average absorption spectra of TE and TM polarization in (**a**) the c-Si active layer and (**b**) the metal layer of the stack with different metal layer*

To sum up this subsection, the stack with Ag (100 nm) and the stack with Ag (50 nm)/Al (50 nm) lead to similar but higher integrated absorption in active c-Si layer: 48%. When using Al, useful absorption in the c-Si is lower due to the absorption within Al layer. Meanwhile, all patterned stacks show higher integrated absorption than their reference stacks.

5.3.3 Design of the top transparent conductive oxide layer

In this section, we will consider TCO layers based on ITO or ZnO. Indeed, they correspond to the most frequently used TCOs, with already well known optical and electrical characteristics.

Adjusting the thickness of the TCO is necessary to achieve a trade-off between the conductivity and the absorption coefficient of the top layer. The optimum TCO thickness is equal to 80 nm, requires an additional current collecting metal grid because the sheet resistance of such thin films is too high. A similar performance can be achieved with ITO and ZnO or ZnO:Al films [16] ZnO is a much more abundant material and promises cost reduction in long term due to the target cost. While, several hundreds nanometres film thickness of top ZnO are required to fulfil the requirement of a low TCO sheet resistance [17]. However, in order to perform electromagnetic simulations within a reasonable

time, we will limit our investigation to TCO thicknesses optimized for unpatterned solar cells. We will therefore consider two main devices, one with a 80 nm top ITO layer, and another one with a 240 nm ZnO layer. Additionally, for the sake of comparison, we will consider the unrealistic case of a 80nm ZnO layer.

As in the former sections, we will consider a structure similar to that exhibited in Fig. 5.6, with a 100 nm thick back Al layer, and the different TCO material and thicknesses, as introduced above. FDTD simulations are then performed, and *L*, *ffair* and *h* are scanned in order to optimize the integrated absorption for each configuration of TCO layer. The results are summarized in Table.5.2.

Table.5.2 Optimized integrated absorption comparison in each layer of stacks with different TCO layer or with different thicknesses of TCO layer. References are planar stack with TCO.

Lattice parameters of the stack with different TCO layer	**Integrated absorption**					
	whole stack	**Al**	**n^- c-Si**	**p^+ a-Si:H**	**c-Si**	**TCO**
ITO (80 nm): *L = 490 nm, ff = 50%, h = 100 nm*	0.784	0.139	0.006	0.085	**0.390**	0.154
Reference (ITO: **80** nm)	0.604	0.112	0.006	0.06	**0.318**	0.100
ZnO (240 nm): *L = 450 nm, ff = 55%, h = 90 nm*	0.795	0.104	0.004	0.07	**0.290**	0.322
Reference (ZnO: **240** nm)	0.662	0.089	0.004	0.05	**0.245**	0.269
ZnO (80 nm): *L = 540 nm, ff = 55%, h = 120 nm*	0.763	0.150	0.006	0.09	**0.435**	0.077
Reference (ZnO: **80** nm)	0.564	0.126	0.006	0.053	**0.318**	0.050

A first remark is that PC patterning increases the global absorption in the whole stack up to about the same value for all the three configurations. Indeed, the integrated absorption varies from 76.3 to 79.5% depending on the choice of the TCO layer. On the contrary, the useful part of the absorption efficiency – in the c-Si layer – exhibit strong variations depending on the configuration: from 29 to to

43.5%. This is essentially due to the absorption in the TCO layer: it is as low as 7.7% for a low absorption coefficient low thickness layer (80 nm of ZnO). Increasing the ZnO thickness to reach an electrically functional layer yields a prohibitive 32.2% absorption loss. In the case of the 80nm thick ITO layer, the TCO absorption losses are limited to 15.4%. Considering that the other sources of optical losses, in Al, and in the doped Si layers, are quite stable with the configuration, it clearly appears that the most appropriate is to deposit a 80 nm thick ITO layer.

Apart from the choice of the layer nature and thickness, another degree of freedom stands in the choice of the patterning and deposition techniques. Indeed, depending on the conformality of the deposition, and on the choice to perform the ITO deposition before or after patterning, the three configurations schematized in Fig. 5.8 may be obtained. In Fig. 5.8(**a**) and (**b**), the Al(100nm)/p^+ c-Si(20nm)/c-Si(1µm) stack is etched, and then n^+ a-Si layer is deposited by PECVD. ITO could then be deposited in a more or less conformal way, leading to the configuration depicted in Fig. 5.8(**a**) and (**b**). In the case of the structure displayed in Fig. 5.8(**c**), photonic crystal structure is realised after deposition of all the layers. It is clear that photon confinement in these three different structures may be different. For each configuration, the geometrical parameters are optimized in order to maximize the integrated absorption in the undoped c-Si, see Table 5.3.

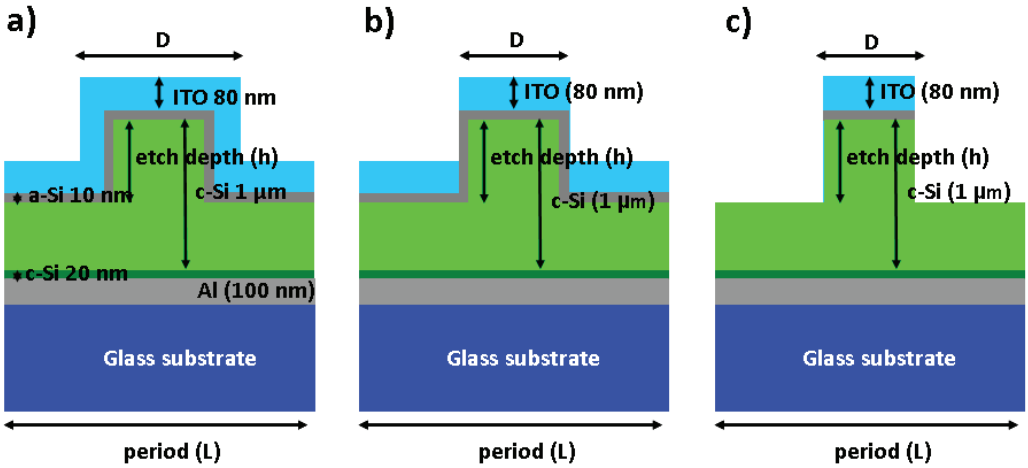

*Fig. 5.8. Schematic view of the complete patterned stack following different deposition techniques (**a-b**) and deposition order (**c**)*

Table.5.3 Optimized geometrical parameters and their integrated absorption in each layer of three stacks by comparing the unpatterned stack, as shown on Fig. 5.8

Lattice parameters of the stack	**Integrated absorption**					
	whole stack	**Al**	**n^- c-Si**	**p^+ a-Si:H**	**c-Si**	**ITO**
a): *L = 490 nm, ff = 50%, h = 100 nm*	0.784	0.139	0.006	0.09	**0.390**	0.154
b): *L = 540 nm, ff = 60%, h = 120 nm*	0.760	0.148	0.006	0.084	**0.400**	0.110
c): *L = 610 nm, ff = 65%, h = 140 nm*	0.749	0.153	0.006	0.06	**0.435**	0.082
Reference	0.604	0.112	0.006	0.06	**0.318**	0.100

As shown in Table.5.3, the integrated absorption in the patterned stacks and the sole active c-Si layers are all higher than in the reference, this is a new evidence of the positive impact of the integration of a photonic crystal in the solar cell. In the case of structure (**c**), light trapping and confinement in c-Si is significantly more efficient than for the other two structures. Indeed, the absorption in ITO layer and p^+ a-Si:H are lower. Additionally, the absorption

contribution in c-Si layer for structure (**a**) and (**b**) does not present obvious differences. It means that there is no need to carefully control the ITO deposition process. Finally it can be concluded that configuration (c) is expected to be more efficient in terms of light trapping. However, such a processing route does not include a direct way to passivate the etched Si sidewalls. At this point, it is not possible to conclude on the most appropriate configuration, since all will depend on the impact of the surface recombination of the carriers.

In conclusion of this section 5.3,

1) 100 nm Ag or Ag (50 nm)/Al (50 nm) back electrode reflect almost all incident light into the active c-Si layer, and has very low absorption in the metal layer. Still, considering the need to perform anodic bonding, the configuration based on a 100nm Al layer will be preferred to perform the first tests.
2) Considering both optical and electrical properties, the TCO should be based on an ITO layer with a thickness around 80 nm.
3) The highest absorption in c-Si layer is obtained when etching is realised after deposition of the complete stack. However, in order to reduce the surface recombinations, we will also consider the other possible configurations, which lead to a-Si:H and ITO deposition after the active layer patterning.

5.4 Absorption mechanisms in 1D and 2D patterned solar cells

In this section, we will consider a PC patterned solar cell structure as optimized in section 5.3. The stack includes a 100 Al layer, the c-Si active structure, and the deposited a-Si and ITO layers. We will consider a top structure designed to optimize the absorption in the undoped c-Si layer, i.e. with etched ITO, a-Si and c-Si layers. For the 1D PC structures, the geometrical parameters

are those optimized in section 5.3: L = 610 nm, *ffair* = 65%, h = 140 nm. As discussed in subsection 5.3.1 in the case of simple c-Si layers, the absorption efficiency of 2D PC is expected to lead to higher gains than their 1D counterpart. In that case, no systematic topographical parameter scanning was performed, with respect of the needed computing resources. For such 2D PC structures, we considered the same lattice parameter, surfacic *ffair* and etching depth as in the case of 1D PCs.

Figure 5.9 displays the wavelength integrated absorption in all the layers, together with the reflexion losses. 1D and 2D patterned structures are considered together with the unpatterned reference. As discussed above for 1D PCs, it clearly appears that absorption losses are mainly located in the Al and ITO layers; refining the topographical parameters for the 2D structure should reduce these contributions. Additionally, we can notice that the optical losses are more important in the case of 2D PCs than in the case of the reference, although the volume of ITO is lower. This illustrates that optical resonances also stand in the ITO layer, and not only in the high index c-Si active layer.

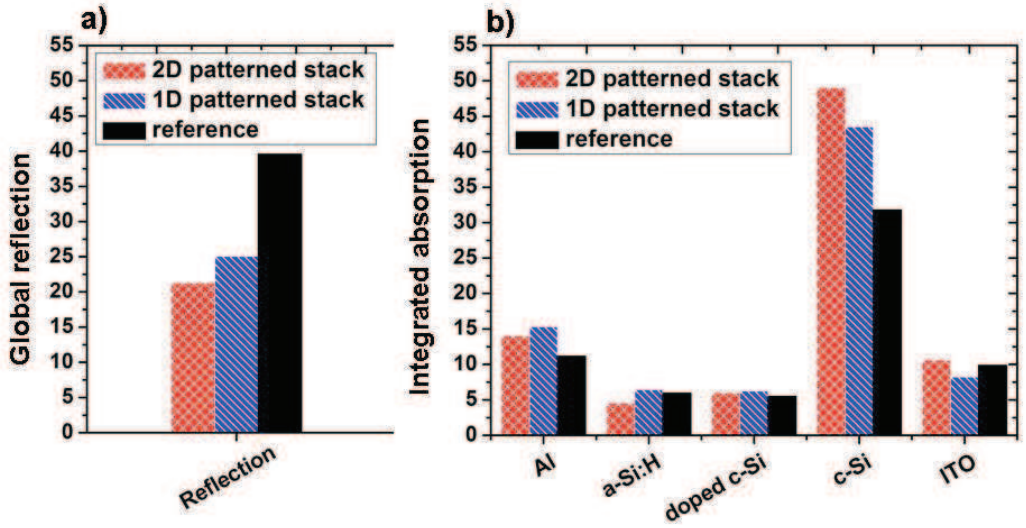

*Fig. 5.9. Global reflection (**a**) and integrated absorption in each layer (**b**) of the 2D PC and 1D PC patterned stacks (L, ffair and h set to 0.61* µm*, 35 % and 0.14* µm *respectively) by comparing to the reference stack (average value on both TE and TM polarizations)*

In order to discuss the absorption and light confinement mechanisms in more details, the absorption spectra in the 1D and 2D patterned complete stacks, the active c-Si layer and other layers are simulated and compared in the Fig. 5.10.

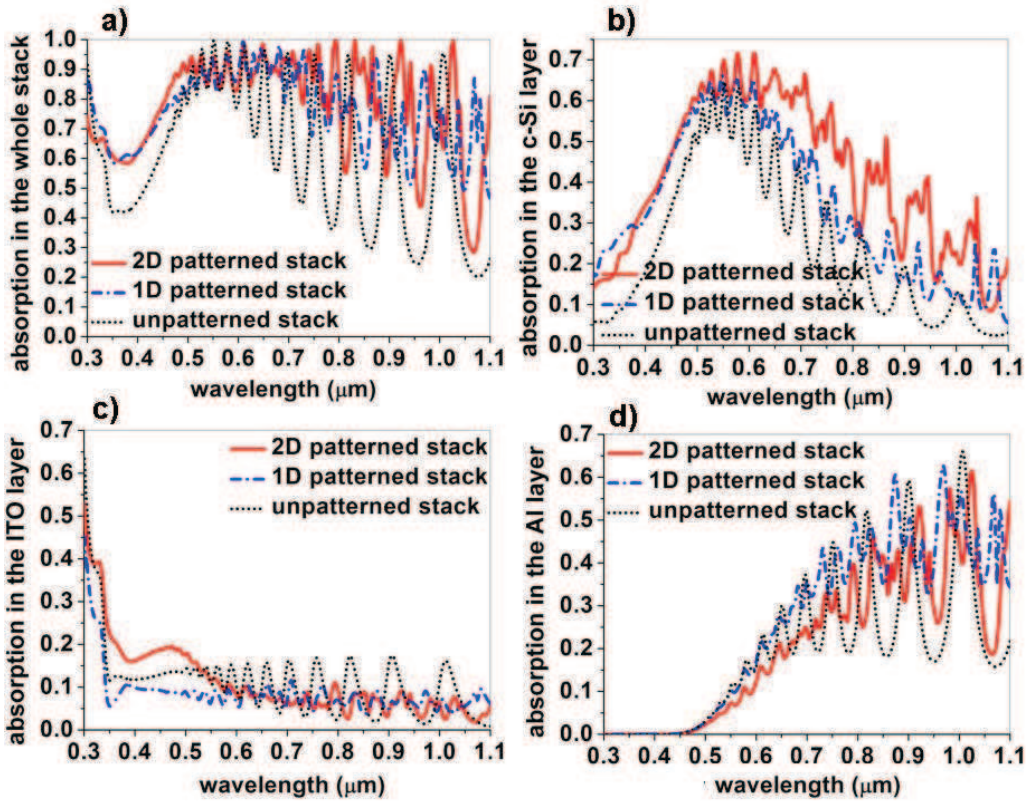

*Fig. 5.10. Average absorption spectra on both TE and TM polarizations in (**a**) the whole stack, (**b**) the sole c-Si layer, (**c**) the ITO and (**d**) the Al layer for the 1D and 2D PC patterned stacks (L, ffair and h set to 0.61* μm*, 35 % and 0.14* μm *respectively) obtained by simulation*

First, we can note from Fig. 5.10(**a**) and (**b**) that in the case of the 2D structures, the absorption losses in ITO mainly occur at low wavelength, while Al induce incident light absorption for wavelengths over 500nm. This it little surprising since incident light at low wavelength is absorbed in the first hundreds of nanometres of silicon. We also notice that, as already shown on Fig. 5.9, light is more efficiently absorbed in the c-Si layer for 2D PCs. More precisely, this absorption increase specifically appears at wavelengths above 600nm. A more careful analysis of Fig. 5.10 (**b**) leads us to split the absorption spectrum in three distinct ranges. Below 450nm, the absorption is continuously increased with the

wavelength, with no clear peak. In this first range, the absorption coefficient is so high that the incident light does not live long enough in the structure to generate an optical mode. The clear increase of the absorption with regards to the unpatterned stack is then related to an antireflective effect. Between 450 and 600nm, a regular series of peaks appear in the case of the 1D and 2D structures, but also for the unpatterned stack. These peaks are attributed to vertical Fabry-Perot resonances, which are characterized by a short photon lifetime. Over, 600nm, the absorption spectra of the PC structures exhibit a complex shape, including peaks which are not as regularly spaced as the Fabry-Perot resonances of the unpatterned structures. These peaks are attributed to the Bloch mode resonance of the PCs. These additional peaks clearly contribute to the absorption enhancement in the long wavelength range.

Figure 5.11 depicts contour plots of the integrated absorption, corresponding to the geometrical parameters which were scanned in the optimization phase, for a 1D PC structure. In the whole stack and c-Si layer, the integrated absorption in the complete stack and the c-Si layer are compared by a given L = 610 nm (shown on Fig. 5.11(**a)** and (**b)** and a fixed h = 140 nm, illuminated in the Fig. 5.11(**c)** and (**d)**.

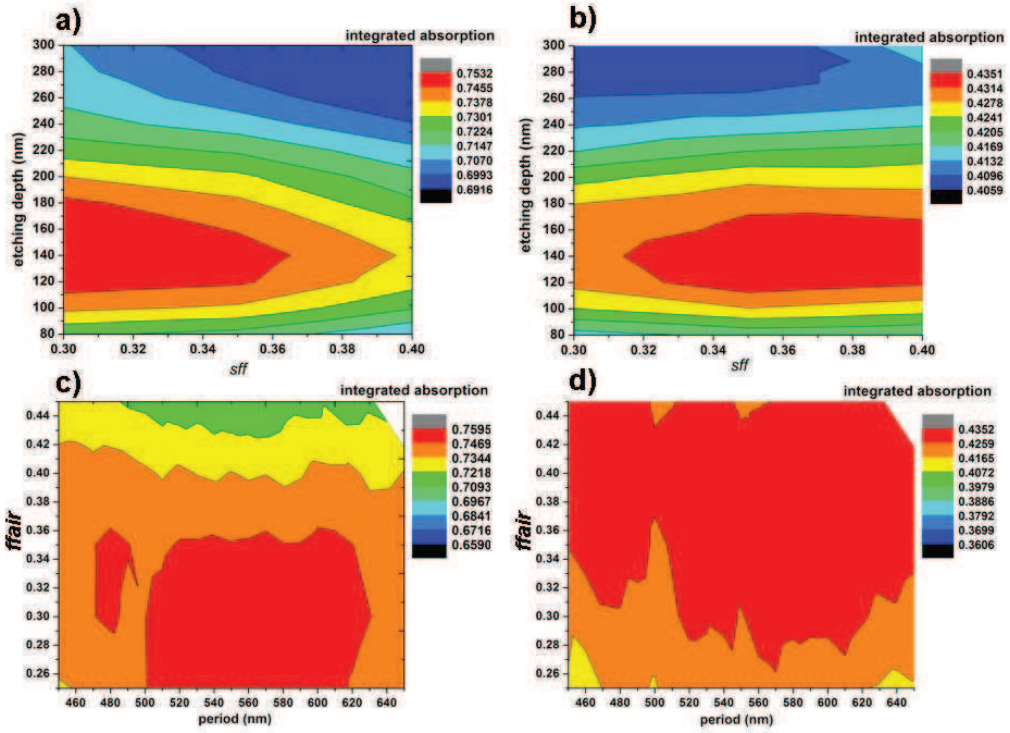

*Fig. 5.11. Contour map of the integrated absorption in the (**a**, **c**) 1D patterned stack and (**b**, **d**) c-Si layer under (**a**, **b**) fixed period at 610 nm, and (**c**, **d**) fixed h at 140 nm on the average of both TE and TM polarizations*

Figure 5.11(**a**) and (**b**) show that, a maximal integrated absorption of about 75 % is reached for a 120~160 nm etching depth and a 30~35% *ffair* with a very little impact of the period, (500-620 nm). The optimum value of the integrated absorption in the c-Si layer, around 43%, occurs for L = 0.5~0.6 µm, *ffair* = 35~45%, and h~140 nm. An important conclusion is that the absorption is quite robust when the topographical parameters fluctuate (L, *ffair* and h): a 5% variation could lead to less than 1% integrated absorption floating in the c-Si layer.

5.5 Fabrication and optical assessment of 1D and 2D PC patterned solar cell stacks

5.5.1 Fabrication of the PC patterned c-Si solar cell stack

In order to confirm the positive impact of the Photonic Crystal on an Epi-free solar cell stack, we fabricated preliminary demonstrators devoted to absorption efficiency assessment. The fabricated structures include all the layers that are needed for the final solar cells, i.e. the c-Si, the Al and the ITO layers. As a starting point, the Epifree stack is constituted of glass/Al(1µm)/c-Si(1µm), see Fig. 5.12(**a**).

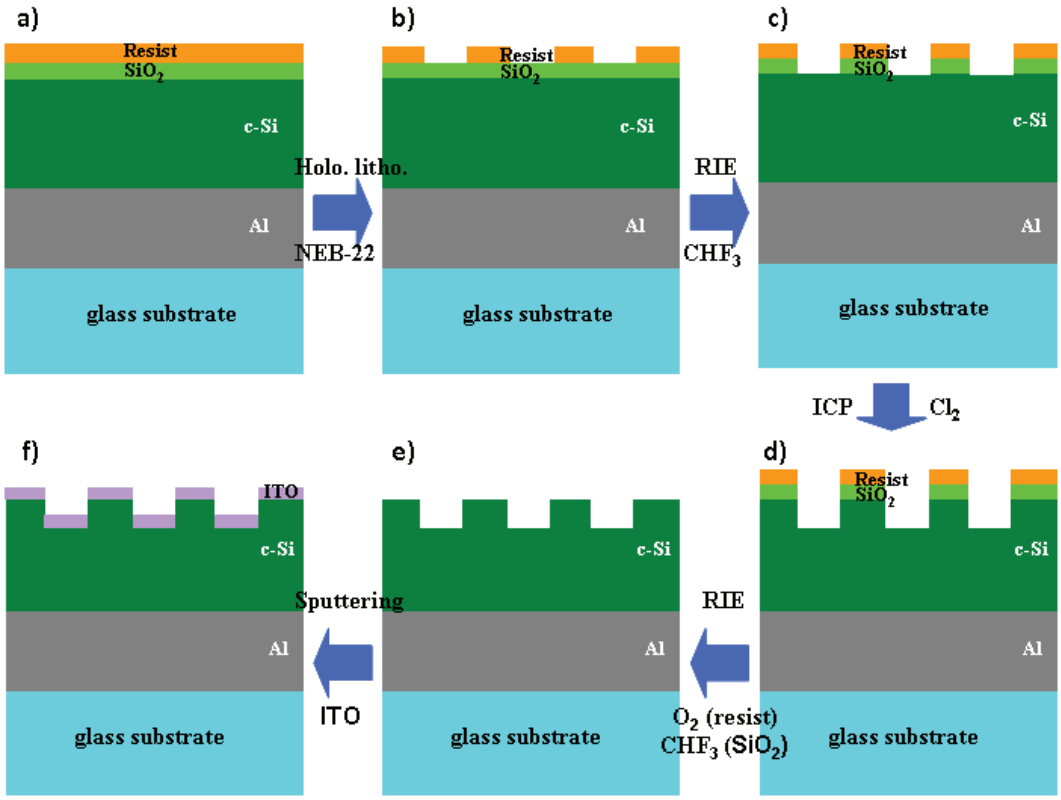

*Fig. 5.12. Main steps of the processes enabling to generate the patterned stack as a 1D and 2D PC through LHL (**a**, **b**), RIE(**c**, **e**) and ICP (**d**) combined with (**f**) final sputtering.*

A 0.1 µm thick SiO_2 layer is deposited by plasma-enhanced chemical vapour deposition (PECVD) on the top of this stack to act as a hard mask during the etching of the c-Si layer, and is further removed. This stack is then patterned using LHL (Fig. 5.12(**b**)), combined with RIE and ICP techniques [5,18]. The LHL process parameters [18] were adapted in order to reach the targeted parameters of the PC (lattice parameter *L*, *ffair* and *h*). After LHL, development, and a descum steps, the patterns are transferred into the SiO_2 hard mask (See Fig. 5.12(**c**)) using RIE process with a 16 sccm CHF_3 flow, at 15 mTorr, and with a power of 100 W for 900s. The c-Si layer is finally etched through the SiO_2 mask by ICP using 50 sccm for Cl_2, with an ICP power of 500 W and a RF power of 100 W, for 200s (see Fig. 5.4(**d**)). As a result of this combination of RIE and ICP, vertical sidewalls are obtained, as shown on the SEM profile views, Fig. 5.13(**b**) and (**d**). Then, the resist and SiO_2 are removed again by RIE (Fig. 5.12(**e**)). As shown in Fig. 5.13(**a**) and (**c**), the lines and holes are patterned with a reasonable regularity and roughness. The achieved period of 1D and 2D stacks are in the targeted range of 0.55-0.65 µm; the *ffair* is just in the range corresponding to the optimal configuration (35%-60%), and etching depth is just over the optimized 0.1-0.14 µm range. A 75 nm thick ITO layer is finally deposited at IMEC on top of the samples by sputtering (see Fig. 5.12(**f**)). On these first samples, the a-Si:H layer was not deposited since no solar cell processes were performed, and because its presence does not significantly affects the absorption efficiencies.

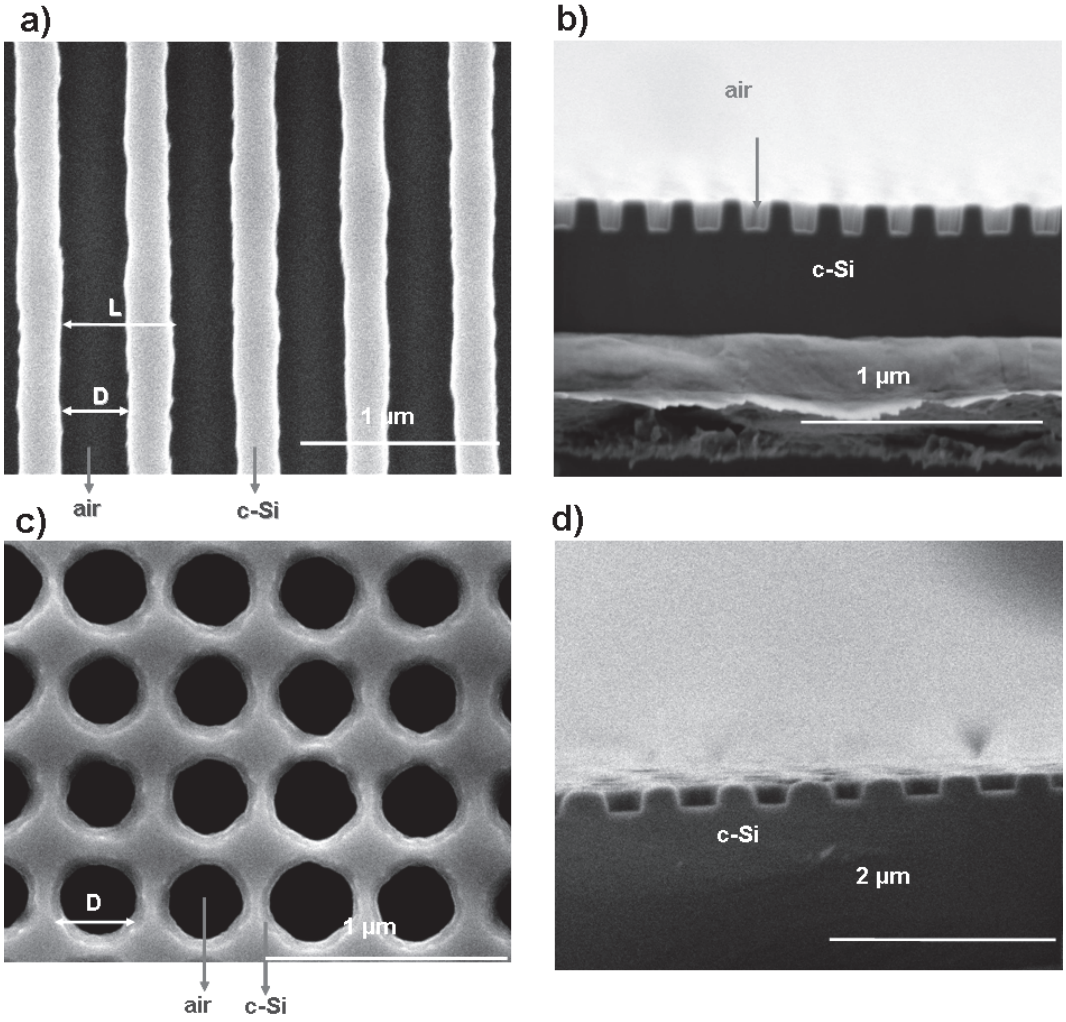

*Fig. 5.13. Top (**a**, **c**) and profile (**b**, **d**) view of a c-Si layer patterned as a 1D network (L ≈ 0.55 µm, D ≈ 0.28 µm) and a 2D network of round holes (L ≈ 0.55 µm, D ≈ 0.35 µm) into a 0.18–0.25 µm depth. Pictures obtained by SEM after removing the hard mask layer*

5.5.2 Absorption measurement of these 1D and 2D PC patterned c-Si ultra thin film solar cell stacks

In order to determine the optical properties of the patterned stack presented in Fig. 5.13(**a**) and (**b**), absorption measurements were performed using an integrating sphere at IMEC. In these experiments, the sample is illuminated by unpolarized light, so as to perform reflectance (R) and transmittance (T) measurements with a

~ 1 mm² spot size and with an 8° angle of incidence, as imposed by the integrating sphere measurement. The absorption $A(\lambda) = 1 - R(\lambda) - T(\lambda)$ is then simply derived. The absorption of the whole patterned stack was measured between 300 nm and 1100 nm with a 10 nm step. The absorption spectrum of the unpatterned stack was also measured as a reference. The corresponding spectra of 1D and 2D patterned stacks are simulated by FDTD. Measured and computed spectra are reported in Fig. 5.14 (**a**) and (**b**).

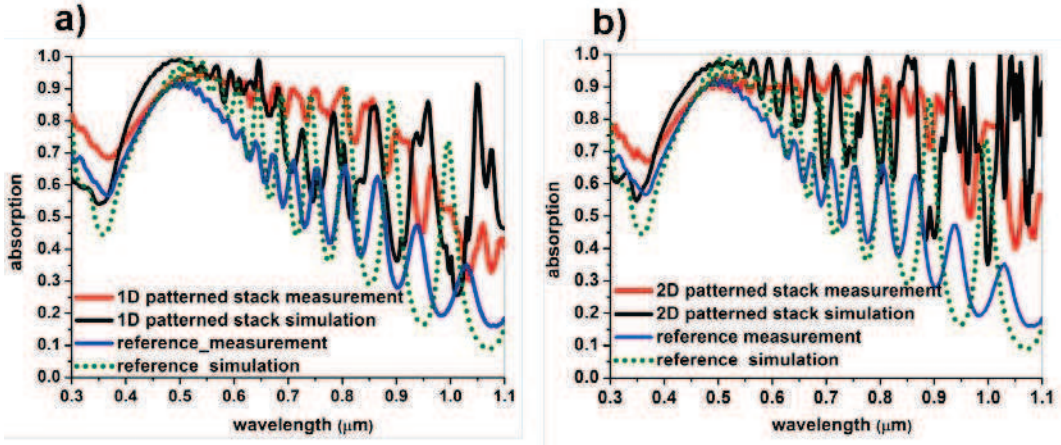

*Fig. 5.14. The simulated and the measured integrated absorption spectra comparison of the (**a**) 1D and (**b**) 2D patterned stack to the measured and simulated unpatterned stack*

The stacks which are really fabricated have been considered and calculated for that purpose. Due to an uncertain determination of the geometrical parameters, and the inhomogeneity of the *ffair* and measurement step length, as well as the roughness of the patterned cells, calculated and measured absorption spectra exhibit slightly different features. However, strong similarities are noticeable and the same general trends can be deduced both in 1D and 2D patterned stacks. As expected, the measured and simulated absorption spectra corresponding to patterned stacks display significantly higher values than for the unpatterned case. Moreover, the measured integrated absorption in the 2D and the 1D patterned stacks are 79% and 71% respectively, which are higher than the 50% reference.

In addition, the optical impact of a 75 nm thick ITO layer was analyzed for both the 1D and 2D patterned stacks. The measured absorption spectra are

displayed in Fig. 5.15.

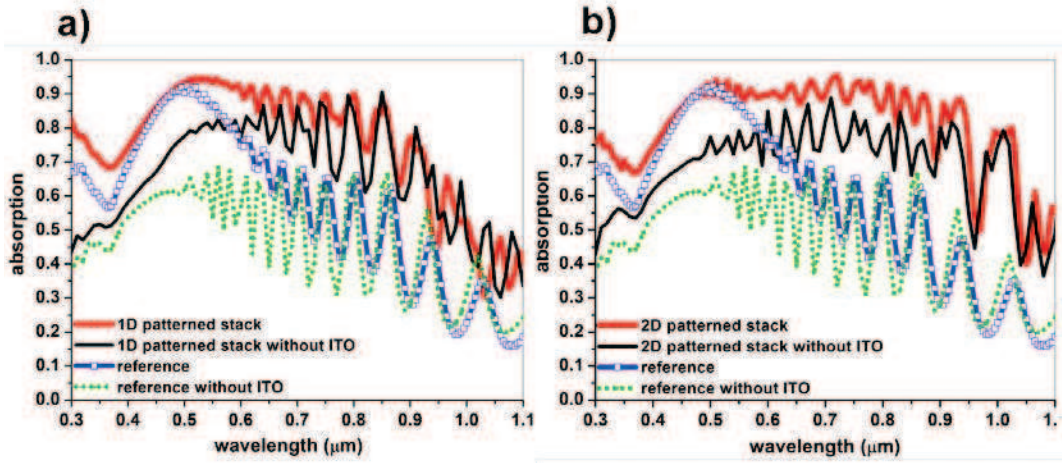

*Fig. 5.15. The measured absorption spectra comparison between the (**a**) 1D and (**b**) 2D patterned and the unpatterned stacks with and without front ITO layer*

Figure 5.15 shows that samples with ITO, either patterned or unpatterned, have a higher absorption than the ones without ITO. Given its thickness of 75 nm, the anti-reflection effect takes place around a resonance wavelength of ~550-600 nm. It indicates that the ITO layer fulfils its role of being an anti-reflector layer in the short wavelength range. It should also be mentioned that below 350nm, a substantial part of the incident light is absorbed in the ITO layer. This was already predicted in the simulated spectra displayed in Fig. 5.10.

Additionally, the influence of the angle of incidence (α) on the integrated absorption of the 1D and 2D patterned stacks was then investigated and compared to the reference stack, as displayed on Fig. 5.16(**a**). This corresponds to structures patterned with optimised parameters, including the 0.075 μm thick ITO layer. The integrated absorption is compared by varying the α in simulations [0°-86°], and in measurements [6°-46°] and [6°-26°] for patterned 1D and 2D stack, respectively. The angle of incidence range is reduced in the measurements due to the measurement setup and sample size limitations. The corresponding absorption spectra at α = 26°, both simulated and measured, are displayed in Fig. 5.16(**b**) and (**c**), in the case of 1D and 2D patterned stacks, respectively.

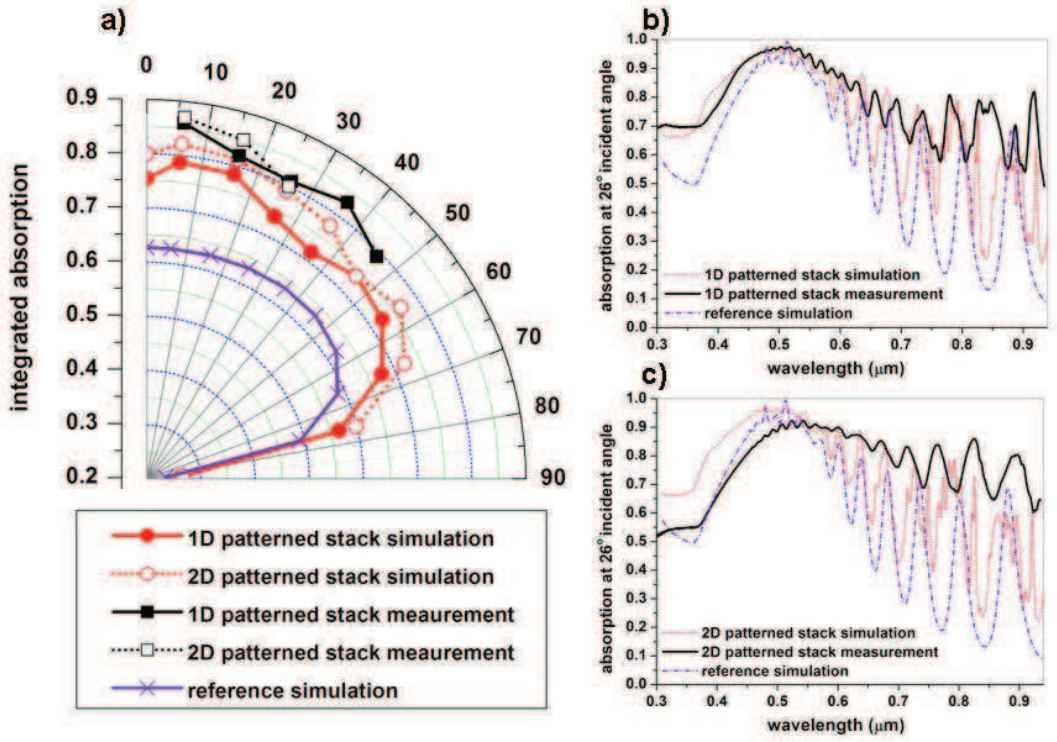

*Fig. 5.16. (**a**) the incident angle dependence comparison between simulation and measurement of the 1D and 2D patterned stacks, as well as a reference stack, the absorption spectra comparison at 26° incident angle in the (**b**) 1D patterned stack and (**c**) 2D patterned stack.*

Figure 5.16 first illustrates that patterned samples exhibit a higher integrated absorption at any angle of incidence. Moreover, although optical resonances are used to increase the absorption efficiency, the behaviour is little dependent on the angle of incidence. At $\alpha = 66°$, only a 8% and a 6% decrease in absolute value is observed compared to the value at $\alpha = 6°$ for the simulated 1D and 2D patterned stack, respectively. Besides, optical measurements reveal that there is a 7% decrease of the integrated absorption at $\alpha = 46°$ for the 1D patterned stacks and a 2% decrease of the integrated absorption at $\alpha = 26°$ for the 2D patterned ones. Such behaviour is of particular importance for solar cells without solar tracker. Figure 5.16(**b**) and (**c**) illustrate that the shape of the absorption spectra are extremely similar to those corresponding to normal incidence. However, it should be highlight that the simulated integrated absorption is higher at around 10° than at normal incidence. This is explained by the possibility to couple incident light

into resonances with a higher symmetry diversity at oblique incidence than at normal incidence [19]. Finally, it appears that the absorption is always lower in the theoretical case than when determined by measurements. Possible reasons for this quantitative discrepancy are the differences between the designed and the fabricated structures, for example the inhomogeneous lattice parameters, the etched profile slopes and roughness.

5.5.3 Electrical characterization of 2D PC patterned c-Si ultra thin film solar cell

Finally, electrical properties of patterned and unpatterned solar cells were measured in IMEC. The short circuit current density J_{sc} for 2D PC patterned and reference stacks are compared on Fig. 5.17.

It is noted that the measured solar cells are slightly different with the previous optimized stack. In these measured solar cells, the back p^+ doped c-Si is 250 nm thick instead of 20 nm thick for the simulated stack, and the front n^+ a-Si:H is 25 nm instead of 10 nm thick for the optimized stack. Also, n^+ a-Si:H and ITO were conformally deposited after PC realisation, shown on Fig. 5.18 (**d**).

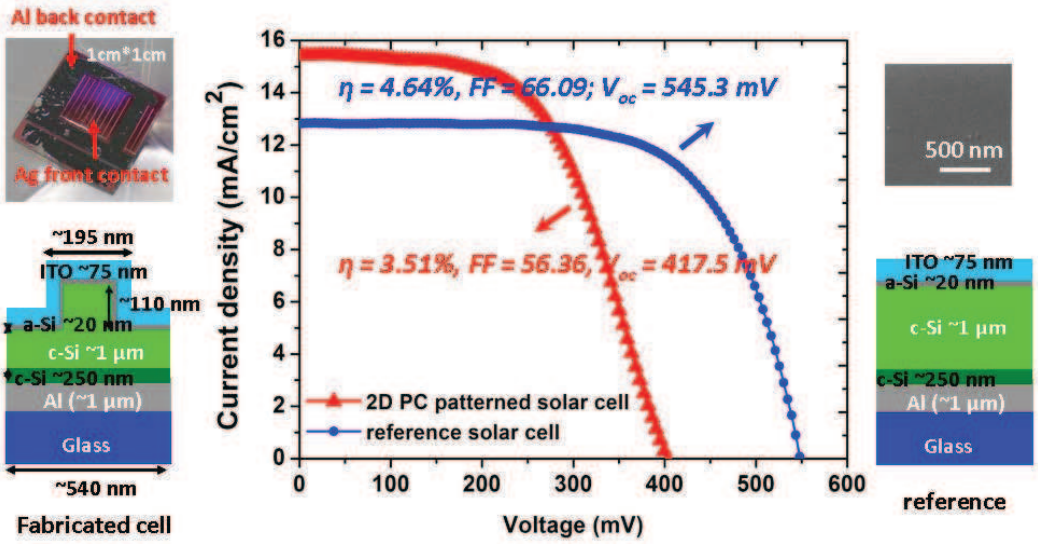

Fig. 5.17. Comparison of I(V) characteristics under illumination for the fabricated 2D PC patterned solar cell (left) and unpatterned solar cell reference (right)

The measured short circuit current density in 2D PC patterned solar cell is 15.43 mA/cm^2. The improvement is up to 20% when comparing to a similar but unpatterned planar solar cell reference (12.83 mA/cm^2). However, fill factor (FF) and Open Circuit Voltage (V_{oc}), therefore final efficiency (η) are deteriorated, respectively from 66 to 56%, from 547.8 to 403.4 mV and from 4.6 to 3.5%. We think it is mainly due to an ineffective passivation of the etched silicon surfaces (See Fig. 5.17).

Then the analyzed reflectance and external quantum efficiency (EQE) are compared in detail and shown on Fig. 5.18.

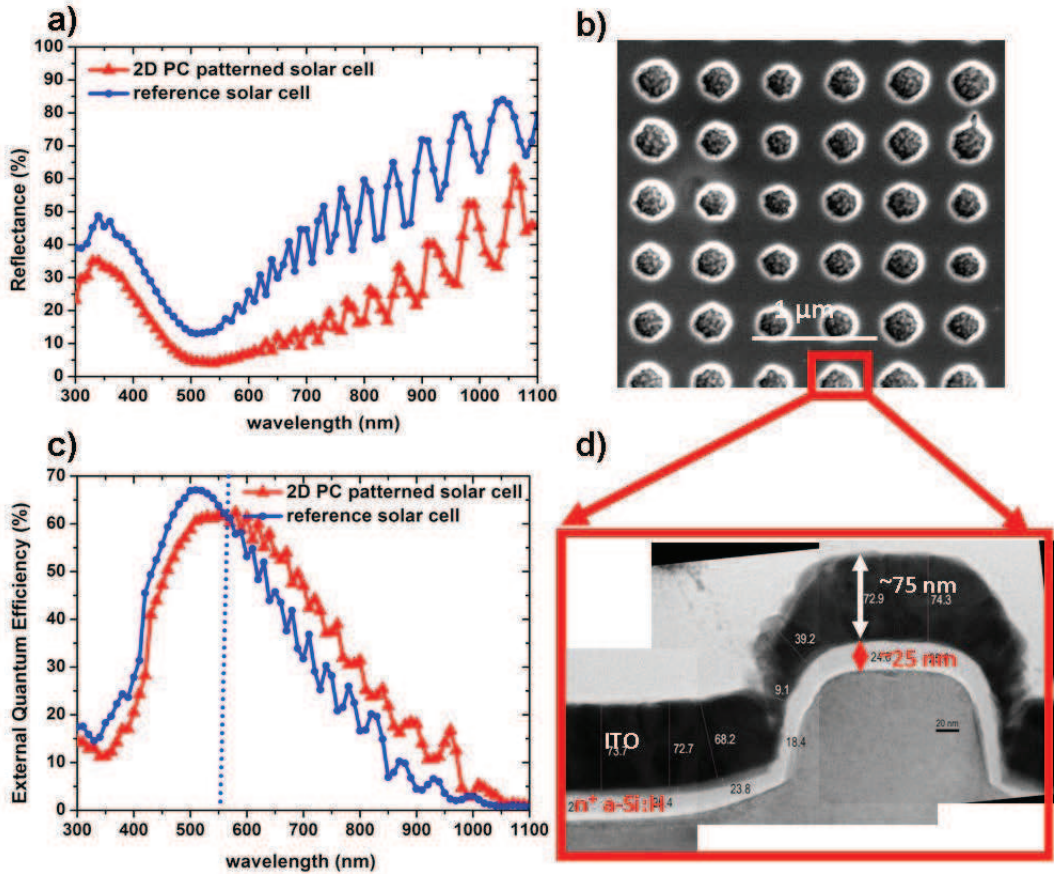

*Fig. 5.18. Comparison of (**a**) reflectance and (**c**) external quantum efficiency for the 2D PC patterned solar cell and unpatterned solar cell reference. The top view (SEM) and profile view (TEM) such 2D PC patterned solar cell.*

Figure 5.18(**a**) shows the reflectance of the structure versus wavelength. Reflection is lower than the reference solar cell in the whole interested

wavelength range, especially in long wavelength. It is due to the presence of photonic crystal and its resonant modes.

The external quantum efficiency (EQE) in PC patterned solar cell is only improved in long wavelength (550-1100 nm) range, above 550 nm (Fig. 5.18(**c**)). The lower EQE in short wavelength (300-550 nm) is attributed to the higher absorption losses in conformal deposited ITO and n^+ a-Si:H layers (Fig. 5.18(**d**)). Nevertheless, the improvement in long wavelength is more important than the losses in short wavelength range. This is why the J_{sc} for a PC patterned solar cell is higher than its reference solar cell in whole of interested wavelength range.

By comparing the optimized optical absorption enhancement of 50% with the current density enhancement of 20%, this difference is mainly due to a too large absorption in the conformal ITO and n^+ a-Si:H layers, a non optimal surface passivation and also due to the different doping profiles (back contact) and also due to a too large thickness of p^+ c-Si BSF. Therefore, these experimental results should be improved in the future when technology will be able to follow the requirements of theoretical optimisation.

Conclusion and outlook

Thin-film c-Si photovoltaic solar cells stacks integrating 1D or 2D PCs have been designed, fabricated and optically characterized.

- A photonic crystal assisted micrometer-thick structure shows an increased absorption in the active layer with proper nano-patterning parameters by up to 38 % for the 1D and 50 % for the 2D patterning, as compared to the unpatterned stack, from 300 nm to 1100 nm, taking into account the AM1.5G solar irradiance.
- A process based on LHL, RIE and ICP etching, has been developed to enable the generation of such 1D and 2D PC on a wide surface.
- Absorption spectra were measured using an integrating sphere. Both the patterned and unpatterned reference cell structures were measured and compared to spectra calculated by FDTD. Despite some discrepancies due to inaccuracies in geometrical parameters, measured and calculated absorption spectra exhibit a very similar behaviour.
- The fabricated stack exhibits a moderate dependence on the light angle of incidence, less than 10% absolute absorption decrease from normal incident light until 66°.
- The first 2D PC patterned solar cell shows higher short circuit current density 15.43 mA/cm^2 than a planar reference stack with a 20% improvement.
- Considering the optical consumption in other component of solar cells, other schemes, such as diffraction grating [20-24] and plasmonics [20,25], could be used to enhance the integrated absorption in solar cells. In the following chapter, we will focus on diffraction grating for a thin film solar cell.

References and links

[1] R. Brendel, "A novel process for ultrathin mono-crystalline silicon solar cells on glass," In *Proc. 14th European Photovoltaic Solar Energy Conf*, 1354 (1997).

[2] A. Fave, S. Quoizola, J. Kraiem, A. Kaminski, M. Lemiti, and A. Laugier, "Comparative study of lpe and vpe silicon thin film on porous sacrificial layer," *Thin solid films* **451**, 308–311 (2004).

[3] V. Depauw, Y. Qiu, K. Van Nieuwenhuysen, I. Gordon, and J. Poortmans, "Epitaxy-free monocrystalline silicon thin film: first steps beyond proof-of-concept solar cells," Progress in Photovoltaics: Research and Applications **19**, 844-850 (2010).

[4] X. Meng, V. Depauw, G. Gomard, O. El Daif, C. Trompoukis, E. Drouard, A. Fave, F. Dross, I. Gordon, and C. Seassal, "Design and fabrication of photonic crystals in epitaxy-free silicon for ultrathin solar cells," Proc. SPIE, 8312, 831207 (2011).

[5] X. Meng, V. Depauw, G. Gomard, O.EI Daif, C. Trompoukis, E. Drouard, C. Jamois, R. Orobtchouk, A. Fave, F. Dross, I. Gordon, and C. Seassal, "Absorbing photonic crystals for mono-crystalline silicon thin film solar cells," Proceedings of SPIE, 8425, 84250R (**2012**).

[6] A. Taflove, S. Hagness, *Computational Electrodynamics: The Finite-Difference Time-Domain Method* (Artech, 2005).

[7] http://www.lumerical.com/

[8] H.L. Hartnagel, A.L. Dawar, A.K. Jain, C. Jagadish, "Semiconducting Transparent Thin Films," Institute of Physics Publishing Bristol and Philadelphia, 134 and 219 (1995).

[9] R. Bel Hadj Tahar, T. Ban, Y. Ohya, Y. Takahashi, "Tin doped indium oxide thin films: Electrical properties," J. Appl. Phys. **83**, 2631(1998).

[10] J. Pla, M. Tamasi, R. Rizzoli, M. Losurdo, E. Centurioni, C. Summonte, and F. Rubinelli, "Optimization of ito layers for applications in a-si/c-si heterojunction solar cells," Thin Solid Films **425**, 185-192 (2003).

[11] G. G. Granqvist and A. Huiltaker, "Transparent and conducting ITO films: new developments and applications," Thin Solid Film **411**, 1-5 (2002).

[12] W. Beyer, J. Hupkes, and H. Stiebig, "Transparent conducting oxide films for thin film silicon photovoltaics," Thin Solid Films, **516**, 147-154 (2007).

[13] M. Berginski, J. Hupkes, M. Schulte, G. Schope, H. Stiebig, B. Rech, and M. Wuttig, "The effect of front ZnO: Al surface texture and optical transparency on efficient light trapping in silicon thin-film solar cells," J. Appl. Phys. **101**, 074903 (2007).

[14] Oliver Nast, Stephan Brehme, Stephen Pritchard, Armin G Aberle, and Stuart R Wenham, "Aluminium-induced crystallisation of silicon on glass for thin-film solar cells," Sol. En. Mat. Sol. Cells **65**, 385-392 (2001).

[15] Mohamed M. Hilali, Mowafak M. Al-Jassim, Bobby To, Helio Moutinho, Ajeet Rohatgi, and Sally Asher, "Understanding the formation and temperature dependence of thick-film Ag contacts on high-sheet-resistance Si emitters for solar cells," J. Elec. Soc., **152**, G742–G749 (2005).

[16] O. Kluth, A. Loffl, S. Wieder, C. Beneking, W. Appenzeller, L. Houben, B. Rech, H. Wagner, S. Hoffmann, R. Waser, et al, "Texture etched al-doped zno: a new material for enhanced light trapping in thin film solar cells," In *Photovoltaic Specialists Conference, 1997., Conference Record of the Twenty-Sixth IEEE*, 715–718 (1997).

[17] B. Rech and H. Wagner, "Potential of amorphous silicon for solar cells," *Appl. Phys. A. Materials Science & Processing* **69**, 155–167 (1999).

[18] X Meng, G. Gomard, O. El Daif, E. Drouard, R. Orobtchouk, A. Kaminski, A. Fave, M. Lemiti, A. Abramov, P. Roca i Cabarrocas and C. Seassal, "Absorbing photonic crystals for silicon thin-film solar cells: Design, fabrication and experimental investigation," Sol. En. Mat. Sol. Cells **95**, 32–38 (2011).

[19] O. El Daif, E. Drouard, G. Gomard, A. Kaminski, A. Fave, M. Lemiti, S. Ahn, S. Kim, P. Roca i Cabarrocas, H. Jeon, and C. Seassal, "Absorbing one-dimensional planar photonic crystal for amorphous silicon solar cell," Opt. Express **18**, A293-A299 (2010).

[20] F Duerinckx and J Szlufcik, "Defect passivation of industrial multi-crystalline solar cells based on pecvd silicon nitride," Sol. En. Mat. Sol. Cells **72**, 231-246 (2002).

[21] Claus Heine and Rudolf H. Morf, "Submicrometer gratings for solar energy applications," Appl. Opt. **34**, 2476–2482 (1995).

[22] Dennis M. Callahan, Jeremy N. Munday, and Harry A. Atwater, "Solar cell light trapping beyond the ray optic limit," Nano Lett. **12**, 214–218 (2012).

[23] J.Krc, M,Zeman et al, "Modulated photonic-crystal structures as broadband back reflector in thin-film solar cells," Appl. Phys. Lett. **94**, 153501 (2009).

[24] M.Berginski, J.Hupkes, et al, The effect of front ZnO:Al surface texture and optical transparency on efficient light trapping in Silicon thin film solar cells, J. Appl. Phys. **101**, 074903 (2007).

[25] S. Pillai, K. R. Catchpole, T. Trupke, and M. A. Green, "Surface plasmon enhanced silicon solar cells," J. Appl. Phys. **101**, 093105 (2007).

Chapter 6

Design and fabrication of ultra thin film c-Si solar cells with front and back diffraction grating

6.1 Introduction

In this chapter, we propose an original design to boost the absorption enhancement obtained using a single diffraction grating. This design involves two gratings having different periods at the front and at the back interfaces of the active layer. Each grating is intended to play a specific role:

- The front grating has to enhance the light coupling into the active, in a spectral range as broad as possible, so to reduce the reflectance;
- The back grating has to diffract the light that has not been absorbed in a single pass back into the active layer.

Up to now, these concepts have been proposed separately. [1-2] For instance, gratings as back reflectors can be patterned on transparent and conductive oxides (TCO) [10-14] or on metallic layers [3-5]. Other groups proposed to use such gratings as front anti-reflection layers [6] to reduce the reflection at the short wavelengths on c-Si [7].

Recently, Mutitu and al. [2], Dewan and al. [8] and K. Wang and al. [9] have developed new designs based on multiple grating structures and reported an increase of the optical path length by simulation, together with an enhancement of the short circuit current [2, 5-6, 8-12]. However, neither the effect of grating height, nor the influence of the period, filling factor for the front and the back diffraction gratings were investigated based on the real fabrication feasibility. This remains one of the most important meaningful investigations for the front and back gratings solar cells.

In this chapter, we investigate and optimize one- or two dimensional (1D or 2D) back-side and front-side diffraction grating solar cells. We propose to implement simultaneously the front grating by patterning directly the absorbing c-Si layer, and the back grating by patterning the back electrode, through its TCO or its metallic layer in a complete solar cell.

The finite difference time domain (FDTD) method is used to optimize the gratings parameters in order to achieve a maximum increase of the absorption in the c-Si layer. The optical simulation based on 1.2 μm thick c-Si layer with back or front 1D gratings is introduced. The influence of the height and the period of different back interfaces are studied based on semi-infinite c-Si at c-Si/ZnO interface and at the ZnO/Ag interface. And then the influence of the period and filling factor of the front grating is introduced. Based on the investigation of devices including a back or a front grating, various double 1D grating configurations are then proposed and discussed. According to the simulations on 1D back and front gratings, the targeted complete solar cells are simulated and compared. Additionally, the optical properties and short circuit current of the optimized structure are investigated by studying its absorption spectra and the electric field mappings. Moreover, the front and back 2D gratings stack is studied by analyzing the absorption spectra and photocurrent. Finally, a fabrication route to generate such kind of double 1D and 2D gratings structures are proposed: the double 1D and 2D gratings devices with different periods are generated by associating laser holographic lithography (LHL) with reactive ion etching (RIE) and inductively coupled plasma (ICP) etching steps combined with several deposition techniques. At the end of this chapter, the optical properties of such double grating solar cell devices are characterized.

6.2 Absorption of front and back 1D gratings on single c-Si layer

The most important property of the grating is to increase the path length of photons inside the absorbing layer by coupling the light to non-zero diffraction orders. Preliminary investigations are conducted on a 1 μm thick c-Si, which is 1D patterned, as shown in Fig. 6.1(**a**)-(**d**). The front period, 200 nm, and the back

period, 800 nm, are arbitrary chosen for these simulation tests. For all the gratings, the air filling factor (*ffair* = *width/period*) is defined as the width of the high index material slices divided by the period A grating filling fraction (*ffair*) of 50% will be considered, a value easily achievable by most of the nanopatterning technologies (holographic lithography, or nano-imprint and so on). The groove height (depth) is set as 100 nm for the front and back grating. Moreover, we concentrate on TM polarization (along the *y* axis (Fig. 6.2), i. e. electric field orthogonal to the slits.

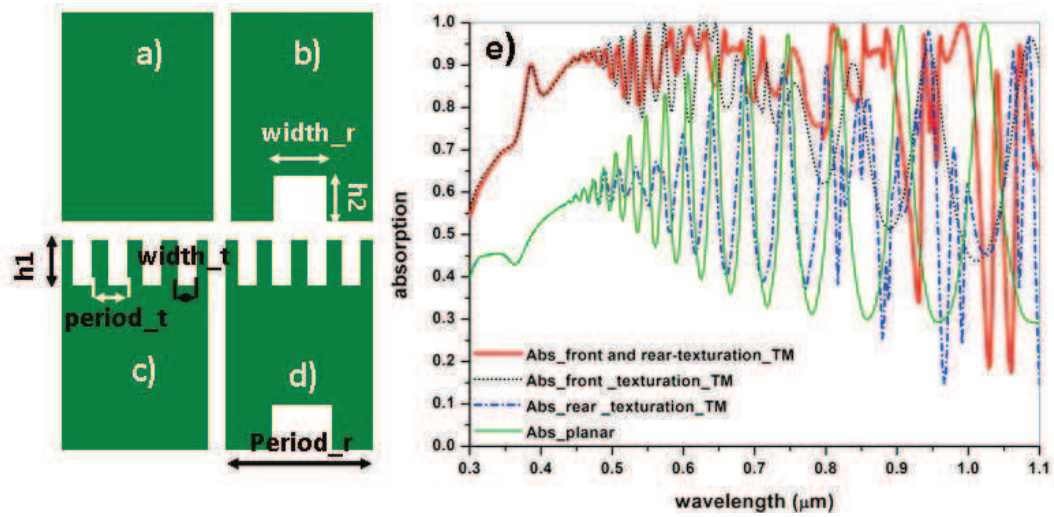

*Fig. 6.1. (**a**) Planar (**b**) back patterned (**c**) front patterned and (**d**) front and back patterned configurations on a 1μm thick c-Si layer (**e**) Optical absorption spectra comparison of those 4 configurations, based on TM polarization*

As shown on Fig. 6.1(**e**), for the planar c-Si layer, from about 450 nm to 1100 nm, the clearly visible absorption resonances correspond to Fabry-Perot modes thanks to the large index contrast between air and c-Si layer. If these resonances can lead to a complete absorption of the incident light, the spectral density of modes is limited by the low thickness of the layer, leading to low integrated absorption on the whole spectral range. Moreover, the large index contrast is also responsible of the low (~50%) absorption for the shorter wavelengths, since the reflexion is too high. Then, the envisaged roles of the texturations are twofold:

- to reduce the reflexion in whole of interested wavelength range,
- to increase the spectral density of modes at large wavelength range.

According to the spectra of Fig. 6.1(**e**), the last issue can be addressed using a back texturation; the absorption peaks are not only due to Fabry-Perot resonances along the vertical direction but also from the Fabry-Perot resonances along directions of diffraction, as can be clearly seen above 800 nm.

Concerning the first issue, it can even be addressed using a front grating: the absorption is strongly improved at shorter wavelength, but it then remains quite low at the longer wavelength.

Finally, both issues are addressed using both front and back 1D grating c-Si layer and lead to a 55% absorption in the active layer. This improvement is up to 75% compared to the absorption in the planar 1 μm thick c-Si layer. Meanwhile, the integrated absorption of the back grating stack and the front grating stack are still higher than the planar c-Si layer by 5% and 68% respectively.

6.3 Front and back grating solar cell design

6.3.1 Structure description

The whole solar cell structure investigated in this work is a stack composed, from the back to the front, of a 100 nm thick silver (Ag) layer, a 120 nm thick zinc oxide (ZnO) layer, a c-Si layer with a thickness in the 600 nm-2 μm range, used as the active material (p+-i- n^+ junction), overlaid by an 80 nm thick indium tin oxide (ITO) layer (see Fig. 6.2(**a**)).

On the back side, the c-Si/ZnO interface is patterned as a 1D / 2D grating, whereas on the top, the c-Si and ITO layers are patterned as a 1D / 2D grating

with a different period (Fig. 6.2(**b**)). The optical indices of the materials (ITO, c-Si, ZnO [13] and Ag [13]) are included in the Annex. A.

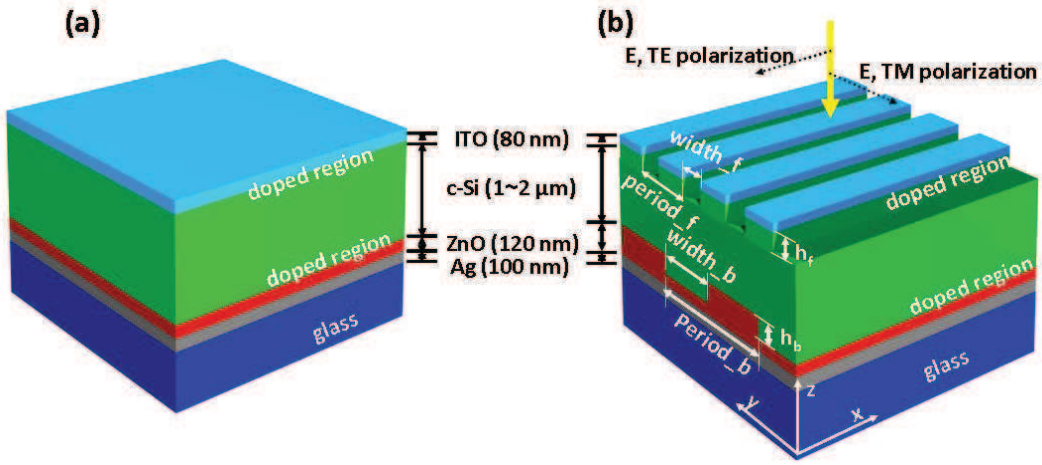

*Fig. 6.2. Schematic views of the investigated complete (**a**) unpatterned stack (reference) and (**b**) patterned stack with the front and back 1D diffraction grating with different periods*

The thickness of 80 nm for the ITO layer is high enough to enable a low sheet resistance, so low lateral transport losses of the carriers over hundreds of microns to lateral metallic contacts. In the same time, this value yields a low optical absorption. In an unpatterned solar cell, this ITO layer, with its refractive index around 2, also plays the role of an anti-reflection coating for red light. In the case of patterned solar cells, this material will further contribute to the anti-reflective effect of the front grating. On the back side of the cell, the silver electrode also acts as an almost perfect reflector. It is assisted by the ZnO or TCO layer which prevents from the diffusion of Ag into c-Si [14], and which exhibits a particularly low optical absorption (see appendix). Incident light is then expected to be preferentially absorbed in the c-Si layer, while the photogenerated carriers are collected by the ITO and ZnO/Ag layers. A grating *ffair* of 50% will be considered, a value easily achievable by most of the nanopatterning technologies [8, 15].

6.3.2 Design rules for 1D front and back gratings

In this section, we discuss on the respective roles of the front and back gratings. For the sake of simplicity, and to provide simple guidelines for the design of these structures, non dispersive materials will be considered, with $n = 4$ and $k = 0$ for c-Si; $n = 2$ and $k = 0$ for ZnO and ITO. We consider 1D gratings and an incident plane wave with a TM polarization (along the y axis, i.e. electric field orthogonal to the slits).

a. Design of the back grating

The expected role of the back diffraction grating is to trap the incident light at long wavelengths into guided modes, in such a way to increase photon lifetime in the active medium. To reach this goal, a periodic grating is implemented on the ZnO layer, on top of the Ag electrode (see Fig. 6.2), in order to diffract back the incident light into c-Si.

In the case of a simple 1D diffraction grating, the angles of the diffracted orders are calculated using the grating equation:

$$\sin\theta_m + \sin\theta_i = +m\lambda / \Lambda_b n_d \qquad (2)$$

where n_d is the refractive index, λ is the wavelength in vacuum, Λb is the grating period, m is the diffraction order (0, ±1, ±2…), θ_i is the incident angle, θ_m is the diffraction angle for the m_{th} order. As the main purpose of the back grating is to increase the absorption at longer wavelengths (from 700-1100 nm for c-Si), the specular reflection in the order 0 should be attenuated for the profit of diffracted orders with. Incident light will then be reflected with a larger propagating angle θ_m, thereby increasing the optical path length, and potentially trapping photons into guided modes in the c-Si layer. Following these considerations, a relatively large lattice parameter should be selected in order to generate non zero diffraction orders [16].

In order to determine in a more quantitative way the opto-geometrical parameters of the back grating, we now consider the structure displayed Fig.

6.3(**a**), and combining the patterned 120 nm ZnO layer, the 100 nm thick Ag reflector and the c-Si medium, here considered as semi-infinite. This structure is simulated by FDTD, with a view to investigate the impact of the corrugation depth (h_b) and of the lattice parameter of the grating.

Figure 6.3(**b**) illustrates the influence of h_b, considering a 500 nm period. Since this depth should be limited considering the processing time and feasibility, a value of 100 nm appears as an optimum since the 0th order is then minimized, while all the light is almost fully diffracted on the +/-1 orders.

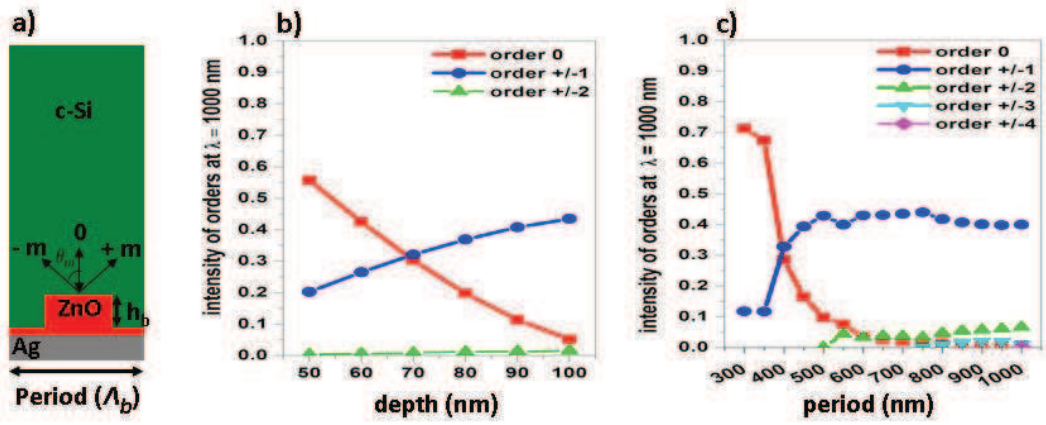

*Fig. 6.3. Schematic view of the back grating structure (**a**); influence of the grating depth (**b**) and period (**c**) on the light intensity distribution on the diffracted orders, for a TM polarization.*

The impact of the grating period is then evaluated (see Fig. 6.3(**c**)), for a 100 nm corrugation depth. As expected, additional orders appear for increased periods, but the intensities corresponding to orders larger than 1 remains very limited, even for a 1µm period. Considering these results, together with the tendencies expected from the grating equation (2), the choice of the period is thus a compromise between a large period to increase the number of diffraction orders, and to reduce the intensity on the order 0, and a small period, to keep a large enough diffracted angle for the first order mode. The grating period will therefore be set to 750 nm.

b. Design of the front grating

As for the case for the back grating, the period (Λ_f) is also a key parameter for the design of the front grating. In this section, we will consider a periodic structure composed of ITO/c-Si patterns, as depicted in Fig. 6.4(**a**). Its behaviour will be explored in the 300-1100 nm wavelength range, considering a semi-infinite c-Si medium. The main objective is to reduce the reflection at the front surface, while considering technologically feasible geometrical parameters. For these reasons, we will consider patterns with an ITO section of 80 nm thick and a c-Si section of 100 nm deep. Fig. 6.4(**b**) shows the influence of the front grating period, tuned from 100 nm to 750 nm, on the amount of light reflected at the front surface.

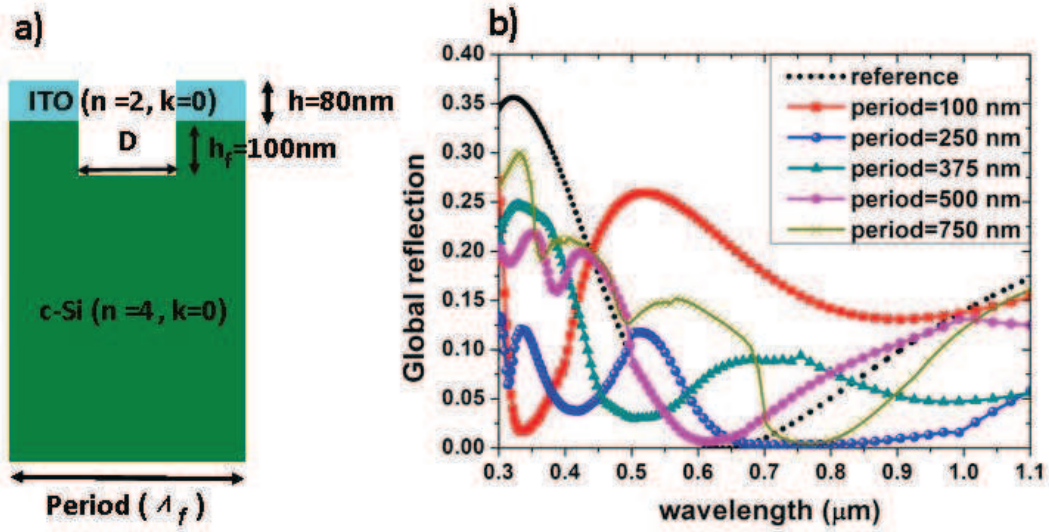

*Fig. 6.4. Schematic view of the front grating (**a**), and reflected intensity versus the wavelength, for various grating periods and considering a TM polarization, and a 50% ffair; the reference corresponds to a planar Si surface covered by a 80nm thick ITO layer (**b**).*

While the ITO layer of the planar ITO/c-Si reference acts as an efficient anti-reflector around 600 nm, it is much less the case for the lower wavelength range, i.e. below 500 nm. On the contrary, the simulated spectra show that the patterned structures exhibit a lower global reflection compared to the reference for all the considered periods, in the whole 300-450 nm wavelength range. It means that the

patterned ITO/c-Si acts as an efficient anti-reflector to decrease the global reflection in this short wavelength range. This can be attributed to a better impedance matching between air and silicon, but also to diffraction processes. In particular, for periods smaller than the wavelength, light is not reflected in diffraction orders than 0 in air, whereas transmission into c-Si is made possible through more diffraction orders (0 and +/- 1). In the specific case of the patterned interface with a 250 nm period, the simulated spectrum demonstrates a low global reflection in the short (300-450 nm), mid (450-700nm) and long-wavelength (700-1100 nm) ranges. This period will therefore be selected for the front grating, in order to trap most of the incident light into the c-Si active layer.

6.4 Combined front and back grating solar cell: global design and analysis

So far, the front and the back gratings have been introduced and optimized separately, with a view to select their geometrical parameters. In this section, we propose to implement a double grating structure from the design rules previously derived. The role of each grating can be understood from the previous studies. On one hand, the short period front grating is intended to reduce the reflection and thus to diffract the incident light in the whole spectral range into the active c-Si layer. On the other hand, the large period back grating is intended to diffract back the incident light into the active layer, mainly in the red to near infrared ranges of the spectrum (700-1100 nm). In this section, we consider the complex indices and dispersion characteristics of all the real materials used. The optical indices of ITO [from ellipsometric measurement] and c-Si [from ellipsometric measurement], ZnO [13] and Ag [13] are included in Annex. A. We derive the photocurrent along with the methodology introduced in section 2.1.

6.4.1 Analysis of the 1D double grating solar cell

We first analyze the spectral behaviour of the double grating solar cell structures, considering the design parameters derived from section 2, including a 250 nm period front grating, a 750 nm period back grating, and 50% filling fraction for both gratings. This set of parameters also enables the use of a simple unit cell for the FDTD simulation. A 1.2 µm thick c-Si layer is considered, including the 100 nm thick corrugated sections on the top and on the bottom parts of the layer. Fig. 6.4 shows the absorption spectra for such a device, considering only the useful part of the absorption, i.e. in the c-Si layer. The double grating structure is compared to structures including only the front or the back grating. Fig. 6.5(**a**) exhibits the spectra corresponding to a TM polarized incident light, as in the case of section 2, while Fig. 6.5(**b**) correspond to a TE polarized light. Below 500 nm, the absorption is always higher when a front grating is integrated, as compared to the device including only the back grating. This confirms that the front grating acts as an efficient anti-reflecting structure, for both polarizations. One should note that in this short wavelength range, no absorption peaks appear, since the absorption length of c-Si is lower than the layer thickness. In the intermediate wavelength range, i.e. between 500 and 700 nm, most of the absorption peaks are regularly spaced, and attributed to Fabry-Perot-like resonances. Apart from a slightly higher mean absorption in the case of the double grating structures, all the devices exhibit a qualitatively similar behaviour. Above 700 nm, the spectra exhibit a very dense and irregular series of intense absorption peaks. Fig. 6.5(**c**) is a close-up of the spectrum corresponding to the TE polarization, also including the reference spectrum corresponding to the flat device, without any grating. A first observation is that the highest absorption is achieved for the devices including a back grating, which spectrum also exhibits a higher spectral density of resonant modes. This is particularly illustrated above 900 nm, where only one broad peak appears in the case of the reference and front grating devices, whereas the structures including a back grating exhibit 4 resonances, with a reduced linewidth and a higher absorption maximum. Indeed, in this long wavelength

range, and considering the low absorption coefficient of c-Si, a longer photon lifetime is necessary to take full profit of the optical resonances of the structure, and to get closer to the critical coupling conditions [15]. Such properties are only offered provided an efficient light trapping scheme, which is achieved here thanks to the back grating diffraction process.

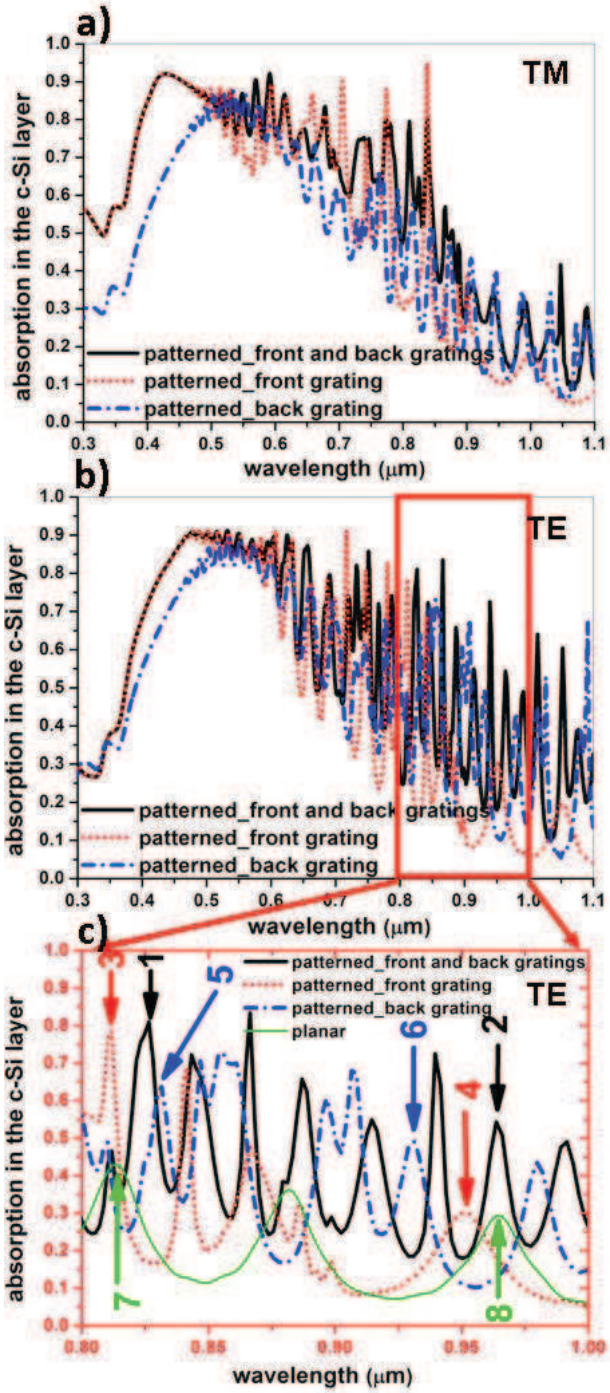

*Fig. 6.5. Absorption spectra of the c-Si layer for the front grating, the back grating and the double grating optimized structures, for (**a**) TM and (**b**) TE polarized incident light, (**c**) with a close-up of the spectra for TE polarized light between 800 and 1000 nm.*

In order to further analyze the origin of the absorption peaks which appear in the long wavelength range, the electromagnetic field maps of the corresponding modes have been simulated by FDTD for TE polarized light, and for all the four investigated structure configurations, see Fig 6.6.

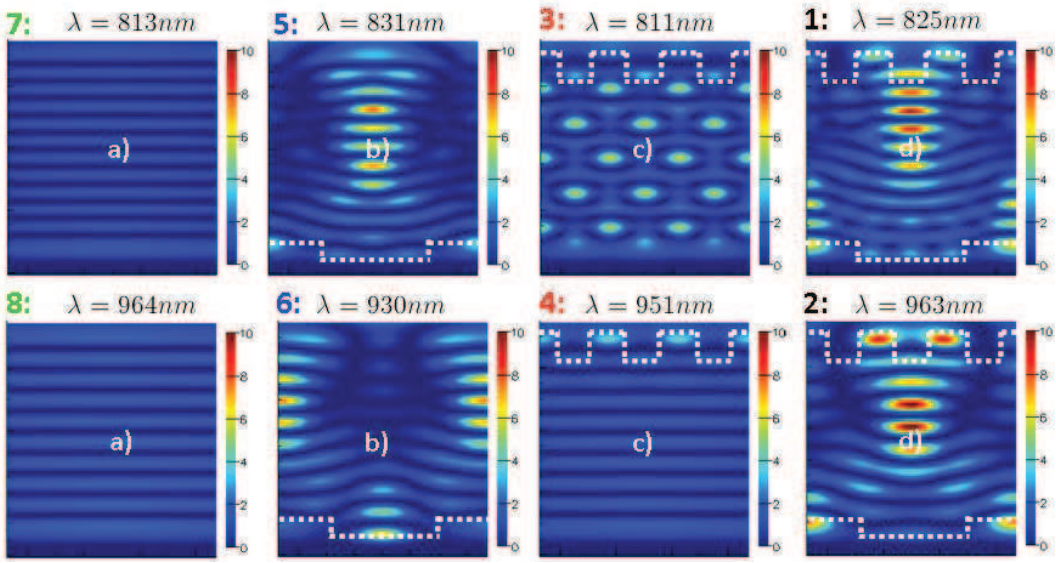

*Fig. 6.6. $|E|^2$ field maps, for TE polarized incident light in the double grating structures (peaks 1-2), in the front grating structures (peaks 3-4), in the back grating structures (peaks 5-6), and in the planar device (peaks 7-8) of Fig. 6.5(**c**)*

For the planar structure, the mode profiles are typical of vertical Fabry-Perot resonances. On the contrary, most of the modes corresponding to absorption peaks observed in simple and double grating structure exhibit a Bloch mode-like diffraction pattern, with a periodicity in the horizontal x-direction. The higher value of the maximum of $|E|^2$, together with the reduced linewidth of the corresponding absorption peaks, illustrate the longer lifetime of the photons trapped in the c-Si layer. Only the mode corresponding to peak 4, for the front grating device, exhibits a field pattern which is characteristic of a vertical Fabry-Perot-like resonance, together with a larger and less intense absorption peak. Finally, the higher absorption efficiencies of the grating structures are attributed to the large number of in-plane Bloch mode-like resonances, which quality factor is significantly higher than that of vertical Fabry-Perot modes.

6.4.2 Performance of 1D and 2D double grating solar cells

Considering the design parameters introduced above, and given the properties of the photonic gratings for light trapping and absorption control, we now discuss on the performance of such solar cells. In this section, we will first compare the four configurations introduced above, with an additional device including 2D planar gratings. Indeed, it has been shown that the expected efficiency of solar cells including 2D patterns significantly exceeds that of a 1D patterned device [15-18]. We consider the same lattice parameters, layer thicknesses and corrugation depths as in the case of 1D grating structures. Different configurations have been considered in terms of air-surface filling faction (*ffair*) for the front and back gratings, in the 32-75% range, which remains accessible with available lithography and etching processes. The schematic cross section and top views of the 1D and 2D patterned devices are shown in Fig. 6.7(**a**)-(**c**).

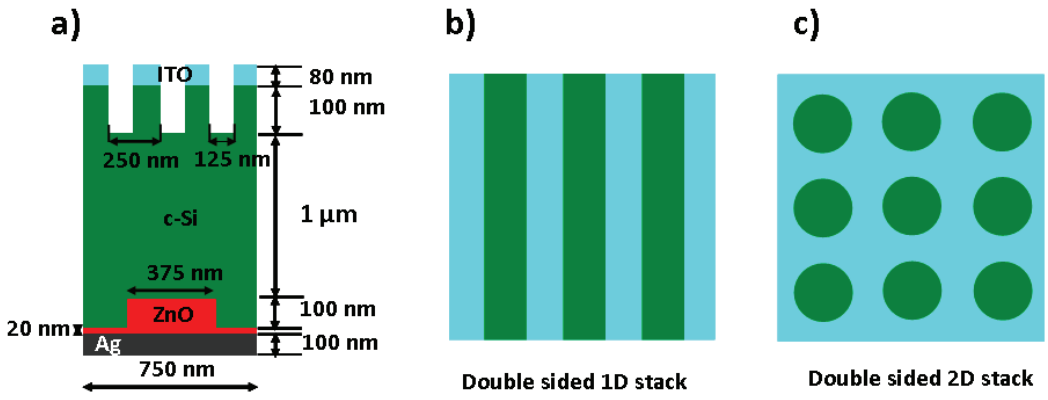

*Fig. 6.7. Schematic view of the double side structure (**a**), the top view of the patterned structure with 1D (**b**) and 2D (**c**) diffraction gratings*

Figure 6.8(**a**) displays the spectra calculated for the flat unpatterned reference, together with patterned structures including 1D and 2D front and back gratings. A first conclusion is that the devices which integrate 1D and 2D gratings exhibit a higher absorption over the whole wavelength range, from 300 to 1100 nm. In the case of the 2D structure, the increase is particularly high in the short and longer wavelength ranges with, respectively, a broad absorption plateau around 450 nm,

and many sharp and intense absorption peaks in the near-infrared. Moreover, considering the shape of the absorption spectra, one can conclude that the nature of the resonant modes is similar for the devices including 1D or 2D patterns. Figure 6.8(**b**) shows the short circuit photocurrent density for all the investigated structures. While a single 1D diffraction grating enables a 25% relative increase of the photocurrent density with regards to the flat unpatterned reference, the integration of both a front and a back grating yields a 43% increase. Now considering such a double side grating devices, but with 2D patterns, the increase is up to 65%, with a current density of 30.3 mA/cm². Therefore, compared to the case of optimized devices including 1D gratings, the results obtained with a few configurations including 2D gratings clearly illustrate their higher potential for photocurrent enhancement. Compared to results obtained by other groups a few years ago [2, 8] or very recently [9], we achieve higher current density for a similar c-Si thickness [8], or a similar value but for a thinner active layer, or more simple and technologically feasible patterns [2, 9].

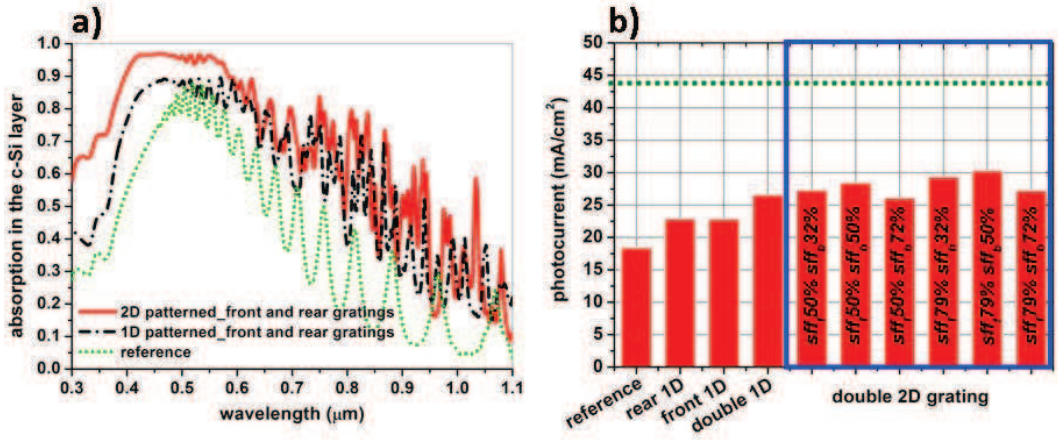

*Fig. 6.8. Absorption spectra for the flat unpatterned reference, compared to the 1D double grating structure, considering the average of spectra corresponding to TE and TM polarized incident light, and the 2D double grating structure (**a**), and short circuit current density for all the structures investigated, with a total c-Si layer thickness of 1.2 μm (**b**). As a comparison, a full absorption of the incident light would lead to a 43.5 mA/cm2 current density (dotted line).*

Lastly, the effect of the thickness of the c-Si layer is investigated in the case of the double grating structure based on 1D gratings, with the geometrical parameters mentioned in Fig. 6.9 (**a**). While the Ag, ZnO and ITO layer thicknesses and grating depths are kept constant, the total c-Si thickness (*h*) is tuned from 600 nm to 2000 nm with steps of 200 nm, and the collected photocurrent is then derived, see Fig. 6.9 (**b**).

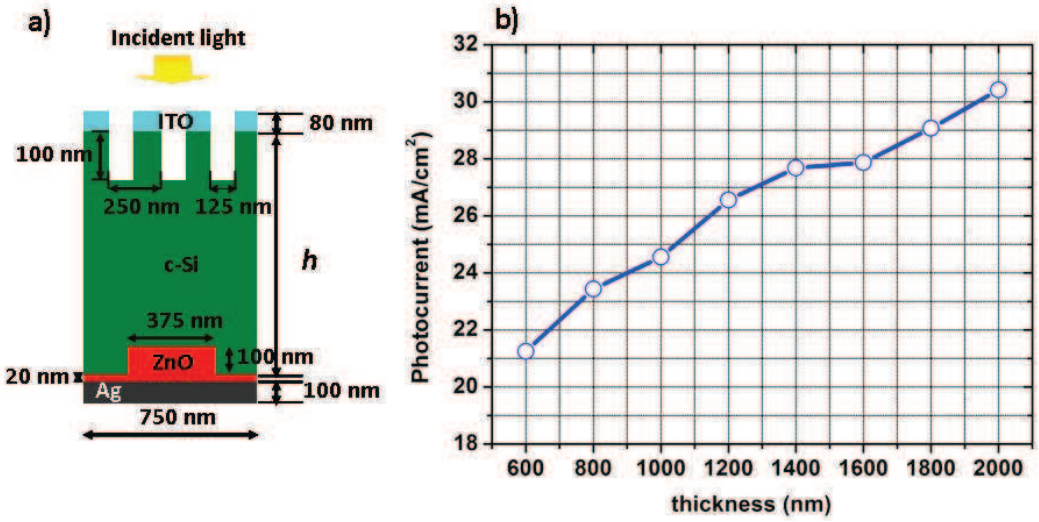

*Fig. 6.9. Schematic cross section view of the optimized front and back gratings solar cell stack (**a**), and photocurrent versus the c-Si layer thickness, for a TM polarized incident light (**b**)*

As one could expect, the short circuit current is increased with the c-Si layer thickness. This increase is not perfectly regular since it depends on the number of resonant modes which are generated in the 300-1100 nm wavelength range. Still, the photocurrent variation is monotone; this tends to prove that the front and back 1D gratings are not fully coupled. Indeed, a strong coupling between the gratings should lead to a more complex variation of the short circuit current versus the thickness. This trend was also observed by Bozzola et al, for 1D and 2D patterned c-Si cell and a-Si, with a single side grating, and therefore a lower short circuit current [19]. In the case of our double side 1D patterned device, a 30.42 mA/cm^2 photocurrent could be achieved with 2 µm thick c-Si layer.

6.5 The fabrication route for the front and back 1D and 2D grating c-Si solar cells

Given the previous simulation results, double front and back grating structures appear to be a promising approach to boost thin film solar cell efficiency.

However, compared to single grating structures, their fabrication using the techniques developed in chapter (holographic lithography, RIE...) remains challenging, mainly because the front and back have different periods and thus need to be written separately. Hopefully, it has to be noticed that additional calculations have shown that the possible misalignment between the two gratings has a negligible effect on the absorption.

Several solutions can be envisaged:

- Using deposition of the active material on a patterned back contact, provided the deposition thickness is large enough to provide an almost flat front surface, for an easier following patterning;
- Using heterogeneous bonding techniques, to integrate the active layer on a planarized back grating, then substrate removal and patterning of the front grating.

Given the accessible processes during this work, first solution has been selected and is described in the following. It is also noticeable that due to some technological constraints, the fabricated structures might differ from the optimal one simulated in the previous section.

In the following, a possible process using deposition is described, then illustrated, but using SiO_2 instead of Si, allowing the validation of a 2 holographic lithography steps process.

6.5.1 General designed processes for the front and back 1D or 2D grating c-Si solar cell stack

In this subsection, we discuss on the steps leading to the patterning of double 1D and 2D grating solar cell stacks, using holographic lithography and RIE as well as ICP techniques combined with the plasma enhanced chemical vapour deposition (PECVD), reactive frequency (RF) deposition, sputtering deposition techniques and very high-frequency glow discharged technique (VHF-GD) [20-21].

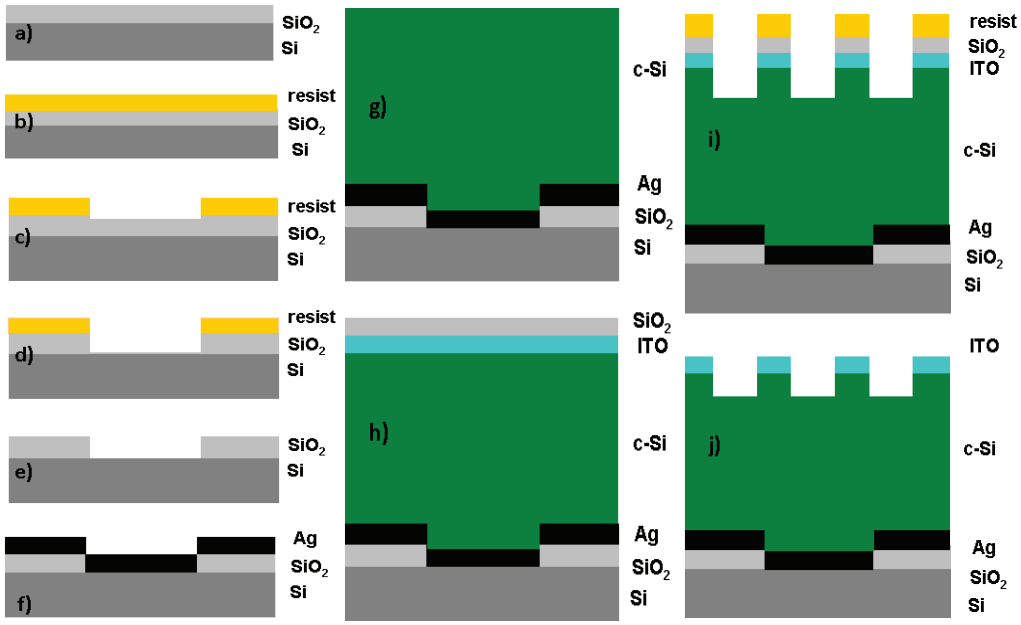

*Fig. 6.10. Main steps of the processes enabling to fabricate and pattern a front and back 1D or 2D grating solar stack by using laser holographic lithography (**c, i**), RIE (**d, e, i**) and ICP (**i**) etching steps combined with several deposition techniques (**f, g, h**)*

For simplification reason, the target of fabrication processes is the double 1D grating structure. The processes to generate the double 2D grating structure are similar to the double 1D stack, the difference is mainly on the lithography methods. The stacks, based on Si substrate, a 0.1 µm thick SiO2 is deposited by PECVD, shown in Fig. 6.10(**a**). A first laser holographic lithography step is used to pattern the back grating. The PC pattern defined by laser holographic

lithography is first transferred into a 0.1 μm thick SiO_2 hard mask (as shown in Fig. 6.10(**d**)) by gases plasma, then the photoresist is removed by RIE (See Fig. 6.10(**e**)). Then the back contactor 0.1 μm Ag is deposited by physical vacuum deposition (PVD), a thin buffer layer Chromium (Cr) is needed between glass and Ag, displayed in Fig. 6.10(**f**). Then the back grating is generated with a larger period. The doped p^+-i-n^+ poly c-Si is deposited by VHF-GD shown as Fig. 6.10(**g**). The top ITO (0.08 μm) and the 0.1 μm thick SiO_2 mask layers will be deposited by sputtering (See Fig. 6.10(**h**)). The following works are focused on how to generate the front grating. As discussed, the front grating could be achieved by laser holographic lithography, RIE and ICP. After spinning coating the resist and generating the gratings, the mask layer and ITO will be etched by RIE following the resist mask. In order to obtain vertical etched sidewalls, ICP is used to transfer the pattern in the c-Si layer thanks to its high etch rates by high ion density and high radical density, as displayed on Fig.6.10(**i**); finally, the resist and mask are removed by RIE (shown in Fig. 6.10(**j**)). From now on, the final complete double grating stack with different periods has been generated by laser holographic lithography, RIE and ICP combined with several deposition techniques.

6.5.2 The first fabrication tests

In our first double grating fabrication test, the actual thicknesses of each layer, shown on Fig. 6.10, may be slightly different from the targeted ones due to technological uncertainties. As a first step, resist has been patterned as a 1D PC via laser holographic lithography, and then patterns are transferred into the SiO_2 hard mask layer by RIE with a CHF_3 plasma using a 16sccm flow, at 15mT, and with a power of 100W for 1000s. The back period is 750 nm and groove is around 110 nm, see Fig. 6.11(**c**). Then the 0.1 μm Ag and 1 μm thick SiO_2 (replaced the real Si in this first fabrication process) are deposited by PVD and PECVD. The front grating is created by laser holographic lithography and RIE with a larger

period. Period and depth of the front grating are 250 nm and 130 nm, as depicted on Fig. 6.11(**b**) and (**a**). The profile view of the final first double 1D grating stack is shown in the Fig. 6.11(**a**).

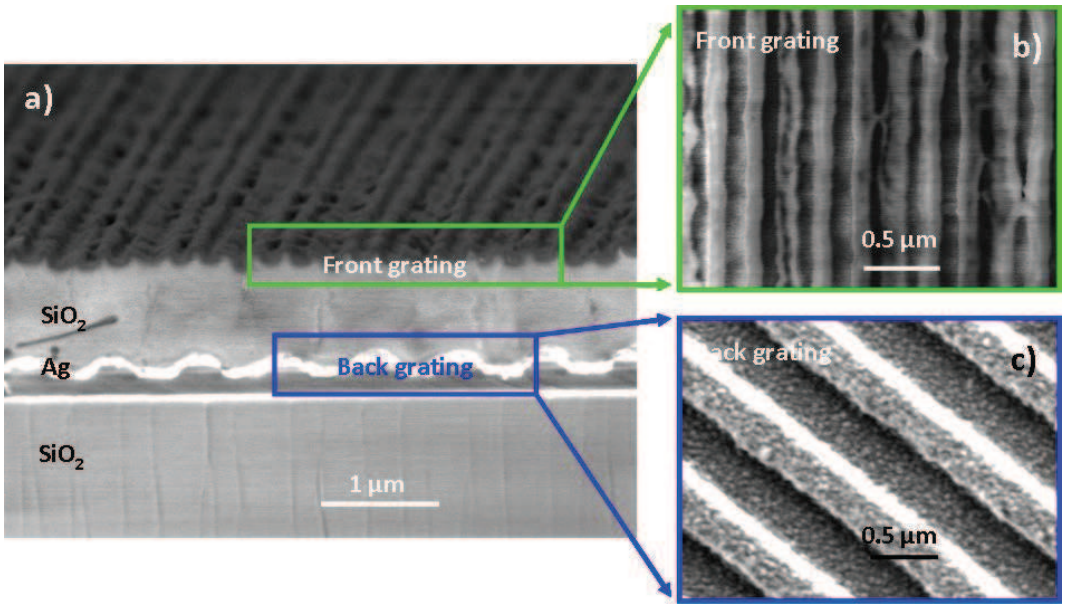

*Fig. 6.11. SEM image of the double 1D patterned module with different front and back periods (the front period around 0.75 µm, the back period 0.25 µm). (**a**) the profile view, and the top view of (**b**) the front grating, as well as (**c**) the back grating.*

This first fabrication process proved that double textured 1D grating could be patterned by the laser holographic lithography and RIE. Indeed, the shape of the front grating almost corresponds to a binary grating. However, possible cracks in the SiO_2 have to be investigated.

Conclusion and outlook

Thin-film photovoltaic solar cells structures based on c-Si, and integrating simultaneously a front and a back 1D and 2D diffraction grating with different periods have been designed and analyzed. The geometrical parameters of both gratings have been designed separately, considering the need to increase photon lifetime in c-Si, efficient anti-reflection at the front surface, and the compatibility with standard processing techniques.

- These considerations led to a back grating located at the c-Si/ZnO interface, with a period of 750 nm, and a front grating made of ITO and c-Si, with a period of 250 nm. In both cases, rectangular pattern shapes and 50% surface filling fraction were selected to ensure the technological feasibility of the photonic structures with already established technological processes.
- The spectral properties and resonant mode nature were then analyzed, and the performance of the double grating solar cell device were simulated and compared to flat or single grating references. As a result, for only a 1.2 μm thick c-Si layer, a photocurrent density of 26.5 mA/cm² is achieved for a 1D patterned double grating structure, which is obviously higher than the flat reference with 18.4 mA/cm². The photocurrent density can be further increased considering the degrees of freedom corresponding to the photonic pattern dimensionality and the active layer thickness, and without affecting the technological feasibility of the device. In particular, a value of 30.3 mA/cm² is expected in the case of similar structures with 2D patterns.
- The possible route to fabricate such front and back 1D and 2D grating stacks was investigated, using LHL, RIE and ICP etchings combined with several deposition techniques. In the next months, we plan to fabricate a real solar cell including double 1D or 2D gratings.

- In addition, more complex grating profiles could be addressed and investigated to enhance the integrated absorption and electrical properties [26-27]. Meanwhile, diffraction gratings have also been considered to create back reflectors either in TCO [14, 28-30], in metal [4], or into c-Si [7] for solar cells to reduce the transmission and enhance absorption. Based on this idea, there are hundreds of possible designs for double texturation structures to improve efficiency of solar cells in our future works

Reference and links

[1] O. El Daif, E. Drouard, G. Gomard, A. Kaminski, A. Fave, M. Lemiti, S. Ahn, S. Kim, P. Roca i Cabarrocas, H. Jeon. and C. Seassal, "Absorbing one-dimensional planar photonic crystal for amorphous silicon solar cell," Opt. Express **18**, A293-A299 (2010).

[2] J. G. Mutitu, S. Shi, C. Chen, T. Creazzo, A. Barnett, C. Honsberg, and D. W. Prather, "Thin film solar cell design based on photonic crystal and diffractive grating structures," Opt. Express **16**, 15238–15248 (2008).

[3] M.Peters, J. C.Goldschmidt, T. Kirchartz, and B.Bläsi, "The photonic light trap--Improved light trapping in solar cells by angularly selective filters," Sol. En. Mat. Sol. Cells **93**, 1721-1727 (2009).

[4] J. Chen, Q.K. Wang and H.H Li, "Microstructured design of metallic diffraction gratings for light trapping in thin-film silicon solar cells," Opt. Com. **283**, 5236-5244 (2010).

[5] J-S Cho, S. Baek and J. C. Lee, "Surface texturing of sputtered ZnO:Al/Ag back reflectors for flexible silicon thin-film solar cells," Sol. En. Mat. Sol. Cells **95**, 1852–1858 (2011).

[6] Young Min Song, Jae Su Yu, and Yong Tak Lee, "Antireflective submicrometer gratings on thin-film silicon solar cells for light-absorption enhancement," Opt. Lett. **35**, 276–278, 2010.

[7] S. H. Zaidi, J. M. Gee, and D. S. Ruby, "Diffraction grating structures in solar cells," in Twenty-Eighth IEEE Photovolt. Spec. Conf., 395-398 (2000).

[8] R. Dewan, M. Marinkovic, R. Noriega, S. Phadke, A. Salleo and D. Knipp, "Light trapping in thin-film silicon solar cells with submicron surface texture," Opt. Express **17**, 23058-23065 (2009).

[9] K. X. Wang, Z. Yu, V. Liu, Y. Cui, and S. Fan, "Absorption enhancement in ultrathin crystalline silicon solar cells with antireflection and light-trapping nanocone gratings," Nano. Lett. **12**, 1616–1619, (2012).

[10] R. Biswas and C. Xu, "Nano-crystalline silicon solar cell architecture with absorption at the classical 4n2 limit," Opt. Express **19**, 664-672 (2011).

[11] J. Gjessing, E. S. Marstein, and A. S. Sudbø, "2D back-side diffraction grating for improved light trapping in thin silicon solar cells," Opt. Express **18**, 5481-5495 (2010).

[12] Mavrokefalos, S.E. Han, S. Yerci, M.S. Branham, G. Chen, "Efficient light trapping in inverted nanopyramid thin crystalline silicon membranes for solar cell applications", Nano Lett. **6**, 2792-2796 (2012).

[13] *Handbook of optical constants of solids*, edited by Edward D. Palik (Academic Press, 1985)

[14] H. Sai, H. Fujiwara, and M. Kondo, "Back surface reflectors with periodic textures fabricated by self-ordering process for light ctrapping in thin-film microcrystalline silicon solar cells," Sol. En. Mat. Sol. Cells **93**, 1087 (2009).

[15] X Meng, G. Gomard, O. El Daif, E. Drouard, R. Orobtchouk, A. Kaminski, A. Fave, M. Lemiti, A. Abramov, P. R. i Cabarrocas and C. Seassal, "Absorbing photonic crystals for silicon thin-film solar cells: Design, fabrication and experimental investigation," Sol. En. Mat. Sol. Cells **95**, 32–38 (2011).

[16] X. Meng, V Depauw, G. Gomard, O. El Daif, C. Trompoukis, E. Drouard, A. Fave, F. Dross, I. Gordon, and C. Seassal, "Design and fabrication of photonic crystals in epitaxy-free silicon for ultrathin solar cells," Proceedings of SPIE (2011), **8312**, 831207.

[17] X. Meng, V. Depauw, G. Gomard, O.EI Daif, C. Trompoukis, E. Drouard, C. Jamois, R. Orobtchouk, A. Fave, F. Dross, I. Gordon, and C. Seassal, "Design, Fabrication and optical characterization of photonic crystal assisted thin film monocrystalline-silicon solar cells," Opt. Express **20**, A465-A475 (2012).

[18] A. Bozzola, M. Liscidini, and L. Claudio Andreani, "Photonic light-trapping versus lambertian limits in thin film silicon solar cells with 1d and 2d periodic patterns," Opt. Express **20**, A224–A244 (2012).

[19] S. H. Zaidi, J. M. Gee, and D. S. Ruby, "Diffraction grating structures in solar cells," in *Twenty-Eighth IEEE Photovolt. Spec. Conf.*, 395-398 (2000).

[20] U. Kroll, J. Meier, P. Torres, J. Pohl, and A. Shah, "From amorphous to microcrystalline silicon films prepared by hydrogen dilution using the vhf (70 mhz) gd technique," J. Non-Cryst. Solids **227**, 68–72 (1998).

[21] J. Meier, E. Vallat-Sauvain, S. Dubail, U. Kroll, J. Dubail, S. Golay, L. Feitknecht, P. Torres, S. Fay, D. Fischer, et al, "Microcrystalline/micromorph silicon thin-film solar cells prepared by vhf-gd technique," Sol. En. Mat. Sol. Cells **66**, 73–84, 2001.

[22] A. W. Blakers and M. A. Green, "20% efficiency silicon solar cells," Appl. Phys. Lett. **48**, 215 (1986).

[23] R. R. King, R. A. Sinton, and R. M. Swanson, "Front and back surface fields for point-contact solar cells," In Proceedings of the 20th IEEE Photovoltaic Specialists Conference, Las Vegas, 538 (1988).

[24] A.G. Aberle. Surface passivation of crystalline silicon solar cells: a review. Progress in Photovoltaics: Research and Applications **8**, 473–487 (2000).

[25] A.G. Aberle, "Overview on sin surface passivation of crystalline silicon solar cells," Sol. En. Mat. Sol. Cells **65**, 239–248 (2001).

[26] J. Gjessing, A. S. Sudbo, and E. S. Marstein, "Comparison of periodic light-trapping structures in thin crystalline silicon solar cells," J. Appl. Phys. **110**, 033104 (2011).

[27] Shrestha Basu Mallick, Mukul Agrawal, Artit Wangperawong, Edward S. Barnard, Kaushal K. Singh, Robert J. Visser, Mark L. Brongersma, and Peter Peumans, "Ultrathin crystalline-silicon solar cells with embedded photonic crystals," Appl. Phys. Lett. **100**, 053113 (2012).

[28] M. Vanecek, O. Babchenko, A. Purkrt, J. Holovsky, N. Neykova, A. Poruba, Z. Remes, J. Meier and U Kroll, "Nanostructured three-dimensional thin

film silicon solar cells with very high efficiency potential," Appl. Phys. Lett. **98**, 163503 (2011).

[29] C. G. Granqvist and A. Hultåker, "Transparent and conducting ITO films: new developments and applications," Thin Solid Films **411**, 1 (2002).

[30] J. Y. Chen and K. W. Sun, "Enhancement of the light conversion efficiency of silicon solar cells by using nanoimprint anti-reflection layer," Sol. En. Mat. Sol. Cells **94**, 629–633 (2010).

Chapter 7

Conclusions and outlook

Conclusions

The main goal of this thesis is to develop photonic crystal (PC) or diffraction grating assisted thin film silicon solar cell stacks to enhance the optical absorption and then the short circuit current density, as well as to maintain the efficiency of high level.

We have first designed, fabricated and optically characterized a 2D PC hydrogenated amorphous silicon (a-Si:H) thin film solar cell stack. The fabrication processes based on laser holographic lithography (LHL) and reactive ion etching (RIE) are focus on and mainly developed to generate such 2D PC patterned stacks. In this investigation, we found that exposure, post-exposure backing (PEB) and development time of lithographic process were the main impact factors to generate desired configurations. Meanwhile, an additional descum etch step was necessary and optimized to achieve a better control of the geometrical parameters with lower roughness of sidewalls. Measured and calculated absorption spectra exhibit a very similar behaviour. The absorption, integrated over the 300-720 nm range, is increased by 28 % in the case of a solar cell stack patterned as a PC membrane. This increase is mainly attributed to the positive role of Bloch mode resonance of the PC membrane above 550 nm. Additionally, these "photonized" cells were independent to the polarization of the light and presented a good tolerance towards the angle of incidence.

The thin-film crystalline silicon (c-Si) photovoltaic solar cells stacks integrating PCs have been then designed, fabricated and characterized. The numerically optimized 1D and 2D PC assisted 1 μm thick structures show 38 % and 50 % increased absorption in the active layer, as compared to the unpatterned stack, from 300 nm to 1100 nm wavelength range. A fabrication process based on LHL, RIE and inductively coupled plasma (ICP) etching has been developed to enable the generation of these 1D and 2D PC on a wide surface. Both the patterned and unpatterned reference cell stacks were measured and compared to the calculated spectra. Despite some discrepancies due to inaccuracies in

geometrical parameters, measured and calculated absorption spectra exhibit a very similar behaviour. Meanwhile, the fabricated stack exhibits a moderate dependence on the light angle of incidence.

At the same time, thin film photovoltaic c-Si solar cells structures integrating simultaneously a front and a back 1D and 2D diffraction grating with different periods have been designed and analyzed. The geometrical parameters of both gratings have been designed and optimized separately, considering the need to increase photon lifetime in c-Si, efficient anti-reflection at the front surface, and the compatibility with standard processing techniques. These considerations led to a 750 nm back grating period and a 250 nm front grating period. By considering the technological feasibility of the photonic structures with LHL, RIE and ICP, rectangular pattern shapes and 50% surface filling factor were selected to generate these optimized parameters. The spectral properties and resonant mode nature were then analyzed, and the performance of the double grating solar cell device were simulated and compared to flat or single grating references. As a result, for a 1.2 μm thick c-Si layer, a photocurrent density of 26.5 mA/cm² is achieved for a 1D patterned double grating structure, i.e. a 43% increase with regards to the flat reference. The photocurrent density can be further increased considering the degrees of freedom corresponding to the photonic pattern dimensionality and the active layer thickness, and without affecting the technological feasibility of the device. In particular, a value of 30.3 mA/cm² is expected in the case of similar structures with 2D patterns. The possible route to fabricate such front and back 1D and 2D grating stacks is designed through LHL, RIE and ICP etchings combined with several deposition techniques.

Outlook

The first 2D patterned c-Si thin film solar cell stack shows 20% higher short circuit current density (15.43 mA/cm^2) than for a similar but planar reference solar cell. This encouraging result can be improved in the short term by following more precisely the targeted optical designs and by using better passivation of etched surfaces.

In a longer term, more advanced optical designs, such as those including double diffraction gratings, as well as others using more complex patterns (mutiperiodic, partly random) can be considered. Several improvements can also be introduced in our processes. Among them, we can mention a better link between optical and electrical simulations to optimize the electrical properties, and the use of advanced holographic or nanoimprint lithography for more complex patterns. The main objective of the ongoing work is to reach a current density of 30 mA/cm², with an efficiency of 15%, in ultra thin film c-Si solar cells of about 2µm thick.

Annex. A

The optical indices of the materials (c-Si [from ellipsometric measurement], ITO [from ellipsometric measurement], Al①, a-Si:H [from ellipsometric measurement], ZnO①, Ag①) are figured out in Fig. A. They are used in our optical simulations to obtain more accurate absorption intensity in designed solar cell stacks. The thickness and position of each layer will be discussed in following chapters.

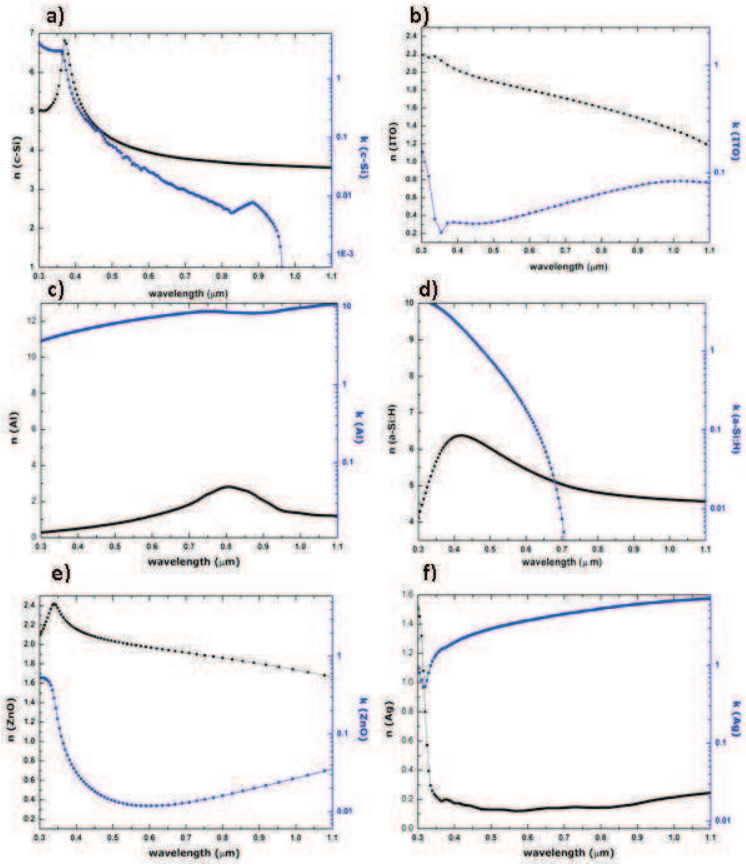

Fig. A. Refractive index n and extinction coefficient k of ITO [from ellipsometric measurement), a-Si:H [from ellipsometric measurement] (above 0.7 μm, k=0), c-Si [from

ellipsometric measurement] (above 1 μm, k=0), ZnO [from ellipsometric measurement], Ag, and Al ① *(between 300 nm and 1100 nm) used for optical simulations*

Annex. B

This script is used to calculate power absorption as:

$$Pabs = 0.5real(i\varpi \vec{E}\square\vec{D}) = -0.5\varpi \mid E \mid^2 imag(\varepsilon)$$

At a given frequency, the whole absorption in the active layer is thus obtained through the integration of the previous equation.

In order to calculate the absorption, we need to know the electric field intensity and the imaginary part of the permittivity, which could be measured by using a special script:

```
##############################################################
# get raw data from monitors
# x, y, z, f: spatial and frequency position vectors
# n: refractive index
#E2=getelectric("field");#|E|^2
W=meshgrid3dz(x,y,2*pi*f); # create 3D matrix of f and sourcepower that
SP=meshgrid3dz(x,y,sourcepower(f)); # that is the same size as E2 and n
# calculate power absorption as a function of x,y,f
epsilon = eps0*n^2; #
Pabs = 0.5*W*E2*imag(epsilon)/SP;# pinch out each frequency and integrate over filtered Pabs
# create filter for cSi and integrate over the area
nx=getdata("index","index_x"); # get the index data
filter=real(nx)>3.5; # set matrix to 1 if index over 3.5, 0 otherwise
Pabs_total=matrix(1,length(f)); # initialize matrix to hold Pabs data
for (i=1:length(f)) {
Pabs_total(i)=integrate(pinch(Pabs,3,i)*pinch(filter,3,i),1:2,x,y); # pinch out each frequency and
integrate over filtered Pabs == -0.5 * w *|E|^2 * imag(eps)
}
#plot(c/f,Pabs_total);
write("Abs_cSi.txt",num2str(Pabs_total));
##############################################
```

To identify *nx > 3.5* (*n = n_cSi* > 3.5), which means the index of this region is larger than 3.5, this part will be considered into the absorption calculation.

① *Handbook of optical constants of solids*, edited by Edward D. Palik (Academic Press, 1985)

Annex. C

The order directions of a 1D grating can be calculated by:

$$\sin\theta_m + \sin\theta_i = +m\lambda / \Lambda n \quad \rightarrow \vec{k}_m = \vec{k}_i + m\frac{2\pi}{\Lambda}$$

where k is wave vector, n is the refractive index, λ is the wavelength in vacuum, Λ is the grating period, m is the diffraction order (0, ±1, ±2…), θ_i is the incident angle, θ_m is the diffraction angle for the m^{th} order. Therefore, the grating order direction can be calculated without running a simulation. The fraction of power transmitted to each grating order can be calculated at all frequency points recorded by the monitor. Meanwhile, the number and angle and the intensity of propagating grating orders are calculated by scripts:

```
## ####################################

f=getdata(mname,"f");# get frequency vector
size_f=length(f);
T=transmission(mname); # get total net power transmitted through monitor
n=gratingn(mname,size_f);  # find the maximum possible number of grating orders
size_n=length(n);
T_grating = matrix(size_n,size_f); # grating order strength vs f # initialize matrices
theta = matrix(size_n,size_f); # angle matrix
for (i=1:size_f) {          # loop over each frequency point
n_tmp = gratingn(mname,i); # get the grating numbers at this frequency
n1 = find(n,n_tmp(1)); # calculate indices for inserting these results into final matrix
n2 = find(n,n_tmp(length(n_tmp)));
theta(1:n1,i) = -90; # calculate grating order angles # set unused orders to -90 or +90
theta(n2:size_n,i) = 90;
theta(n1:n2,i) = gratingangle(mname,i);
T_grating(n1:n2,i)=grating(mname,i)*T(i); # calculate grating orders and save into T_grating
matrix
}
# Calculate the number of grating orders (theta < 90)
num_orders = sum( (abs(theta) < 89.9) ,1);
if (make_plots) {
```

```
plot(c/f*1e9, num_orders, # plot number of orders
"wavelength (nm)","","Number of grating orders");
# plot data for a particular grating order
T_grating_plot = pinch( T_grating,1,find(n,n_target) );
theta_plot = pinch( theta ,1,find(n,n_target) );
plot(c/f*1e9, T, T_grating_plot,
"wavelength (nm)","Transmission","Transmission");
legend("Total","To order ("+num2str(n_target)+")");
plot(c/f*1e9, theta_plot,
"wavelength (nm)","angle (deg)","Propagation angle for order ("+num2str(n_target)+")");
# plot results at one frequency point
fi = find(c/f,lambda_target);
theta_plot = pinch(theta,2,fi);
T_grating_plot = pinch(T_grating,2,fi);
plot(theta_plot,T_grating_plot,
"theta (deg)","Transmission","Transmission at "+num2str(round(c/f(fi)*1e9))+"nm","plot
points");
}
##############################################
```

PUBLICATIONS

1 **X. Meng**, E. Drouard, G. Gomard, R. Peretti, A. Fave, and C. Seassal, "Combined front and back diffraction gratings for broad band light trapping in thin film solar cell," *Optics Express* **20**, A560-571 (**2012)**.

2 **X. Meng**, V. Depauw, G. Gomard, O.EI Daif, C. Trompoukis, E. Drouard, C. Jamois, R. Orobtchouk, A. Fave, F. Dross, I. Gordon, and C. Seassal, "Design, Fabrication and optical characterization of photonic crystal assisted thin film monocrystalline-silicon solar cells," *Optics Express* **20**, A465-A475 **(2012)**.

3 **X. Meng**, V. Depauw, G. Gomard, O.EI Daif, C. Trompoukis, E. Drouard, C. Jamois, R. Orobtchouk, A. Fave, F. Dross, I. Gordon, and C. Seassal, "Absorbing photonic crystals for mono-crystalline silicon thin film solar cells," *Proceedings of SPIE*, **8425**, 84250R (**2012**).

4 G. Gomard, **X. Meng,** E. Drouard, K. El Hajjam, E. Gerelli, R. Peretti, A. Fave, R. Orobtchouk, M. Lemiti, and C. Seassal, "Light harvesting by planar photonic crystals in solar cells: the case of amorphous silicon," *Recent Research Developments in Applied Physics* **14**, 024011 (**2012**).

5 **X. Meng**, V Depauw, G. Gomard, O. El Daif, C. Trompoukis, E. Drouard, A. Fave, F. Dross, I. Gordon, and C. Seassal, "Design and fabrication of photonic crystals in epitaxy-free silicon for ultrathin solar cells," *Proceedings of SPIE*, **8312**, 831207 (**2011**).

6 **X. Meng**, G. Gomard, O. El Daif, E. Drouard, R. Orobtchouk, A. Kaminski, A. Fave, M. Lemiti, A. Abramov, P. R. i Cabarrocas, and C. Seassal, "Absorbing photonic crystals for silicon thin-film solar cells: Design,

fabrication and experimental investigation," *Solar Energy Materials and Solar Cells* **95** , 32–38 (**2011**).

7 G. Gomard, E. Drouard, X. Letartre, **X. Meng**, A. Kaminski, A. Fave, M. Lemiti, E. Garcia-Caurel, and C. Seassal, "Two-dimensional photonic crystal for absorption enhancement in hydrogenated amorphous silicon thin film solar cells," *Journal of Applied. Physics* **108**, 123102 (**2010**).

8 G. Gomard, O. E. Daif, E. Drouard, **X. Meng**, A. Kaminski, A. Fave, M. Lemiti, E. Garcia-Caurel, P. R. i Cabarrocas, C. Seassal, R. B. Wehrspohn, and A. Gombert, "Design and fabrication of photonic crystal thin film photovoltaic cells" *Photonics for Solar Energy Systems III, SPIE*, **7725**, 77250M (**2010**).

9 O. E. Daif, E. Drouard, G. Gomard, **X. Meng**, A. Kaminski, A. Fave, M. Lemiti, E. Garcia Cavrel, P. Roca i Cabarrocas, S. Ahn, H. Jeon, and C. Seassal, "Absorbing photonic crystals for thin film photovoltaics," in *Photonic Crystal Materials and Devices IX, Proceedings of SPIE*, **7713**, 771308 (**2010**).

CONFERENCE PRESENTATIONS

1 **X. Meng**, E. Drouard, and al., "Combined front and rear photonic patterning for light trapping in thin film silicon solar cell," 27th European photovoltaic solar energy conference (27th EU PVSEC), Frankfurt, Germany, September 24th-27th **2012** (poster).

2 **X. Meng**, V. Depauw, and al., "Combined Front and rear diffraction gratings for light trapping in thin film silicon solar cell," The third Photovoltaic Technical Conference (PVTC), Aix-en-Provence, France, June 6th-8th, **2012** (poster).

3 **X. Meng**, V. Depauw, and al., "Absorbing photonic crystals for monocrystalline silicon thin film solar cells," SPIE Photonics Europe,

Brussels, Belgium, April 16th-19th, **2012** (presentation).

4 **X. Meng**, V. Depauw, and al., "Design and fabricate photonic crystals in epitaxy-free silicon for thin film solar cells," Fourth International Forum on Multidisciplinary Education and Research for Energy Science (GCOE), Hawaii, America, December 16th-21th, **2011** (presentation).

5 **X. Meng**, V.Depauw, and al., "Design and fabrication of photonic crystals in epitaxy-free silicon for ultrathin solar cells," Asia Communications and Photonics Conference (ACP), Shanghai, China, November 13th-16th, **2011** (presentation).

6 **X. Meng**, E. Drouard, and al., "Photonic crystals for Silicon thin film solar cells," Groupement de Recherche Ondes (GDR Ondes), Nice, France, October 21th-24th, **2011** (poster).

7 **X. Meng**, G. Gomard, and al., "Cristaux photoniques pour les cellules solaires en couches minces," Fédérqtion de Recherche sur l'énergie solaire, Lyon, France, April 4th-5th, **2011** (presentation).

8 **X. Meng**, G. Gomard, and al., "Design and fabrication of photonic crystal thin film photovoltaic cells," Thin Film 2010 international PV specialty conferences, Aix-en-Provence, France, May 27th-28th, **2010** (Poster).

dernière page de la thèse

AUTORISATION DE SOUTENANCE

Vu les dispositions de l'arrêté du 7 août 2006,

Vu la demande du Directeur de Thèse

Monsieur C. SEASSAL

et les rapports de

Monsieur L. ESCOUBAS
Professeur - Université Aix-Marseille - IN2MP - UMR 7334 - Domaine Universitaire de Saint-Jérôme
13397 MARSEILLE cedex 20

Et de

Monsieur Y. JOURLIN
Maître de Conférences HDR - Université Jean Monnet Saint-Etienne - Laboratoire Hubert Curien
UMR CNRS 5516 - Bâtiment F - 18 rue du Professeur Benoît Lauras - 42000 SAINT-ETIENNE

Mademoiselle MENG Xianqin

est autorisée à soutenir une thèse pour l'obtention du grade de **DOCTEUR**

Ecole doctorale MATERIAUX

Fait à Ecully, le 1er octobre 2012

P/Le directeur de l'E.C.L.
La directrice des Etudes

M-A. GALLAND

Design and fabrication of photonic crystals and diffraction gratings for ultra thin film Si solar cells

In this thesis, light trapping schemes based on Photonic Crystals (PCs) and Diffraction Gratings are considered. The goal is to integrate such structures into ultra-thin film silicon photovoltaic solar cells, with a view to improve their conversion efficiency.

First, a PCs assisted ultra-thin film crystalline silicon (c-Si) solar cell is designed optimized by using the Finite Different Time Domain (FDTD) approach. An increase over 50% is achieved for the absorption, as integrated over the whole spectral range, by patterning a 2D PCs in the active Si layer. This enhancement is achieved by combining Slow Bloch modes and Fabry-Perot modes. In order to fabricate such solar cells, we developed a process based on Laser Holographic Lithography, Reactive Ion Etching and Inductivity Coupled Plasma etching. We have investigated the influence of the parameters taking part in these processes on the obtained patterns. Finally the optical and electrical properties of the devices have been characterized by our co-workers at IMEC, Belgium. Absorption measurements are in good agreement with the theoretical simulations. Moreover, the integrated absorption is tolerant with regard to the sunlight angle of incidence. The final fabricated 2D PCs patterned solar cell exhibits a 20% higher short circuit current (J_{sc} = 15mA/cm^2) than the reference.

Additionally, a more complex thin film c-Si solar cells integrating front and back diffraction gratings has been designed. Long wavelength absorption is increased thanks to the long period (750 nm) back grating, while the incident light reflection is reduced by using a short period (250 nm) front grating. A short-circuit current increase up to 30 mA/cm² is predicted for this device, far above the 18 mA/cm² value for the unpatterned reference

These are first steps towards the development of a future generation of PC and diffraction grating assisted solar cells.

Keywords: Photovoltaic, Light trapping, Photonic crystals, Diffraction grating

Conception et réalisation de cristaux photoniques et de réseaux de diffraction pour les cellules photovoltaïques silicium en couches ultra-minces

Ce travail de thèse est consacré au piégeage de la lumière par des cristaux photoniques (CP) et des réseaux de diffraction. L'objectif consiste à intégrer de telles structures dans des cellules solaires à couches ultra-minces de silicium, afin d'augmenter leur rendement de conversion.

Nous avons conçu et optimisé des cellules solaires en silicium cristallin (c-Si) assistées par les CP, grâce à la méthode FDTD (Finite Difference Time Domain). En gravant un CP 2D dans la couche active de silicium, l'absorption intégrée sur l'ensemble du spectre est augmentée de 50%. Cette amélioration est atteinte en combinant des modes de Bloch lent et des résonances Fabry-Perot. Afin de réaliser de telles cellules solaires, nous avons développé une filière technologique combinant insolation holographique, gravure ionique réactive et gravure ICP (Inductively Coupled Plasma). Nous avons étudié l'influence des paramètres de ces procédés sur la structuration réalisée. Enfin, les caractéristiques optiques et électriques de ces objets ont été mesurées par nos collaborateurs de l'IMEC, en Belgique. Les mesures d'absorption sont en bon accord avec les prédictions théoriques. De plus, l'absorption intégrée est peu sensible à l'angle d'incidence de la lumière solaire. La cellule solaire structurée comme un CP 2D présente finalement un courant de court-circuit d'environ 15mA/cm², soit 20% plus élevé que dans le cas de la cellule de référence.

Par ailleurs, nous avons conçu une cellule solaire en c-Si plus complexe, intégrant des réseaux de diffraction avant et arrière. L'absorption aux grandes longueurs d'onde est augmentée du fait de la période élevée (750 nm) du réseau arrière, tandis que la réflexion en face avant est diminuée du fait de la faible période (250 nm) du réseau avant. Nous avons prédit une augmentation du courant de court-circuit jusqu'à 30m A/cm² pour ce dispositif, en comparaison avec la valeur de 18 mA/cm² correspondant à la cellule de référence non structurée.

Ces résultats sont première étape vers le développement de futures générations de cellules solaires assistées par des cristaux photoniques et des réseaux de diffraction.

Mots clé : Photovoltaïque, piégeage de la lumière, cristaux photoniques, réseaux de diffraction